NORTHWESTERN UNIVERSITY

Plasmonic Sensors for Applications in Catalysis and Art Conservation

A DISSERTATION

SUBMITTED TO THE GRADUATE SCHOOL

IN PARTIAL FULLFILMENT OF THE REQUIREMENTS

for the degree of

DOCTOR OF PHILOSOPHY

Field of Chemistry

By

Alyson Victoria Whitney

EVANSTON, ILLINOIS

June 2007

Abstract

Plasmonic Sensors for Applications in Catalysis and Art Conservation

Alyson V. Whitney

The work described here includes both fundamental and application based studies centered around the use of plasmonic sensors. Fundamental studies focus on probing the optical properties of nanosphere lithography (NSL) fabricated Ag nanoparticles, while surface-enhanced Raman spectroscopy (SERS) sensors are applied to identify and characterize artists' red dye and red lake pigments. Experiments were conducted to further our understanding of the optical properties and thermal stability of NSL fabricated Ag nanoparticles in order to design the best sensor for a given system. Because these nanoparticles are extremely sensitive to their dielectric environment, atomic layer deposition (ALD) was used to fabricate highly uniform, ~1 Å, monolayers of Al_2O_3 in order produce a high resolution study of the short and long range distance dependence of the localized surface plasmon resonance (LSPR) of these nanoparticles. Because Ag triangular nanoparticles will anneal into hemispheres at elevated temperatures (200°C and above), NSL fabricated Ag nanoparticles were coated with thin layers (0.2 - 1.0 nm) of ALD Al_2O_3. These new thermally stable nanoparticles have potential to be used to conduct *in situ* monitoring of model catalytic reactions by SERS.

Plasmonic sensors were applied in the field of art conservation. Both silver island film (AgIF) and silver film over nanosphere (AgFON) SERS substrates were successfully used to identify and characterize artist's red dyes and red lake pigments. In the past, Raman spectroscopy has been successfully employed to identify many pigments and modern synthetic dyes. Unfortunately, red lake pigments are both poor Raman scatterers and extremely fluorescent, therefore there has been few Raman spectra collected for many of these materials.

SERS has been a successful technique because it not only enhances the Raman effect; but, also quenches fluorescence, resulting in detailed vibrational information that can be used to correctly identify red lakes and natural red dyestuffs. Fundamental and application based studies of plasmonic sensors are equally important so that the best sensor can be designed for the desired application.

_____

Professor Richard P. Van Duyne
Research Advisor

Acknowledgments

The thing that I value the most about Northwestern is that I have not only had the opportunity to be involved in unique and motivating scientific collaborations but have also been able to build great friendships along the way. A theme that is present throughout the Department of Chemistry is collaboration. This idea begins with the professors and as a result, projects are designed that are often not possible to replicate in the majority of other research institutions. There are many individuals who I have to thank for making the last five years not only educational but enjoyable.

First, I have to thank my advisor, Professor Richard P. Van Duyne. Rick's first priority has always been his students. His enthusiasm for science is contagious, making for a positive working environment. I came to Rick in my second year with the desire to begin a scientific collaboration with the Art Institute of Chicago. While there was no money for this project, the fact that I was interested was a good enough reason for him to allow me to become involved in this work. I am grateful to have had the opportunity to work with and learn from Rick during my time at Northwestern.

I have been involved in several scientific collaborations that would not have been possible without the help of several people. First, I would like to thank Dr. Francesca Casadio, a conservation scientist, at the Art Institute of Chicago. She has been both a mentor and friend to me. I would also like to thank Professor Peter C. Stair for involving me in a collaboration with Argonne National Laboratory. The work that I accomplished there has propelled a new area of research for the Van Duyne group. Furthermore, Peter has always been willing to take the time to discuss science, research, and my experimental results with me. I have been fortunate enough to work alongside Dr. Jeffrey W. Elam at Argonne. Jeff is a fantastic teacher and has been

incredible to work with. I would like to thank both Professor George C. Schatz and Dr. Shengli Zou for their theoretical modeling, which has provided valuable insight into my experimental work

I would like to thank my committee members, Professor Chad A. Mirkin and Professor Peter C. Stair for offering valuable comments and insight into my work. I would also like to thank Professor George C. Schatz for acting as a substitute committee member on two occasions.

Finally, I would like to thank the entire Van Dunye Group: Dave Andrews, Jeff Anker, Kevin Biggs, Julia Bingham, Jon Camden, George Chan, Jon Dieringer, Paige Hall, Kathryn Kosuda, Olga Landres, Adam McFarland, Erin McLellan, Nilam Shah, Leif Sherry, Paul Stiles, Jiha Sung, Kallie Willets, Xiaoyu, Chanda Ranjit Yonzon, Matt Young, Jing Zhao for making the Van Duyne group a great place to work.

The friendships I have built at Northwestern have provided me with an endless amount of fun, laughter and unforgettable stories. First, I would like to thank Dr. Kallie Willets who has not only been an amazing teacher but also served as the catalyst that brought our group together. Nilam Shah is someone who always understands how I think. I have had fun learning from her and am now completely and totally addicted to chaat. I would like to thank Dave Andrews for making me laugh, lending me books, daveandlena.com, making wine tasting extra fun, inspiring the famous Beer Bracket, bringing in left over brownies (when he hasn't eaten them all), and for the ability to always remain relaxed no matter what (even when lost in Chicago). I have enjoyed my time in the Front Row (Jon Deiringer, Kathryn Kosuda, and Leif Sherry). No matter what anyone says, we are and will always be the best row. I have enjoyed scientific discussions with Jon as well as serious talks about important topics such as Gilmore Girls and America's Next Top Model. I could not have picked a better person than Kathryn to take over my work. She is

smart, hard working, and fun to work with. I have sat next to Leif for the past three years and I would have it no other way…hopefully he feels the same. He helped me out with Quantum my first year and since then has become a good friend despite the fact that he eats cold clam chowder out of a can with a Star Wars spoon. While, I have known Julia Bingham only a short time, she has already she has become a great friend. Her love of Bon Jovi is inspirational. Kevin Biggs always makes me laugh and has fabulous hair. I would like to thank The Theory Floor (Eric, Sina and Raj) for providing me with much needed procrastination time. Finally, I have to thank my wonderful roommate Liza Babayan. We have lived together for four years and I will truly miss her when she leaves me in December. We have had great late night talks, insightful clothing and shoe discussions, and she is one of the best cooks I know. I can honestly say I have never had a better roommate.

I cannot forget to thank some very important people outside the Department of Chemistry who have made my time here that much more enjoyable. Brian Shah is a good friend to everyone, but more importantly, he has introduced me to the world of the Chicago Bears. No evening is really complete with out either Sara Sherry or Lena Sadowitz. I am grateful to Leif and Dave for their amazing taste in women. Without Sara how would I know that everyone needs a gravy boat. And before Lena I never knew the joy a pink cupcake could bring…although I did suspect they were pretty enjoyable.

Finally I would like to thank my family. My mom and dad have given me support not just through graduate school but throughout my entire life. Their only requirement in terms of education has been to pursue whatever would make me happy. I would also like to thank my aunt, uncle, cousins: Jane, Fraser, and Hayley, and of course Tucker for their good company and for filling my belly with tasty food during the first few years of graduate school.

Table of Contents

List of Illustrations

List of Tables

Chapter 1

Introduction to Plasmonic Sensors

1.1 Localized Surface Plasmon Resonance Sensors

The localized surface plasmon resonance (LSPR) wavelength shift response, $\Delta\lambda_{max}$, of noble metal nanoparticles fabricated by nanosphere lithography (NSL) has been used for a new class of nanoscale optical biosensors.[1-5] The LSPR phenomenon occurs when light interacts with particles that are much smaller (~10 – 200 nm) than the incident wavelength.[1,6] The resulting effect is that the electric field **E** near the particle surface is enhanced where $| \mathbf{E} |^2$ can be 100-10,000 times larger than the incident field.[1] The LSPR is extremely sensitive to changes in the local dielectric environment as well nanoparticle shape and size.[1,6-9] The Van Duyne group has extensively studied the optical properties of the NSL fabricated LSPR sensor in order to design an optimized sensor for any given system.[5,7,9-13]

Previous work has shown that when resonant molecules are adsorbed on a NSL fabricated nanoparticle, the resulting LSPR response is dependent upon the spectral overlap between the electronic resonance of the adsorbate and the plasmon resonance of the nanoparticle.[10] Further studies involving the study of the LSPR response of NSL fabricated nanoparticles to resonant adsorbates has been studied by Zhao et al.[13] The authors found that the LSPR shift induced by a resonant molecule has an oscillatory dependence on wavelength.[13] Discrete dipole approximation (DDA) calculations suggest that molecular absorption is enhanced by surface adsorption.[13] Furthermore, the authors demonstrate that the NSL fabricated LSPR sensor can be effectively used to detect the binding of a small molecule to a protein.[13] Experiments found that, an amplified spectral response is achieved when the LSPR maxima of the nanoparticle is close to the molecular resonance of the protein.[13]

The distance dependence of the LSPR of NSL fabricated nanoparticles has also been examined.[9,14] Haes and co-workers explored the long range distance dependence of the LSPR

nanosensor using self-assembled monolayers (SAMs) of 11-mecaptoundecanoic acid (11-MUD) and Cu^{2+} ions adsorbed on arrays NSL fabricated nanoparticles with various sizes, shapes, and compositions.[14] The spatial resolution of this experiment was limited to the thickness of the 11-MUD/ Cu^{2+} monolayer which was at least 1.6 nm.[14] Several interesting characteristics of the long-range behavior were found including: (1) the LSPR shift vs. SAM thickness is nonlinear; (2) Ag nanoparticles are more sensitive than Au nanoparticles; (3) nanotriangles have larger sensing distances than nanohemispheroids; (4) increasing the nanoparticle in-plane width results in larger sensing distances; and (5) decreasing nanoparticle out-of-plane height results in larger sensing distances.[14] Additionally, semi-quantitative theoretical calculations revealed that the plasmon resonance shift is controlled by the average electromagnetic field over the nanoparticle surface.[14]

Even though much important information was obtained from these studies, it was hypothesized that new information could be obtained if it were possible to deposit single layers of a material with thicknesses of ~1 Å. Furthermore, while the refractive index of the bulk SAM material is known, the refractive index of the SAM is not known making an accurate theoretical model of the experiment difficult.[14] Whitney et al were able to improve the resolution of Haes's study as well as design a more accurate theoretical model by using a material with a known refractive index. Highly uniform monolayers of Al_2O_3 can be deposited by atomic layer deposition (ALD) with ~1 Å thickness resolution and a refractive index of 1.57.[15,16] By depositing ALD Al_2O_3 multilayers onto the noble metal nanosensor, the distance dependence of the LSPR nanosensor was probed with 10x spatial resolution compared with previous work.[9,14] Furthermore, because ALD Al_2O_3 has a known refractive index, an accurate theoretical model of

the experiments could be designed. This work found good agreement between the theoretical analysis and experimental results.[9]

Finally, Sherry and co-workers have focused their work on understanding the optical properties of single noble metal nanoparticles.[11,12] The authors have correlated atomic force microscopy (AFM) with darkfield optical microscopy in order to study both the geometric and optical properties of single Ag cubic nanoparticles and triangular nanoprisms.[11,12] Using AFM measurements, accurate theoretical models could be constructed to compare theoretically predicted optical properties with those determined experimentally.[11,12] The results of these experiments showed good correlation between the theoretical and experimental measurements.[11,12] Furthermore, the authors were able to monitor the nanoparticles' sensitivity to both bulk (Solvent) and local (surface chemical modification) refractive index changes.[11,12] The results of this work have given new insight into the relationship between nanoparticle geometric and optical properties. Furthermore, the authors demonstrate that single nanoparticles are extremely sensitive to refractive index changes and therefore have the potential to successfully serve as optical biosensors.

1.2 Surface-Enhanced Raman Spectroscopy Sensors

The LSPR of noble metal nanoparticles plays an important role in the field of surface-enhanced Raman spectroscopy (SERS). Raman spectroscopy was discovered by C. V. Raman in 1928 and he was awarded the 1930 Nobel Prize in Physics for this important work.[17] Because every molecule scatters light uniquely, Raman spectroscopy is an excellent analytical tool to "fingerprint" unknown compounds. Unfortunately, Raman scattering is a weak optical process where only 1 in 10^8 of elastically scattered photons will be Raman scattered. In 1977, Jeanmarie and Van Duyne showed that the Raman scattering signal is significantly enhanced when the

Raman-active molecule is spatially confined within the electromagnetic fields generated upon excitation of the LSPR of the nanostructured noble metal surface.[18] This phenomenon, now known as SERS results in signal enhancements of up to 8 orders of magnitude over normal Raman signals.[19,20] The Van Duyne group had designed several SERS sensors for application in healthcare,[21-25] chemical warfare,[25-28] and even art conservation.[29,30]

In 2003, Shafer-Peltier and co-works designed a Ag film over nanosphere (AgFON) SERS substrate with the potential to do real time monitoring of glucose levels in human beings. Because glucose does not readily bind to silver, a tri(ethylene glycol) partition layer was employed to bring glucose molecules near the substrate surface. Since then, Shah and co-workers have improved the glucose sensor by utilizing a mixed decanethiol/mercaptohexanol partition layer which has great temporal stability, demonstrates rapid, reversible partitioning and departitioning and is more simple to control in comparison to the first generation partition layer.[21] Additionally, the authors show that the glucose sensor is stable for 10 days in bovine plasma.[21] Finally, the first *in vivo* experiments were conducted 2006 by Stuart and co-workers.[31]

Zhang and co-workers have fabricated a SERS substrate for the detection of anthrax spores.[27] The authors used a portable Raman system for their studies demonstrating that their SERS sensor has the potential to be used for the field analysis of potentially harmful environmental samples.[27] The SERS sensor presented, demonstrated detection limits of ~2.6 x 10^3 spores, which is well below the anthrax infectious dose of 10^4 spores.[27] The SERS sensor was improved upon by coating it with ~2 Å of ALD Al_2O_3.[28] The new sensor had twice the sensitivity, 6 times shorter data acquisition time, and 7 times longer temporal stability than the original sensor.[28]

1.3 Goals and Organization

The goals of the work described in this thesis are to further the understanding of the properties of plasmonic nanosensors as well as to develop these sensors for applications in catalysis and art conservation. Specifically, the distance dependence of the LSPR of NSL fabricated nanoparticles is probed using ALD Al_2O_3. Additionally, the thermally stability ALD Al_2O_3 coated NSL nanoparticles is studied. These thermally robust particles have the potential to be used for the *in situ* monitoring of model catalytic systems. Finally, both Ag island films (AgIFs) and AgFON SERS substrates have been used to identify and characterize artists' red dyes and red lake pigments, which had been previously difficult and often impossible to study with normal Raman spectroscopy.

Chapter 2 describes a novel nanopore fabrication technique using the reactive ion etching (RIE) variant of NSL and angle-resolved NSL (AR NSL). Chapters 3 and 4 describe NSL nanoparticle sensors for future applications in Operando SERS. In Chapter 3, ALD Al_2O_3 is used to study the distance dependence of the LSPR nanosensor. An extensive study of the thermal stability of ALD Al_2O_3 coated NSL nanoparticles are presented in Chapter 4. Chapters 5 and 6 focus on the utilization of SERS to study artists' red dyes and red lake pigments. In Chapter 5, AgIFs are directly applied to the red dyes and red lake pigments to obtain spectra that were previously unobtainable with normal Raman spectroscopy. Finally, the work presented in Chapter 6 involves using AgFONs to not only acquire higher resolution and more consistent spectra than previous work but also to identify individual dyes in mixtures.

Chapter 2

Sub-100 nm Triangular Nanopores Fabricated with the Reactive Ion Variant of Nanosphere Lithography and Angle-Resolved Nanosphere Lithography

2.1 Introduction

Arrays of nanoparticles and nanopores in the sub-100 nm size regime are widely used in applications such as catalysis,[32,33] sensing,[3,14,34], optics[19], molecular separation.[35-38], molecular reaction dynamics,[39] single molecule detection,[40] and electronics.[41] Consequently, there is an increasing demand for rapid, massively parallel fabrication strategies for these nanostructures. The standard lithographic techniques used to fabricate such nanostructures with controlled size, shape, and spacing include photolithography, electron beam lithography (EBL)[42], and focused ion beam lithography (FIB)[35]. Photolithography is the most widely used because it is massively parallel; however, its resolution is often limited by diffraction to ~100 nm[43]. However, recent work has demonstrated that by modifying traditional photolithographic techniques, sub-50 nm structures can be fabricated.[44] EBL and FIB are capable of producing arbitrary shaped nanoparticles and nanopores with excellent minimum feature size that are ideal for many electronic, optical, and magnetic applications. However, the high cost and serial nature of EBL and FIB present serious challenges to their high volume manufacture. Consequently, much recent research has been focused on the development of alternative parallel lithographic methods. The remainder of this paper will concentrate on the topic of low cost, parallel fabrication of nanopores.

Several parallel lithographic methods have been successfully developed to fabricate nanopores.[34,35,45] Pantano and Walt have chemically etched nanopores onto the distal face of an optical imaging fiber.[34] Because each nanopore is connected to its own optical channel it may be individually addressed or utilized as part of the entire imaging fiber array.[34] In this technique, the nanopore size is controlled by the dimensions of the imaging fiber's distal tip resulting in a minimum nanopore diameter of 250 nm. Nanoporous alumina membranes with sub-100 nm pore

dimensions have been fabricated by electrochemical anodization.[45] This fabrication method is, however, highly substrate specific. The ideal nanopore fabrication technique would not only be low cost and parallel but would also be substrate independent. The work presented herein demonstrates that the reactive ion etching (RIE) variant of nanosphere lithography (NSL) and angle-resolved nanosphere lithography (AR NSL) is a novel nanofabrication approach that yields sub-100 nm nanopores and possesses these desirable properties.

NSL has been shown to be a low cost, parallel, substrate independent technique for producing well-ordered sub-100 nm array structures with nanometer precision.[46] It is based on the self-assembly of polystyrene or silica nanospheres into close-packed monolayers or bilayers, which are then employed as lithographic masks to fabricate nanoparticle arrays. As in all naturally occurring crystals, NSL masks include a variety of defects that arise as a result of nanosphere polydispersity, site randomness, point defects (vacancies), line defects (slip dislocations), and polycrystalline domains.[47] Typical defect-free domain sizes are in the 10 – 100 μm^2 range.[47] Single layer, NSL masks yield nanostructures with a triangular in-plane shape and p_{6mm} array symmetry. Usually the sample is mounted in a physical vapor deposition system where a material is deposited normal to the substrate surface.[46] The size and inter particle spacing of the resulting nanoparticles are controlled completely by the diameter of the chosen nanospheres. This technique is, therefore, substrate independent. The in-plane width, a, of the nanoparticles produced with a single layer nanosphere mask can be predicted with equation 1.[47]

$$a = \frac{3}{2}\left(\sqrt{3} - 1 - \frac{1}{\sqrt{3}}\right)D \qquad (1)$$

AR NSL provides additional control of the size and shape of nanoparticles. The dimensions of AR NSL fabricated nanoparticles are controlled with two additional parameters:

(1) the angle between the surface normal of the NSL substrate and the propagation vector of the material deposition beam (Θ) and (2) the azimuthal angle (Φ).[48] Both Θ and Φ can be varied to produce a variety of nanoparticle geometries and inter particle spacing. Furthermore, the size and shape of the fabricated nanoparticles can be accurately predicted using the geometric model developed in our previous work.[48,49]

In this paper, we demonstrate that the combination of NSL and AR NSL with RIE is capable of fabricating size-tunable triangular nanopores in single crystal silicon (111) (Si (111)) substrates. RIE is a natural choice to use with NSL masks because of its parallel and highly anisotropic properties. Because of its anisotropic nature, RIE can also be combined with AR NSL to further reduce the nanopore dimensions. Specifically, it will be shown that this combination approach is ideal for the creation of nanopores with the following unique properties: (1) extremely uniform nanopores (in-plane widths = 44 nm – 404 nm); (2) controlled nanopore depth (25 nm – 250 nm); (3) controlled, uniform nanopore shapes; and (4) high areal density (~ 10^{10} pores cm^{-2}). The in-plane widths of the nanopores are shown to be linearly dependent upon nanosphere diameter allowing for the production of pre-determined, size tunable nanopores. AR NSL is employed to achieve a three-fold reduction of the nanopore dimensions. For example, nanopores fabricated with 720 nm diameter NSL etch-masks were found to have an average in-plane width of 297 nm. Combining AR NSL with RIE with the same diameter NSL etch-masks produced nanopores with in-plane widths of 93 - 177 nm. By extrapolation, it is reasonable to suggest that nanopores with in-plane widths of 44 nm can be reduced to ~15 nm using RIE and AR NSL.

2.2 Experimental and Methods

2.2.1 Substrate Preparation

Phosphorous doped Si (111) substrates were purchased from Wacker Siltronic (Portland, OR) and cut into ~10 mm^2-15 mm^2 pieces. The substrates were cleaned in a piranha etch solution (30 % 3:1 H_2SO_4:H_2O_2) for 30 minutes at 80°C in order to create a hydrophilic surface on Si (111) to facilitate self-assembly of the nanosphere masks. After rinsing with water, the silicon substrates were sonicated for 60 minutes in 5:1:1 H_2O:H_2O_2:NH_4OH. Finally, the silicon substrates were rinsed and stored in water for future use.

2.2.2 Reactive Ion Etching

Surfactant-free carboxyl terminated polystyrene nanospheres of specific diameters (1100 nm-160 nm) were self-assembled on to the Si (111) substrates as described in previous work.[50] The sample was then placed in an RIE chamber (RIE 2000, South Bay Technology) and etched with a CF_4 plasma. Unless otherwise stated, etch conditions were as follows: etch time = 2 minutes, radio frequency power = 45 Watts, chamber pressure = 20 mTorr, DC-Bias = -500 – -600 Volts, and flow rate = 72 sccm. When the reactive plasma bombards the polystyrene nanospheres, the hydrocarbons are fluorinated and remain intact, However, interaction between the reactive CF_4 plasma and the Si (111) substrate produces volatile SiF_4, thus etching the exposed surface area. The resulting nanostructure is a well ordered periodic array of triangular cross-section nanopores. Using this protocol, nanopores with varying in-plane widths were fabricated using nanosphere diameters of 160 nm, 290 nm 510 nm, 720 nm, and 1100 nm.

2.2.3 Angle-Resolved Nanosphere Lithography

The fabrication of nanopores by AR NSL and RIE begins with the self-assembled NSL etch mask described above. The sample substrate and etch mask are then mounted on a

machined aluminum block in order to obtain the desired angle, (Θ). The sample is then placed in the RIE chamber and etched as described above. The geometry of the nanopores was predicted using the symbolic mathematics program Maple 8 (Version 9.0, Waterloo Maple Inc., Ontario, Canada).[48] The Maple worksheet was used to determine the projection of the nanosphere mask onto a substrate for a specified Θ and azimuthal angle (Φ). The generated graphical representations of the nanopore shapes were compared to the fabricated nanopore geometries observed with scanning electron microscopy (SEM) (Gemini 1525, Leo). While Θ can be easily controlled by etching geometry, imperfections in the nanosphere mask make it difficult to control Φ resulting in a single sample containing several nanopore geometries. Determining Φ was done by choosing a value that gave the best overall shape fit for the experimentally controlled Θ values.

2.2.4 Nanopore Characterization by AFM and SEM

Characterization of the nanopore depths and in-plane widths was carried out using tapping mode atomic force microscopy (AFM) (Nanoscope IV microscope and Nanoscope IIIa controller, Digital Instruments). Accurate AFM measurements of nanopore depth are problematic due to the large size of the AFM tip relative to the nanopore aperture. Therefore, to obtain accurate depths, lines scans were measured over small defect areas on the substrate surface. In addition, the nanopore depth was measured by further cross-sectional SEM analysis. The etched Si (111) sample was first milled with FIB (FIB-2000A, Hitachi) and then cleaved to obtain a clean edge for SEM examination.

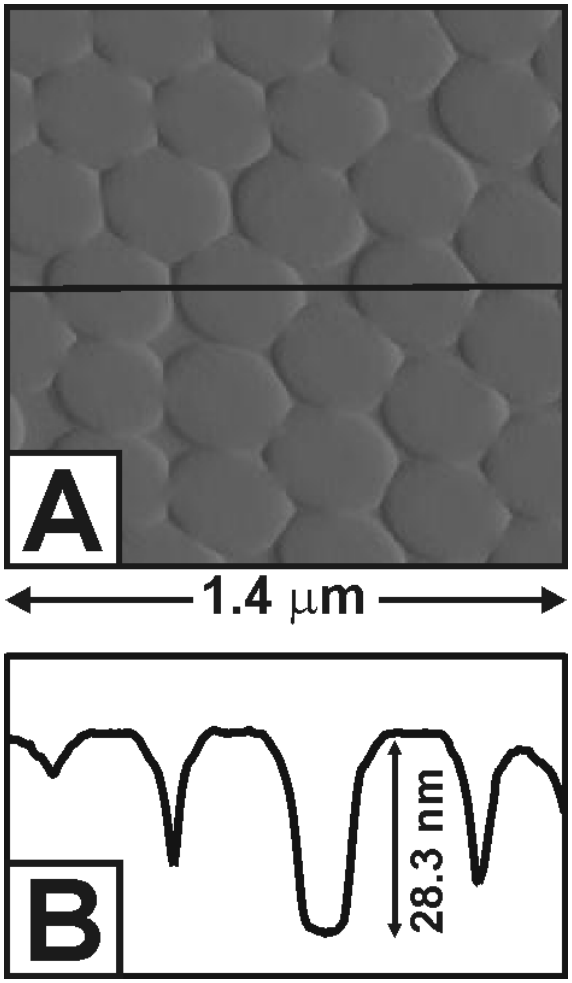

Figure 2.1 (A) AFM image of nanopores fabricated with a 290 nm nanosphere diameter etch mask on P doped Si (111) with a typical line scan (B) over a small defect area. Etch time = 2 minutes and height = 28.3 ± 0.5 nm.

2.3 Results and Discussion

This work demonstrates that nanopore size and shape tunability can be achieved by combining NSL etch masks with RIE. Figure 2.1 shows AFM images of nanopores in Si (111) fabricated using 290 nm diameter nanospheres as the etch mask along with a corresponding typical line scan. This image contains a small defect area so that the nanopore depth can be accurately determined. A two minute etch with the CF_4 plasma produced uniform depth nanopores with an average value of 28.3 ± 0.6 nm. Etching times of 2-10 minutes produced nanopore depths ranging from ~25-250 nm. We anticipate that nanopores with depths in the 1-5 μm range could be produced by using deep reactive ion etching (DRIE) conditions.[51]

2.3.1 Nanopore Characterization by SEM and AFM

A cross-sectional SEM image of an array of typical nanopores is shown in Figure 2.2 An etch mask assembled from 720 nm diameter nanospheres was used with an etch time of 4 minutes. AFM line scan analysis determined the average nanopore depth to be 106.0 nm. The cross-sectional SEM image supports this depth measurement. Interestingly, one can see that the nanopores have a tapered shape, which can be attributed to the fact that RIE is not a perfectly anisotropic process.

Nanopore in-plane widths were experimentally determined using AFM line scans and theoretically predicted using equation 1. Figure 2.3 depicts AFM images of nanopores fabricated with nanosphere etch masks with nanosphere diameters of 720 nm, 290 nm, and 160 nm and corresponding line scans. The in-plane widths of the respective nanopores were experimentally found to be 297.9 ± 13.9 nm, 102.7 ± 6.4 nm, and 44.9 ± 8.4 nm. The propagation vector of the RIE plasma was normal to the Si (111)/ nanosphere surface. While the reader may interpret Figure 2.3 to depict nanoparticles instead of nanopores, the corresponding line scans clearly

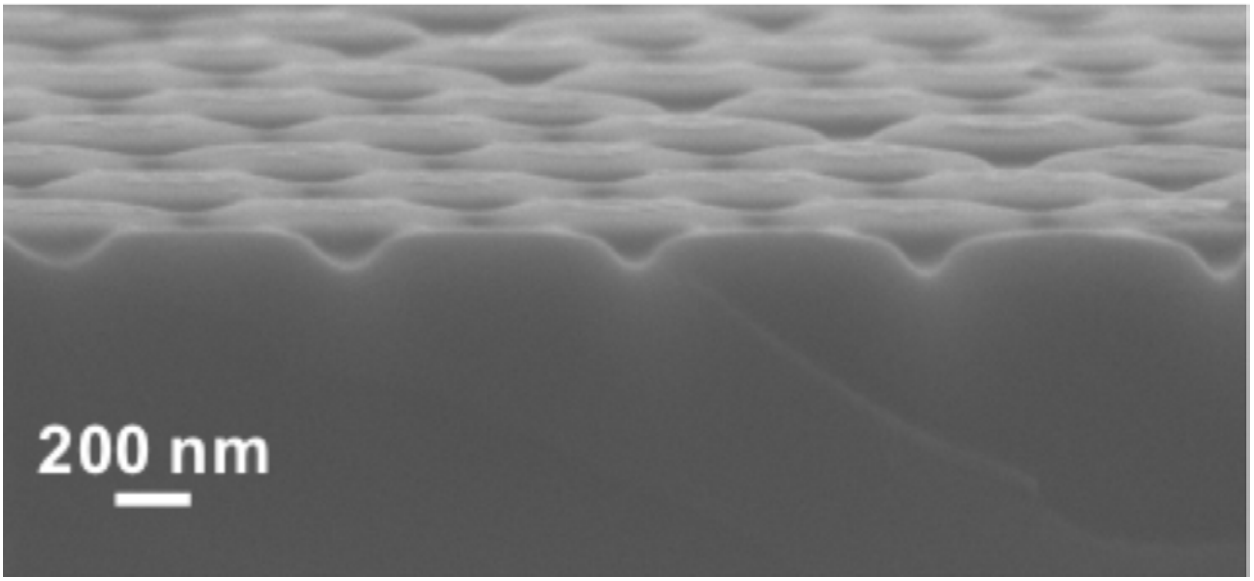

Figure 2.2. SEM image of a cross-section of nanopores fabricated with a 720 nm diameter nanosphere etch mask with an etch time of 4 minutes.

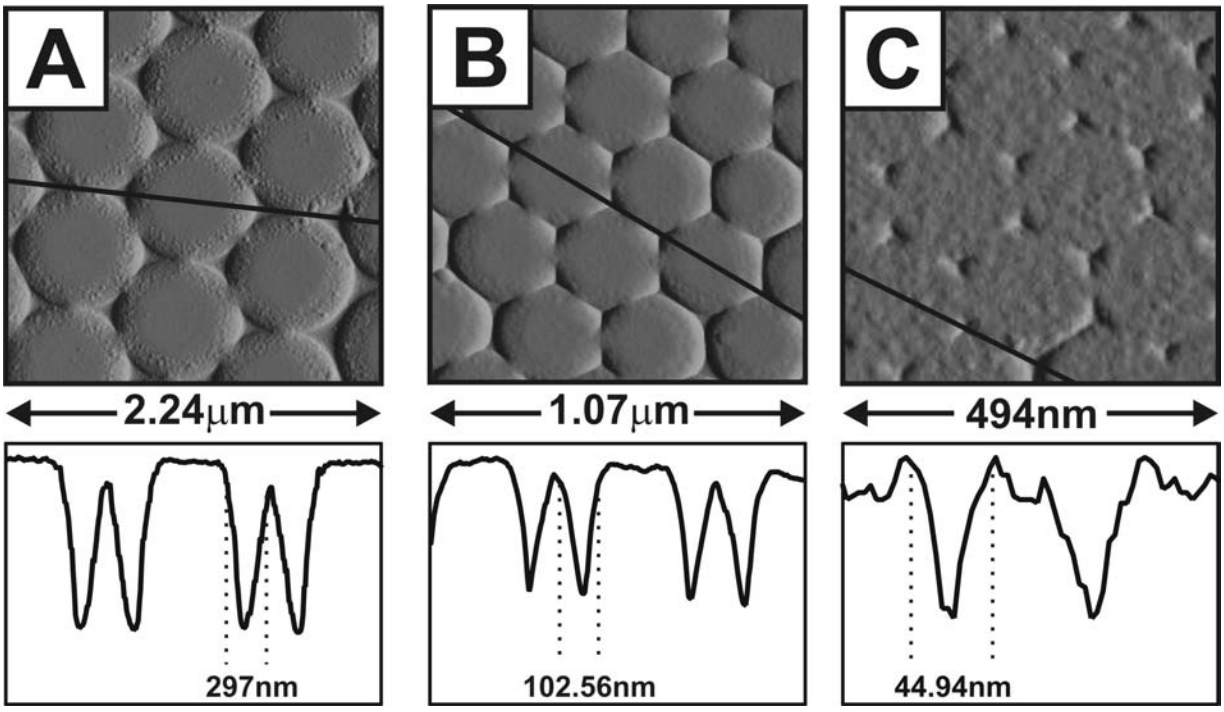

Figure 2.3 AFM images of several sizes of nanopore structures on Si (111) with corresponding line scans. (A) Nanopores fabricated with 720 nm diameter nanosphere etch mask. In-plane width = 297.9 ± 13.9 nm. (B) Nanopores fabricated with 290 nm diameter nanosphere etch mask. In-plane width = 102.5 ± 6.4 nm. (C) Nanopores fabricated with 160 nm diameter nanosphere etch mask. In-plane width = 44.9 ± 3.8 nm. (C) Etch time = 1 minute, rf power = 26 Watts.

indicate that they are nanopores. Predicted in-plane widths were calculated from equation 1 for the nanopores shown in Figure 2.3 and were found to be 167 nm, 67 nm, and 37 nm corresponding to nanosphere etch masks with diameters of 720 nm, 290 nm, and 160 nm, respectively.

2.3.2 Analysis of Nanopore Dimensions by AFM

Figure 2.4 is a plot of experimental and predicted (from equation 1) nanopore in-plane widths as a function of nanosphere diameter. The experimental in-plane widths are always found to be greater than those predicted from equation 1. This discrepancy can be attributed to three factors. The first factor is the convolution of the AFM tip radius of curvature with the nanopore resulting in systematic errors in the measured in-plane widths.[52] The experimental values have a y-intercept of -7.84 nm. This deviation is also a consequence of AFM tip convolution.

The second factor is that since the nanospheres contain only one point of direct contact with the substrate, the etchant can access the substrate underneath the nanosphere mask (under-etching). The third factor is that the etching species may scatter off the NSL mask and in doing so, create nanopore apertures that are larger than would otherwise be predicted. While the theoretical model does not quantitatively predict the nanopore in-plane widths, the fabricated nanopore dimensions were a linear function of nanosphere diameter, therefore the fabricated nanopore in-plane widths can be designed to a predetermined size. The slope of the experimental values is a factor of 2 larger than the slope of the theoretical values. The origin of the factor of 2 slope difference is due to under-etching as well as scattering of the etching species. The etchant has more access to etch underneath large nanospheres than small nanospheres. Furthermore, the larger nanospheres provide a wider angular distribution for the scattered etching species resulting in larger nanopore apertures.

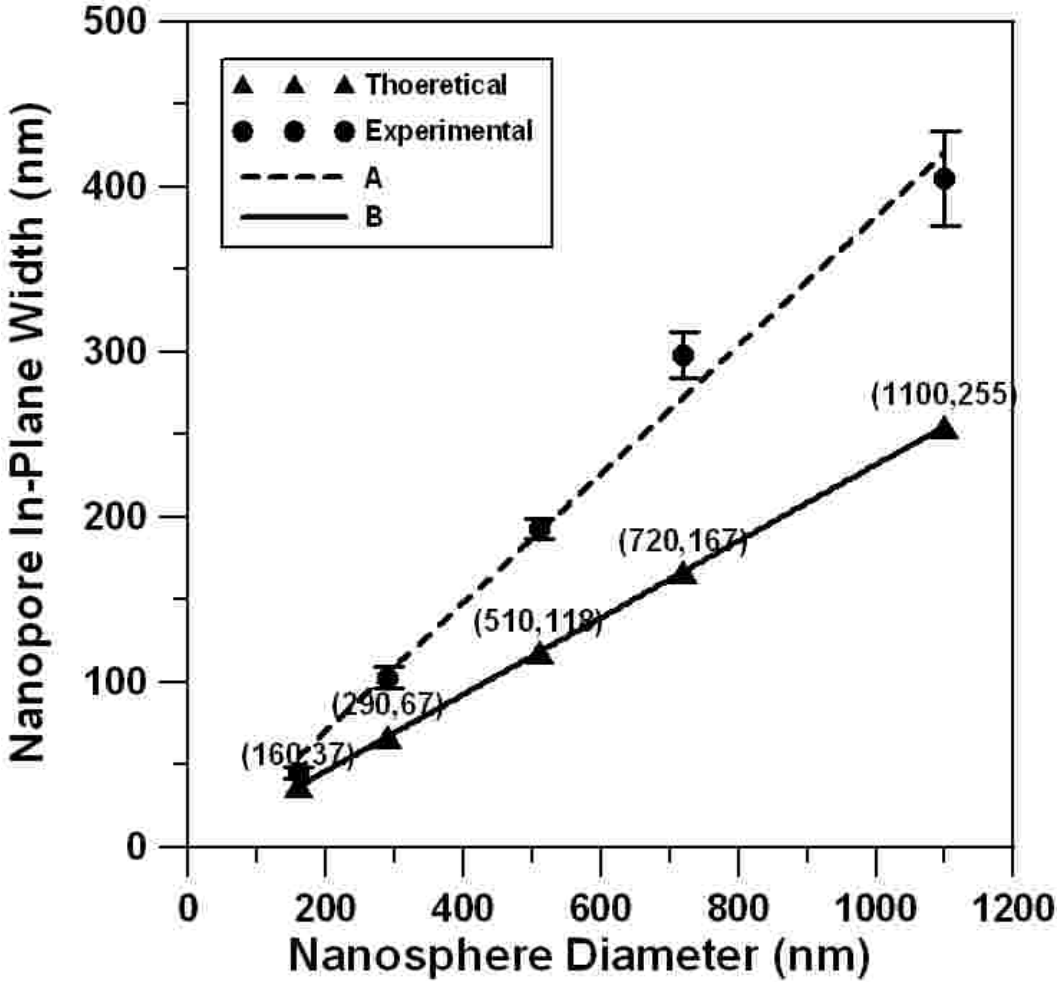

Figure 2.4 Plot of both experimental and theoretical nanopore in-plane width with relation to nanosphere etch mask diameters. (A) Y = 0.4X-7.8, R^2 = 0.9883 (B) Plot of equation 1: $a = \frac{3}{2}\left(\sqrt{3} - 1 - \frac{1}{\sqrt{3}}\right)D$ with coordinates that correspond to experimental data.

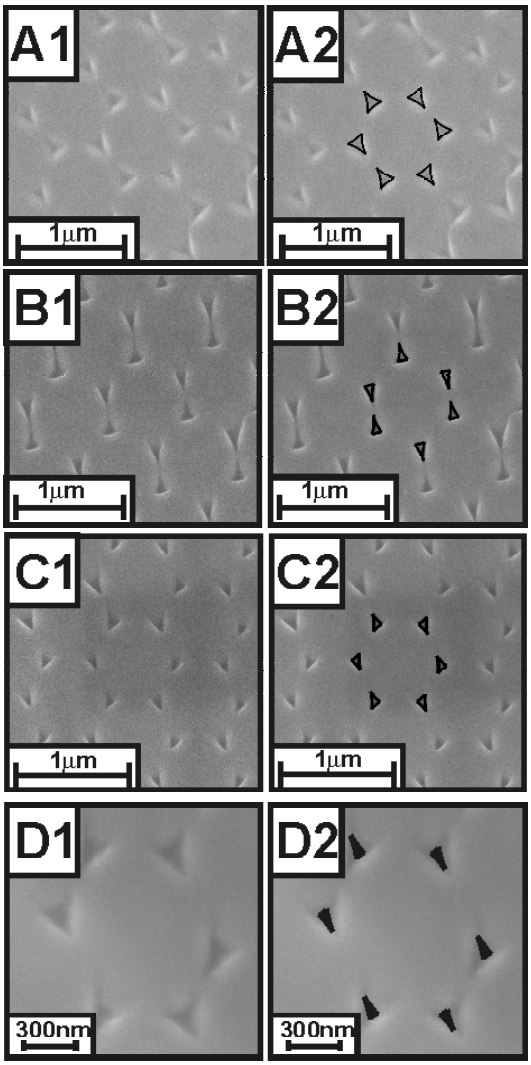

Figure 2.5 SEM images of nanopores fabricated using AR NSL and images with simulated superimposed geometries, respectively. (A1, A2) Θ = 20º; Φ = 5º, (B1, B2) Θ = 30º; Φ = 1º, (C1, C2) Θ = 30º, Φ = 24º, and (D1, D2) Θ = 40º, Φ = 10º. All nanopores were made with 720 nm nanosphere etch masks on Si (111). Etch time = 2 minutes.

2.3.3 Reactive Ion Etching Variant of Angle-Resolved Nanosphere Lithography

The RIE variant of AR NSL yields a further reduction in nanopore in-plane widths by approximately a factor of 3. Furthermore, a variety of nanopore aperture shapes are possible with AR NSL. Figure 2.5 depicts SEM images of the resulting nanopores (2.5A-1, 2.5B-1, 2.5C-1, and 5D-1) paired with their theoretically predicted geometric representations (2.5A-2, 2.5B-2, 2.5C-2, and 2.5D-2). All nanopore structures shown in Figure 2.5 were designed with 720 nm diameter etch masks. A range of Θ (20º-40º) and Φ (1º-24º) values were used in the modeling. One can see how drastically the angle Φ affects the final nanopore dimensions. Figures 2.5B and 5C show nanopores that have both been etched at Θ=30º while their Φ values vary dramatically. The resulting pore aperture shapes are significantly different. The in-plane widths ranged from 93 nm to 177 nm, demonstrating a three-fold decrease in the dimensions of the nanopore aperture. The geometrically predicted representations of the pore apertures corresponded well with small values of Θ (≤ 30º) seen in the SEM images (Figures 2.5A-2, 2.5B-2, and 2.5C-2). However, as seen in Figure 2.5D-2, at larger values of Θ the predicted geometric representations fail to match well with the experimental results. The nanopores fabricated at Θ = 40º were significantly larger than the predicted geometry. This deviation can be attributed to the fact that at large values of Θ, significant under-etching of the nanosphere mask occurs. One can expect that as Θ increases, the fabricated nanopores will deviate further from their predicted geometry because under-etching. Furthermore, tilting of the substrate will affect the uniformity of the etching parameters which would become more significant as Θ increases resulting in further deviation of the experimental nanopore geometry from the predicted nanopore geometry.

2.4 Conclusions

In conclusion, we have shown that the RIE variant of NSL and AR NSL can be employed to make sub-100 nm triangular nanoporous which have potential applications in catalysis, optics, magnetics, sensing, molecular separation, molecular dynamics, and single molecule detection. The nanopores presented here have the following unique characteristics: (1) uniform in-plane-widths (44 nm - 404 nm), (2) controlled depth (25 nm – 250 nm), (3) controlled shapes, and (4) high areal density (~10^{10} pores cm^{-2}). Furthermore we have shown that AR NSL provides an additional three-fold reduction in the in-plane width of the nanopores. Because the in-plane width has been shown to be linearly dependent on nanosphere diameter, the fabrication of pre-determined, size-tunable nanopores is possible. AR NSL provides additional control of nanopore dimension by utilizing the parameters, Θ and Φ. This technique was employed to etch nanopores through 720 nm diameter nanosphere etch masks with in-plane widths ranging from 93-177 nm, resulting in a three-fold reduction in nanopore dimensions compared to those fabricated with $\Theta = 0^{\circ}$. The nanopore geometries fabricated with AR NSL and RIE corresponded well with the theoretically determined geometries for values of $\Theta \leq 30^{\circ}$. Because of their size uniformity, these nanopores provide the ideal template to fabricate a variety of optical and magnetic nanoparticles. Future work will focus on extending this nanopore fabrication technique to a variety of substrates for applications in nanoparticle optics, nanomagnetics, and catalysis.

Chapter 3

The Localized Surface Plasmon Resonance Nanosensor: A High Resolution Distance Dependence Study Using Atomic Layer Deposition

3.1 Introduction

The localized surface plasmon resonance (LSPR) wavelength shift response, $\Delta\lambda_{max}$, of Ag nanoparticles fabricated by nanosphere lithography (NSL) has been used to develop a new class of nanoscale optical biosensors.[1-5] On the most elementary level, the LSPR wavelength shift response of these sensors can be understood using a model of the refractive-index response of propagating surface plasmons on a planar noble metal surface:[53]

$$\Delta\lambda_{max} = m\Delta n\left[1 - \exp\left(-2d / l_d\right)\right] \tag{1}$$

where $\Delta\lambda_{max}$ is the wavelength shift, m is the refractive-index sensitivity, Δn is the change in refractive index induced by an adsorbate, d is the effective adsorbate layer thickness, and l_d is the characteristic electromagnetic field decay length. This model assumes a single exponential decay of the electromagnetic field normal to the planar surface, which is accurate for a propagating surface plasmon, but is undoubtedly an oversimplification for the electromagnetic fields associated with noble metal nanoparticles. While this oversimplified model does not quantitatively capture all aspects of the LSPR nanosensor response, it does provide some guidance for sensor optimization. In particular, Equation (1) highlights the importance of distance dependence as described by the of the electromagnetic field decay length, l_d.

Haes and co-workers explored the long range distance dependence of the LSPR nanosensor using self-assembled monolayers (SAMs) of 11-mecaptoundecanoic acid (11-MUD) and Cu^{2+} ions adsorbed on arrays of noble metal nanoparticles with various sizes, shapes, and compositions.[14] The spatial resolution of this experiment was limited to the thickness of the 11-MUD/ Cu^{2+} monolayer which was at least 1.6 nm. Several interesting characteristics of the long-range behavior were found including: (1) the LSPR shift vs. SAM thickness is nonlinear; (2) Ag

nanoparticles are more sensitive than Au nanoparticles; (3) nanotriangles have larger sensing distances than nanohemispheroids; (4) increasing the nanoparticle in-plane width results in larger sensing distances; and (5) decreasing nanoparticle out-of-plane height results in larger sensing distances.[14] Semi-quantitative theoretical calculations revealed that the plasmon resonance shift is controlled by the average electromagnetic field over the nanoparticle surface.[14]

Similarly, the short range distance dependence (0-3 nm) of the LSPR nanosensor has been studied using alkanethiol, $CH_3(CH_2)_xSH$ (x = 2-11, 13-15, and 17), monolayers.[54,55] It was found that Equation 1 does a remarkably good job of accounting for the short range LSPR response if one assumes a value l_d = 5–6 nm. In addition, the dependence of $\Delta\lambda_{max}$ on the chain length of the alkanethiol monolayer was found to be linear, with a large slope of 3.1 -3.3 nm per CH_2 unit.[55]

Even though much important information was obtained from these previous long and short range distance dependence studies, it was hypothesized that new information could be obtained if it were possible to deposit single layers of a material with thicknesses of ~1 Å. Furthermore, while the refractive index of the bulk SAM molecule is known, the refractive index of the SAM is not known making an accurate theoretical model of the experiment difficult.[14]

Atomic layer deposition (ALD) is just such a fabrication method that produces highly uniform and controlled thin films. Precursor gases are alternately pulsed through the reactor and purged away resulting in a self-limiting growth process that constructs a film one monolayer at a time.[56] Highly uniform monolayers of Al_2O_3 can be deposited with ~1 Å thickness resolution and a refractive index of 1.57.[15,16] Depositing Al_2O_3 multilayers onto the noble metal nanosensor should allow the long range distance dependence of the LSPR nanosensor to be probed with 10x spatial resolution compared with previous work.[14]

In this paper, we have utilized ALD of Al_2O_3 to probe both the long and short range LSPR distance dependences of Ag nanoparticles in one integrated experiment. The following results are presented: (1) A detailed study of the long distance dependence of the LSPR sensor with 10x increased spatial resolution afforded by ALD in comparison with earlier experiments with SAMs; (2) LSPR nanosensors are shown to have single Al_2O_3 layer detection capabilities; and (3) at short range, triangular nanoparticles with fixed widths and smaller out-of-plane heights have larger LSPR sensing distances. A semi-quantitative theoretical analysis of the long and short range distance dependence of the LSPR sensor is presented. Furthermore, the nucleation and growth of Al_2O_3 on Ag surfaces was studied using quartz crystal microbalance (QCM), variable angle spectroscopic ellipsometry (VASE), and X-ray photoelectron spectroscopy (XPS) measurements. These measurements reveal that the Al_2O_3 deposits on the LSPR Ag surface in a layer-by-layer fashion and the initial nucleation may proceed via the thermal decomposition of trimethylaluminum on the Ag.

3.2 Experimental and Methods

3.2.1 Materials

Ag (99.99%) was purchased from D. F. Goldsmith (Evanston, IL). Borosilicate glass substrates, No. 2 Fisherbrand 18-mm circular coverslips were acquired from Fisher Scientific (Pittsburg, PA) and P-doped Si (111) was obtained from Wacker Siltronic (Portland, OR). Hexanes, methanol, H_2SO_4, H_2O_2, and NH_4OH were purchased from Fischer Scientific (Fairlawn, VA). Surfactant-free carboxyl-terminated polystyrene nanospheres with 390 nm (± 19.5 nm) diameters were received in a suspension of water from Duke Scientific (Palo Alto, Ca).

Absolute ethanol was acquired from Pharmco (Brookfield, CT). Millipore cartridges (Marlbourough, MA) were used to purify water to a resistivity of 18 $M\Omega cm^{-1}$. Al_2O_3 films were fabricated by ALD utilizing TMA purchased from Sigma Aldrich (Milwaukee, WI) and deionized water.

3.2.2 Nanosphere Lithography

NSL was used to fabricate monodispersed, surface-confined Ag nanoparticles.[57] Glass and Si (111) substrates were cleaned in a piranha etch solution (30% 3:1 H_2SO_4/H_2O_2) for 30 min at 80 ºC. After rinsing with water, the substrates were sonicated for 60 min in 5:1:1 $H_2O/H_2O_2/NH_4OH$ in order to create a hydrophilic surface on the substrate to facilitate self-assembly of the nanosphere masks. Finally, the substrates were rinsed and stored in water for future use. 2D self-assembled monolayer masks of nanospheres were fabricated by drop-coating approximately 2.5 μL of undiluted nanosphere solution (10% solid) on the pretreated substrates. The nanospheres were allowed to dry in ambient conditions. Ag was deposited by electron beam (e-beam) deposition in a Kurt J. Lesker Axxis e-beam deposition system (Pittsburg, PA) with a base pressure of 10^{-6} Torr. The mass thickness and deposition rate (1 Å/sec) was monitored using a Sigma Instruments 6 MHz gold plated QCM (Fort Collins, Colorado). After the Ag deposition, the nanosphere masks were removed by sonication in absolute ethanol for 3 min. Hemispheroidal Ag nanoparticles were fabricated by annealing Ag triangular nanoparticles at 300ºC for 1 hr at ~1 Torr under N_2.

3.2.3 Nanoparticle Annealing

The Ag nanoparticles were solvent annealed using hexanes and methanol in a home build flow cell to ensure the stabilization of the LSPR extinction spectra.[54] Dry N_2 gas and solvent

were cycled through the flow cell until the λ_{max} of the nanoparticle arrays was stabilized. The samples were then rinsed with absolute ethanol and dried under N_2.

3.2.4 Atomic Layer Deposition

Al_2O_3 films were fabricated on the Ag nanoparticles by ALD. The reactor utilized in these experiments is similar to previous publications.[58] TMA and deionized H_2O vapors were alternately pulsed through the reaction chamber utilizing N_2 as the carrier gas at a mass flow rate of 360 sccm and a pressure of 1 Torr using a growth temperature of 50 ºC. Al_2O_3 ALD proceeds on a hydroxylated surface according to scheme 1.[16]

Scheme 1

(A) $Al\text{-}OH^* + Al(CH_3)_3 \rightarrow Al\text{-}O\text{-}Al(CH_3)_2^* + CH_4$

(B) $Al\text{-}CH_3^* + H_2O \rightarrow Al\text{-}OH^* + CH_4$

The asterisks (*) signify the surface species.

Figure 3.1 depicts a simplified schematic diagram of the ALD reactor. One complete AB cycle is 42 s: (1) TMA reactant exposure time = 1 s, (2) N_2 purge following TMA exposure time = 10 s, (3) H_2O reactant exposure time = 1 s, (4) N_2 purge following H_2O exposure time = 30 s. Long purge times are necessary at low temperatures to prevent chemical vapor deposition (CVD) of Al_2O_3.[16]

3.2.5 X-ray Photoelectron Spectroscopy

The surface composition of a 50 nm Ag film deposited by e-beam on glass was analyzed by XPS. The measurements were performed using Mg*Kα* (1253.6 eV) radiation and a hemispherical electron energy analyzer (HEA). The spectra were recorded in fixed absolute resolution (FAT) mode of the HEA with pass energy of 44 eV (for survey spectra) and 22 eV (for detailed measurements of core level peaks). The electrons were collected from the area with

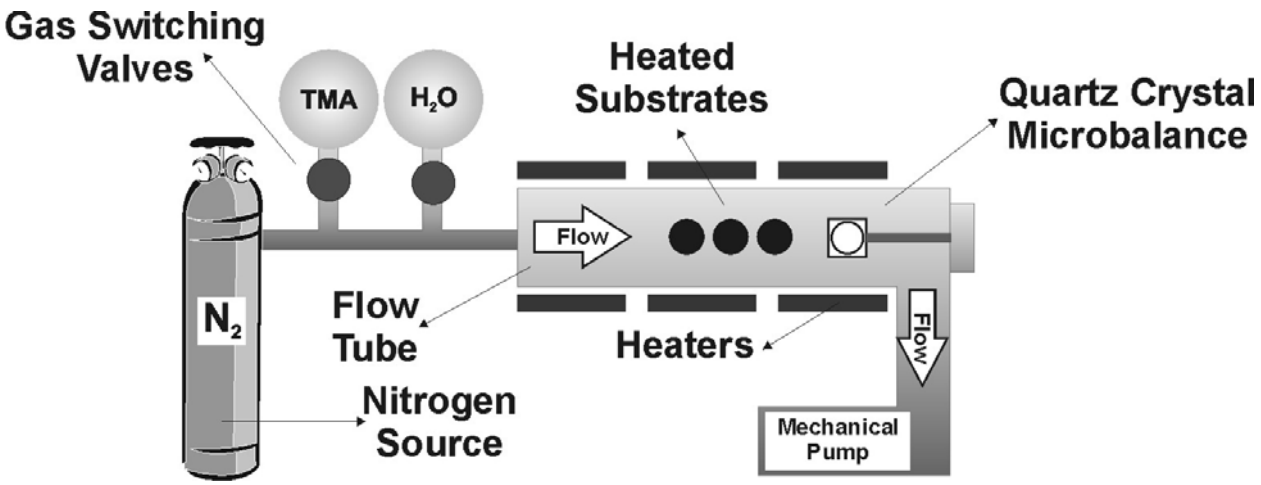

Figure 3.1. Schematic representation of the ALD system.

an elliptical shape with dimensions of 4 mm x 3 mm. Survey spectra with an energy step of 1eV and precision measurements of core level photoelectron lines C*1s*, Si*2p*, O*1s*, Cl*1s* as well as a valence band with the energy step of 0.2 eV were recorded. The spectrometer calibration was performed using the gold XPS emission line (Au$4f_{7/2}$ with a binding energy of 84 eV). The residual vacuum in the analyzing chamber was 4 x 10^{-10} mbar. Processing of the obtained XPS spectra was performed using the CasaXPS software. All measured peaks were corrected for inelastic scattering by subtracting the Shirley background from the raw spectra, followed by the fitting of peaks by using the asymmetric pseudo-Voigt shape peaks with different relative content of Gaussian and Lorentzian components.

3.2.6 Variable Angle Spectroscopic Ellipsometry

Al_2O_3 film thicknesses were measured by VASE using an M-2000V from J. A. Wollam Co.. VASE measurements were taken on Al_2O_3 ALD films fabricated on a 50 nm Ag film deposited by e-beam. The Al_2O_3 ALD on the Ag film was done concurrently with Al_2O_3 ALD on the Ag nanoparticles.

3.2.7 Quartz Crystal Microbalance Measurements

Details of the *in situ* QCM measurements have been reported previously.[58] Briefly, the QCM experiments utilized polished sensors (Colorado Crystal Corporation, Part #CCAT1BK-1007-000) installed in a Maxtek BSH-150 bakeable sensor head. Prior to installation, an Ag film with a thickness of 50 nm was deposited onto the QCM sensor by e-beam . To prevent deposition on the back surface of the sensor during the ALD experiments, the sensor housing was continuously purged with ultrahigh purity N_2 and the gap between the front surface of the sensor and the crystal holder was filled using a high temperature conducting epoxy (Epotek P1011). To minimize temperature-induced apparent mass changes, a uniform temperature

distribution was established near the QCM by adjusting the temperature setpoints and heater power distribution of four separate temperature-controlled heating zones.[59] The QCM signals were monitored using a Maxtek TM400 thickness monitor with a mass resolution of 0.375 ng/cm^2 (0.01 Å Al_2O_3) at 10 measurements per second.

3.2.8 UV-Vis Extinction Spectroscopy

LSPR extinction measurements of the Ag nanoparticle arrays were obtained using the M-2000V in transmission mode.

3.2.9 Scanning Electron Microscopy (SEM)

Various Al_2O_3 film thicknesses on triangular Ag nanoparticles on Si (111) were observed with a Hitatchi S-4700-II SEM. Images were collected with 10.0 kV.

3.3 Results and Discussion

3.3.1 SEM of Ag Nanotriangles

SEM images of bare and Al_2O_3 coated Ag nanotriangles on Si (111) were acquired. Si (111) was chosen as the substrate to minimize charging and to produce high quality images. Nanoparticles fabricated on Si (111) substrates are similar to those fabricated on glass substrates. Figure 3.2 presents SEM images of bare Ag nanoparticles (Fig. 3.2A) and Ag nanoparticles coated by Al_2O_3 ALD using 100 (Fig. 3.2B), 200 (Fig. 3.2C), 400 (Fig. 3.2D), and 600 (Fig. 3.2E) AB cycles. Figure 3.2F depicts a plot of the nanoparticle in-plane width vs. AB cycles determined from the SEM images and yields a growth rate of 0.9 Å/cycle.

3.3.2 Ellipsometry

VASE studies were carried out to accurately monitor the Al_2O_3 film thickness and growth rate. Measurements were carried out on a 50 nm Ag film e-beam deposited on glass. Figure 3.3

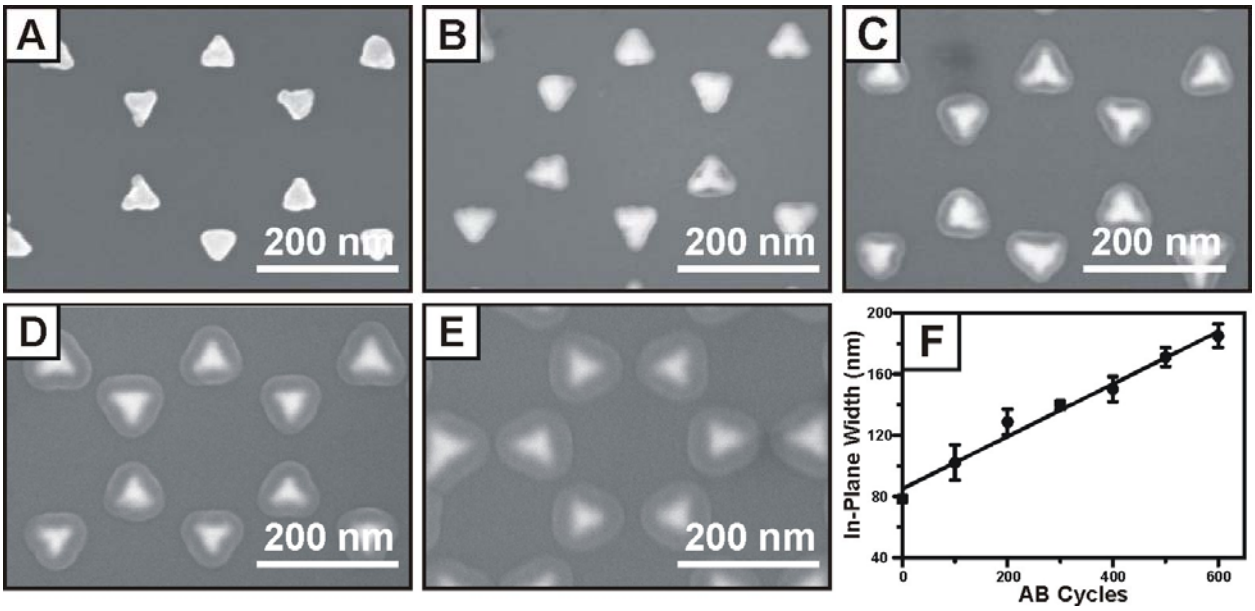

Figure 3.2 SEM images of (A) bare Ag nanoparticles (a = 90 nm, b = 51 nm) and Ag nanoparticles following (B) 100, (C) 200, (D) 400, and (E) 600 AB cycles of TMA/H_2O. (F) Plot of in-plane Ag triangle width versus AB cycles determined from SEM images.

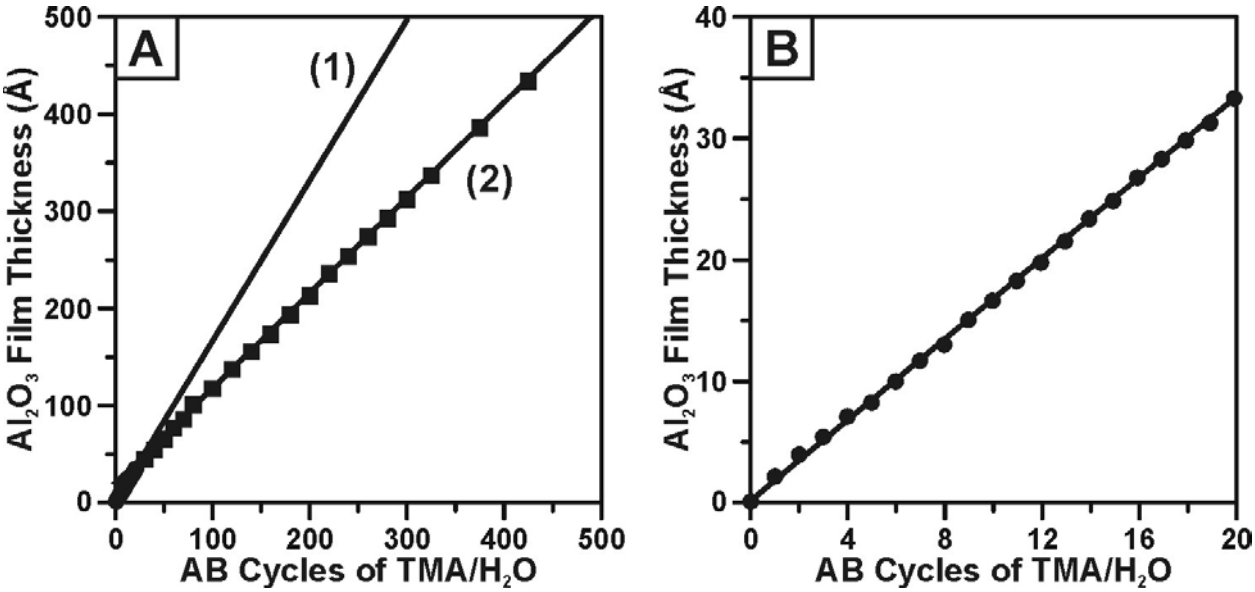

Figure 3.3 Ellipsometry measurements for Al_2O_3 ALD grown on a 50 nm Ag film. (A) Ellipsometry data for 0-425 AB cycles of TMA and water. Circles denote single AB cycles of TMA and water and squares denote multiple AB cycles of TMA and water. (B) Ellipsometry data for 0-20 AB cycles TMA and water. Circles denote single AB cycles of TMA and water. Growth rate for 0-20 AB cycles (1) = 1.65 Å per cycle. Growth rate for 30-425 AB cycles (2) = 0.98 Å per cycle.

plots the Al_2O_3 film thickness vs. AB cycles of TMA and water deposited on a Ag-coated Si (111) surface measured with VASE. VASE data is presented for 0 - 425 AB cycles (Fig. 3.3A). Two growth rates are observed: growth rate for 0 - 20 AB cycles = 1.65 Å per cycle (Fig. 3.3A-1) and the growth rate for 20 – 425 AB cycles = 0.98 Å per cycle (Fig. 3.3A-2). Figure 3.3B depicts the VASE data for just the 0 - 20 AB cycles. Both growth rates are extremely linear with R^2 = 0.9934 and 0.9998 for (3.3A-1) and (3.3A-2), respectively and can therefore be easily predicted and controlled. The higher growth rate (1.65 Å per cycle) measured during the first 20 AB cycles is a consequence of a much larger H_2O exposures resulting from removing the sample from the reaction chamber and exposing the sample to room air after each AB cycle to collect an extinction spectrum. The Al_2O_3 ALD growth rate increases with increasing water exposures.[60] The growth rate then reduces to 0.98 Å per cycle once multiple AB cycles of TMA and water are employed (Fig. 3.3A-2). This growth rate is very close to the value determined from the SEM measurements (Fig. 3.2F) and is typical for ALD Al_2O_3 on hydroxylated SiO_x under these conditions.[16]

3.3.3 XPS Measurements on Ag Film

Given that the Al_2O_3 ALD growth mechanism requires surface hydroxyl groups (Scheme 1), it was surprising that the Al_2O_3 ALD proceeds at the same rate on Ag as on hydroxylated SiO_x without apparent inhibition or nucleation delay. Hydroxyl groups may be present if the Ag surface is oxidized, however VASE detected no AgO before or after the Al_2O_3 ALD. Further measurements were made using XPS, an extremely sensitive probe for surface composition. XPS was preformed on a 50 nm Ag film e-beam deposited on glass. Figure 3.4 presents XPS measurements on a 50 nm Ag film e-beam deposited on glass obtained before (Fig. 3.4A) and after (Fig. 3.4B) annealing the Ag film at ~200ºC for 40 min. Figure 3.4A shows 10.5 % oxygen

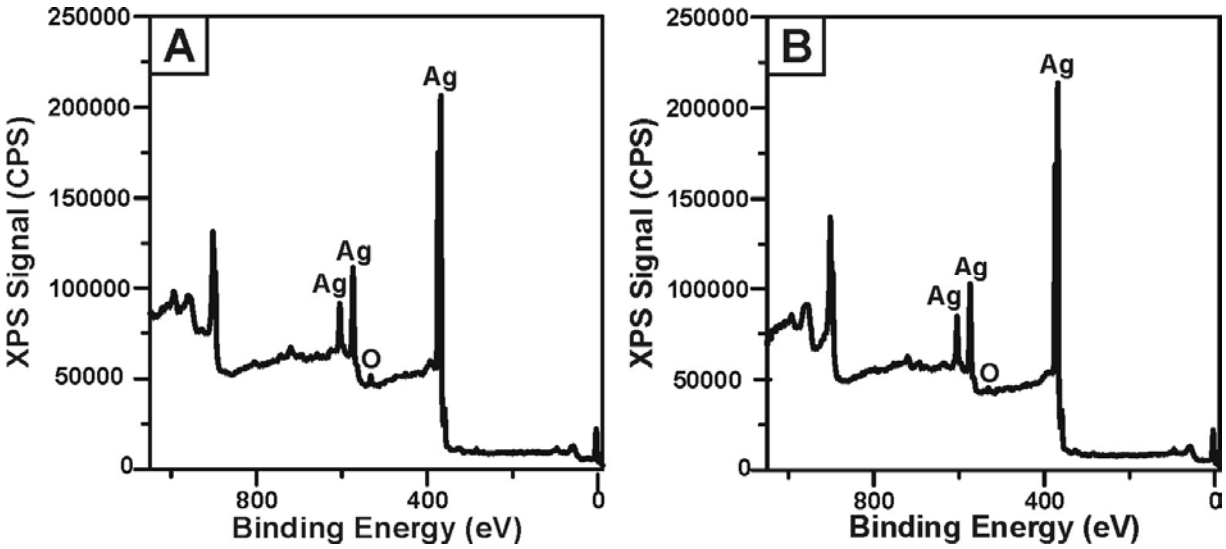

Figure 3.4 XPS measurements on 50 nm Ag film. (A) XPS measurements taken on the Ag film as deposited. 10.5% oxygen was found on the Ag film surface. (B) XPS measurements taken on the Ag film after annealing for 40 minutes under UHV at ~200ºC. 5.6% oxygen was on the Ag film surface.

content on the surface of the Ag film. After annealing the substrate the oxygen content on the Ag film surface drops to 5.6 % (Fig3. 4B). The oxygen XPS peak does not appear at the expected position for AgO (~528-532 eV) indicating that the oxygen peak results from surface impurities.[61]

3.3.4 QCM measurements on Ag Film

Further exploration of the Al_2O_3 growth mechanism on Ag was done by QCM studies (Figure 3.5). QCM measurements were conducted on 50 nm Ag film e-beam deposited directly on the QCM crystal. Figure 3.5A shows the QCM measurements recorded during 100 AB cycles of Al_2O_3 ALD. The QCM signals have been converted to Al_2O_3 thickness assuming a density of 2.6 g/cm^3.[62] The Al_2O_3 growth is extremely linear with a growth rate of 1.0 Å/cycle in excellent agreement with the VASE and SEM results. Moreover, there is no indication of inhibited initial growth as might be expected for Al_2O_3 ALD on a noble metal surface. The step-like structure in Figure 3.5A reflects the discrete mass changes produced by the individual TMA and H_2O exposures. Expanded views of the QCM data at early and late times are given in Figures 3.5B and 3.5C, respectively. The shaded areas represent the time periods that the TMA and water dosing valves were open.

The QCM structure in Figure 3.5B reveals details about the mechanism for Al_2O_3 nucleation and growth on Ag. Figure 3.5B shows a large thickness change of 3 - 4 Å during the first TMA exposure. Given that XPS and VASE detect no AgO and little surface oxygen, the TMA must react directly with the Ag. Although this reaction has not been studied, TMA reacts with Ni(111) to form a monolayer of $Al(CH_3)_2$ and CH_3 surface species even at low temperatures of 110 K.[63] During the initial Al_2O_3 ALD cycles on Ag, the thickness decreases during the TMA purge periods (Figure 3.5B). This may be a result from the desorption of physisorbed H_2O or the

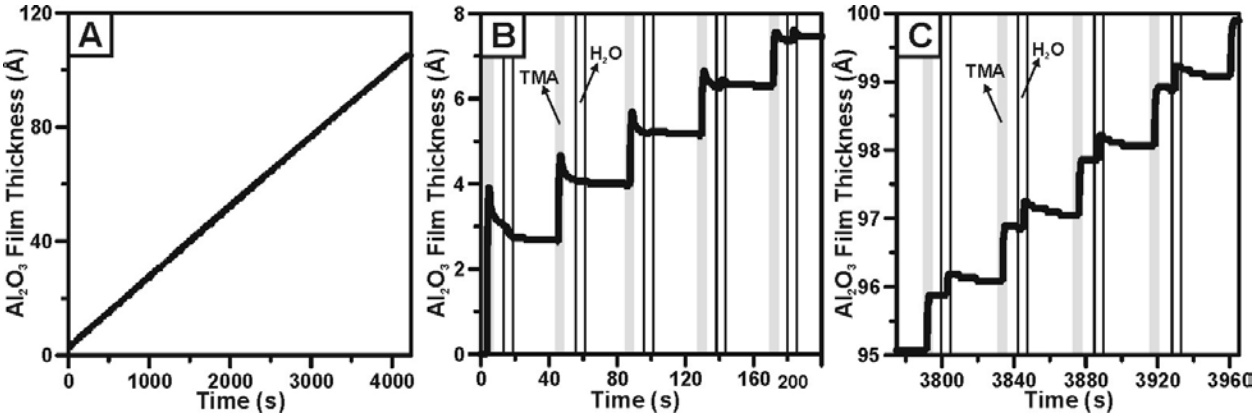

Figure 3.5 Plots of Al_2O_3 growth rate and QCM step ratio vs. AB cycles of TMA and water measured with QCM on 50 nm Ag film. (A) QCM measurements for 0-100 AB cycles of TMA and water. (B) QCM measurements for the first 5 AB cycles of TMA and water. (C) QCM measurements for the final AB cycles of TMA and water. 50 nm Ag was deposited on the QCM to insure similar experimental environment. The shaded areas represent the time periods that the TMA and water dosing valves were open.

recombinative desorption of surface OH groups. *In situ* quadrupole mass spectrometry measurements would verify these desorption processes.[64]

There is a net thickness decrease following the H_2O doses and purges at early times (Figure 3.5B) and a net thickness increase at later times (Figure 3.5C). This net change reflects the density of surface OH groups: larger net increases result from larger OH group coverages.[64] The net thickness change is negative in Figure 3.5B because there are no OH groups on the metallic Ag surface. However, the net thickness change is positive (Figure 3.5C) because the ALD Al_2O_3 surface is fully hydroxylated at 50ºC. Approximately 20 AB cycles are required for the net thickness to reach the steady-state value shown in Figure 3.5C.

To summarize, our results indicate nearly ideal layer-by-layer growth of the ALD Al_2O_3 on the Ag surfaces. Both the VASE and QCM measurements (Figures 3.3 and 3.5) demonstrate highly linear Al_2O_3 growth on planar Ag surfaces without any initial delay. The nucleation may result in part from the reaction of TMA with surface hydroxyls bound to a thin native oxide layer on the Ag. However, the coverage of this oxide layer must be very small (<10%) as shown by XPS (Figure 4). Alternatively, nucleation may occur by the direct reaction of TMA with the Ag surface and evidence for this mechanism is given by the large, initial mass increase shown in the QCM data (Figure 3.5B). The SEM analysis also supports layer-by-layer Al_2O_3 growth on the Ag nanoparticles (Figure 3.2). These results greatly simplify the interpretation of the LSPR spectroscopy of the Ag nanoparticles because the thickness of the Al_2O_3 overlayers can be deduced easily from the number of ALD cycles.

3.3.5 LSPR Spectroscopy of Ag Nanoparticles

3.6 depicts LSPR extinction spectra for triangular Ag nanoparticles with an in-

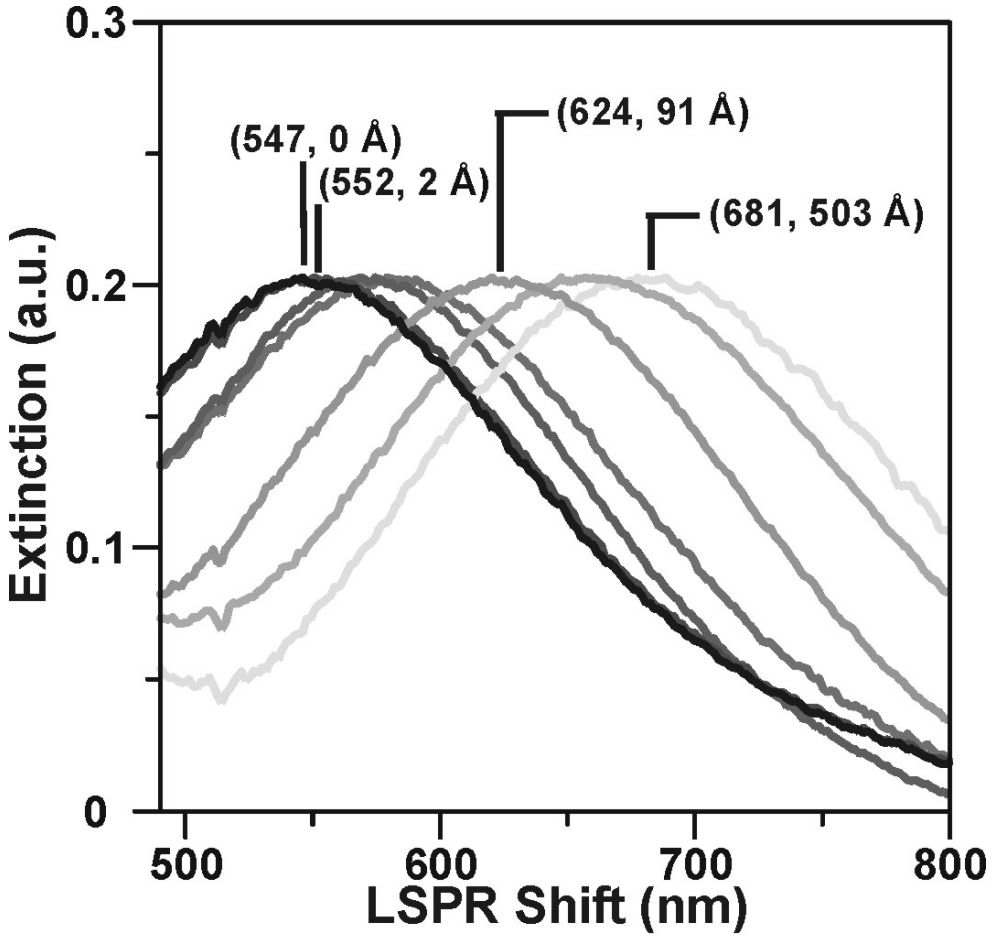

Figure3.6 LSPR spectroscopy of Ag nanoparticles (a = 90 nm, b = 40 nm) for 0-450 AB cycles of TMA and water.

plane width (a) of 90 nm and out-of-plane height (b) of 40 nm. The UV-Vis spectra for Ag nanoparticles with 0 - 450 cycles of TMA and water is presented in Figure 3.6. As subsequent ALD Al_2O_3 layers are completed, the LSPR λ_{max} position red shifts which is consistent with previous work.[14] Importantly, these results clearly demonstrate that the LSPR nanosensor has sufficient sensitivity to detect the deposition of each successive Al_2O_3 monolayer. For nanoparticles with a = 90 nm and b = 40 nm a 5 nm LSPR λ_{max} shift is observed with 2 Å of Al_2O_3. Furthermore, by extrapolation it should be possible to detect sub-monolayers of material. ALD of Al_2O_3 allows for the fabrication of Angstrom thick monolayers which gives this work a 10x increase in the spatial resolution compared to previous work.[14]

3.3.6 LSPR Shifts vs. Al_2O_3 Film Thickness

Figure 3.7 depicts plots of the LSPR λ_{max} shift vs. Al_2O_3 film thickness for triangular nanoparticles with a = 90 nm and b = 30 nm (1), 40nm (2), 51 nm (4), and hemispheroidal nanoparticles with a = 104 nm and b = 54 nm (3). In Figure 3.7A the LSPR λ_{max} shift vs. Al_2O_3 film thickness response is shown for 0 - 600 AB cycles. These results compare well with previous work.[14] At short distances from the nanoparticle surface, the LSPR λ_{max} shift follows a steep linear slope, but as the distance from the nanoparticle increases, the curve bends over, and eventually levels off once the nanoparticle has reached its saturation point. As the nanoparticle height decreases and the in-plane width remains constant, the LSPR λ_{max} shift increases which again agrees with previous results.[14] The short range distance dependence is highlighted in Figure 3.7B which depicts the λ_{max} shift vs. Al_2O_3 film thickness response for the first 0 - 20 AB cycles. After each cycle a LSPR extinction spectrum was collected which presents a highly detailed view of the short range distance dependence of the LSPR nanosensor. Because Al_2O_3 layers deposited by ALD are ~ 1.1 Å in thickness[15] this is the first time that an extremely

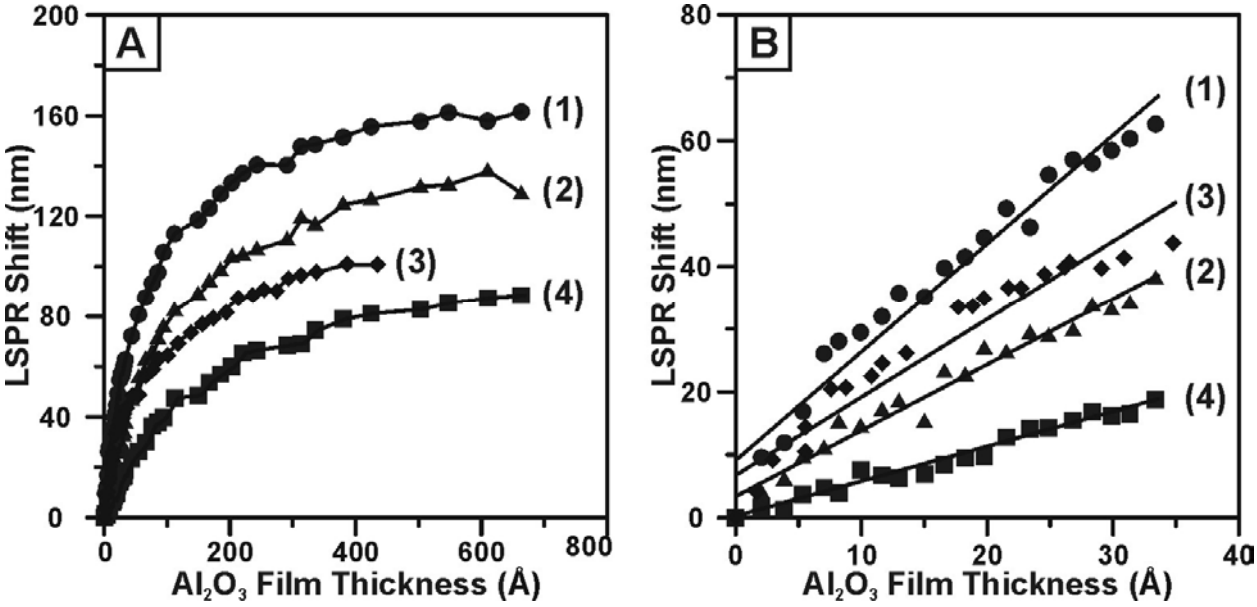

Figure 3.7 Plot of LSPR shift vs. Al_2O_3 film thickness. (A) Out-of plane height dependence on the long and short range distance dependence for Ag triangular nanoparticles a = 90 nm and b = (1) 30 nm, (2) 40 nm, and (4) 51 nm and Ag hemispherical nanoparticles a = 104 nm and b = 52 nm (3). Data presented for 0-600 AB cycles of TMA and water. (B) Out-of-plane height dependence of the short range distance dependence for the Ag triangular nanoparticles a = 90 nm and b = (1) 30 nm, (2) 40 nm, and (4) 51 nm and Ag hemispherical nanoparticles a = 104 and b = 52 nm (3). Data presented for 0-20 AB cycles of TMA and water. Linear regression was used to fit the data to lines described by the following equations: $y = 1.7x + 9.1$; $R^2 = 0.9602$ (1), $1.0x + 3.5$; $R^2 = 0.9689$ (2) $1.2x + 7.0$; $R^2 = 0.9293$ (3), and $y = 0.5x + 0.1$; $R^2 = 0.9744$.

detailed picture of both the short and long range distance dependences of the LSPR nanosensor have been obtained in a single integrated experiment. In fact, the results in this work show that at short distances from the nanoparticle surface, the LSPR λ_{max} shift vs. layer thickness follows a steep linear trend compared with the moderate slope at larger distance from the nanoparticle surface. Nanoparticles with fixed in-plane widths and decreasing out-of-plane heights yield larger sensing distances (Fig. 3.7B-1) as has been observed at larger distances from the nanoparticle surface.[14] The scatter in these plots results from slight misalignments resulting from repositioning the LSPR samples between measurements as the samples were moved between the ALD reactor and the spectrometer. We expect the scatter to be reduced greatly if the extinction spectra are recorded in situ, and work is currently underway to construct a new ALD reactor with in situ optical capability. Nevertheless, the data in Figures 3.6 and 3.7 clearly demonstrate that the LSPR sensors possess Angstrom-level sensitivity to the Al_2O_3 thickness changes.

Previous results have shown that hemispheroidal nanoparticles have a smaller sensing distance than triangular nanoparticles of similar volume.[14] Unexpectedly, Figure 3.5B-3 shows that the hemispheroidal particles (a = 104 nm and b = 52 nm) presented here have a larger LSPR λ_{max} shift at long distances compared with triangular nanoparticles with a = 90 nm and b = 51 nm (Figure 3.7A-4). Also, at short distances from the nanoparticle surface, the hemispheroidal particles have larger LSPR λ_{max} shifts than both triangular nanoparticles with a = 90 and b = 39 nm and 51 nm.

3.3.7 Theory

Using the discrete dipole approximation (DDA) method,[65-68] we modeled the LSPR λ_{max} shift measurements for silver particles coated with multilayers of Al_2O_3. In this method, the

particle and Al_2O_3 coating are represented using a cubic grid of polarizable elements, with the polarizability of each element determined by the local dielectric constant. The particles are represented either as a truncated tetrahedron or as a hemispheroid, with dimensions taken to match the experimental results. The grid size in these calculations is 2 nm and the wave vector is taken perpendicular to the bottom surfaces of the truncated tetrahedron or hemispheroid. The refractive index of silver is taken from Hunter and Lynch[69] and that for the adsorbate Al_2O_3 is taken to be 1.57 from the experimental data. The resonance wavelength of the truncated tetrahedron shaped silver particles was calculated with the layer thickness of the Al_2O_3 taken to be the grid size, 2 nm. This is not same as the layer thickness of Al_2O_3, however, the dependence of the LSPR λ_{max} shifts on the layer thickness are not sensitive to this difference for layers that are more than around 5 nm thick. (as is apparent from Figure 3.8). Figure 3.8 shows excellent agreement between the experimental and calculated results for the truncated tetrahedral shape. These results are similar to what we obtained in previous work involving the long range dependence of the LSPR λ_{max} shifts using 11-MUD/ Cu^{2+} multilayers, but here the index of refraction of the Al_2O_3 is known accurately; whereas, with the SAM multilayers it could only be estimated.[14] The only significant differences between theory and experiment in Fig. 3.8 are (1) that the theory shift is higher than experiment for layer thicknesses of 10-30 nm, and (2) a small bump in the calculated result at 50 nm. The 10-30 nm result could easily arise from small differences between theory and experiment in the precise definition of the layer structure. The bump is likely a photonic resonance effect that would be extremely sensitive to layer structure and thus unlikely to show up in the same way in the experiment.

The hemispheroidal nanoparticle was modeled using the same parameters as the triangular nanoparticle. Initially, the hemispheroidal nanoparticle was modeled as half an

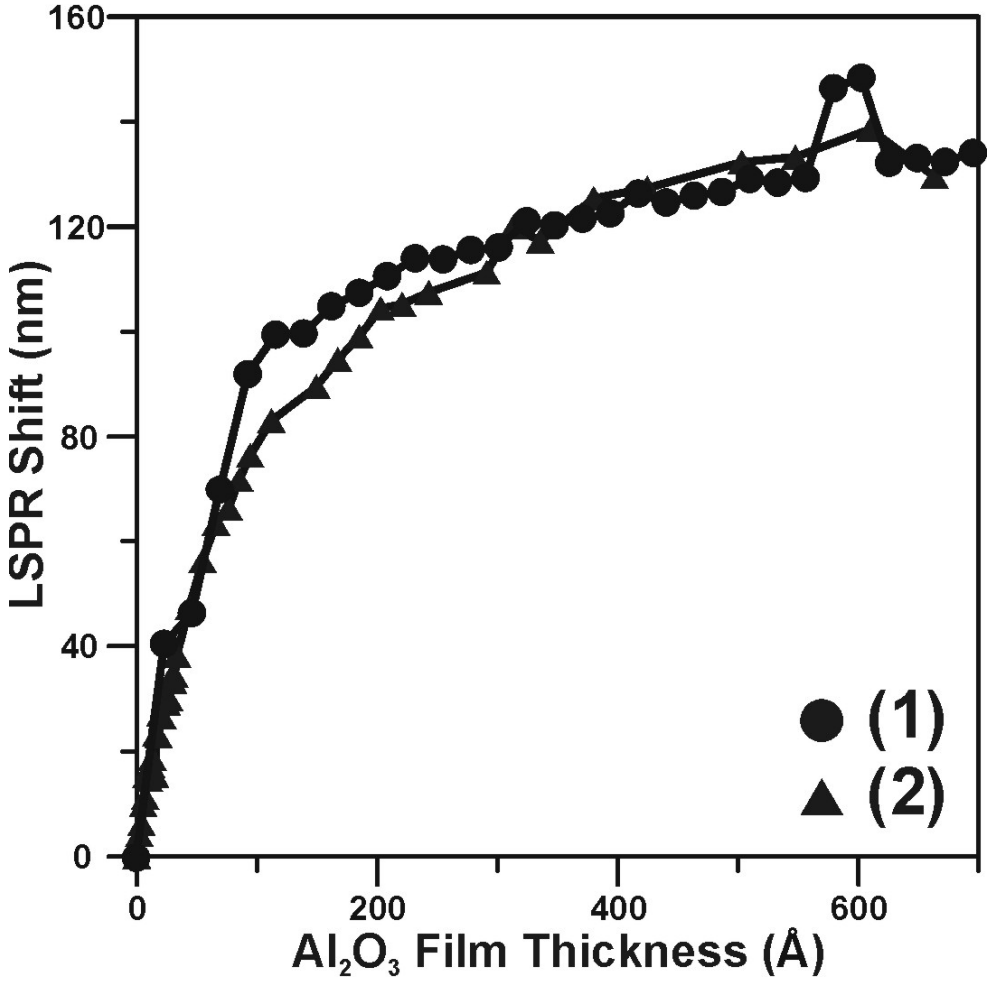

Figure 3.8 Comparison of calculated (1) and experimental (2) shift of the LSPR from bare truncated tetrahedral particles with a = 90 nm and b = 40 nm

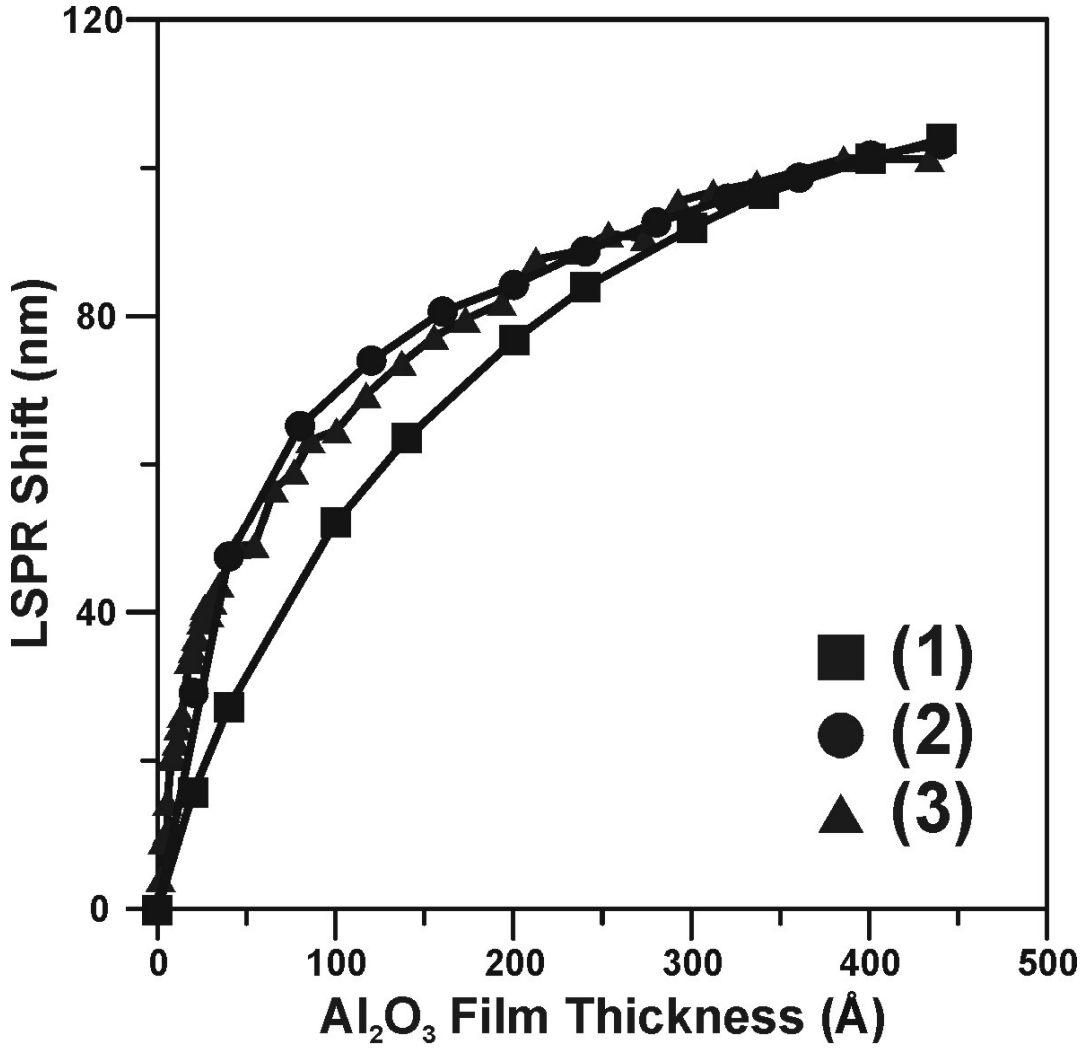

Figure 3.9 Experimental (●) vs. Calculated shift (■) of the LSPR from bare hemispheroidal particles with a = 102 and b = 54 nm along with experimental results (▲). A second calculation (■) was conducted with a small ring added to the hemispheroid as described above.

ellipsoid with dimensions: diameter = 104 nm and height = 52 nm. The nanoparticle was then coated with layers of Al_2O_3. The calculated results as well as the LSPR λ_{max} shifts from the experiment are presented in Figure 3.9. This shows, as noted earlier, that the measured LSPR λ_{max} red shifts sharply with increasing Al_2O_3 film thickness for layer thicknesses less than 10 nm and then bends over as the thickness is increased. However, the calculations show that the LSPR λ_{max} red shifts almost linearly with increasing Al_2O_3 layer thickness, with a slope that is significantly smaller than is observed. Thus it seems that even though the particle was modeled using the exact shape parameters from the experiment, the model does not describe the observed sensitivity to layer thickness. Further, the difference between theory and experiment is consistent with the presence of a short range near-field around the hemispheroidal particle, such as would arise from small radius of curvature features such as the sharp points that are present in the truncated tetrahedral structure. From this we infer that the idealized hemispheroidal shape does not characterize the annealed particle completely, and there must be additional sharp features, not resolvable with AFM, that produce the short range near-field behavior that is seen in the experiments. To model this, we have assumed that at the bottom edge of each spheroid, there is an "apron" of metal that arises from wetting the substrate during the annealing stage. Thus the hemispheroidal nanoparticle is assumed surrounded by a ring of metal that is 8 nm in width and 4 nm in height whose bottom surface is parallel to the bottom surface of the hemispheroid. The results of DDA calculations with this structure (Figure 3.9) agree well with the experimental LSPR λ_{max} shifts. From this we see how a small, sharp feature on the nanoparticle can have a large influence on the near-field, and hence on the short-range dependence on layer thickness. This influence becomes less important when the layer thickness is increased, especially when the layer thickness is larger than 30 nm. Unfortunately, we do not have the resolution in our AFM

measurements to see a feature as small as is suggested by the theory. Also, instead of an apron, a crack of similar dimensions but underneath the bottom of the particle should have a similar affect.

3.4 Conclusions

This work demonstrates that the LSPR nanosensor can detect a single layer of Al_2O_3 deposited by ALD. Furthermore, the long range results presented in this paper provide a 10x increase in the spatial resolution compared with previous experiments. At short distances from the Ag nanoparticle surface there is a much larger LSPR λ_{max} red shift than is seen at distances further from the nanoparticle surface. Furthermore, nanoparticles with fixed in-plane widths and decreasing out-of-plane heights have larger sensing distances which, is the same trend that was observed for alkanethiol layers at larger distances from the nanoparticle surface. Surprisingly, it was found that hemispheroidal nanoparticles show sensitivity to adsorbed layers that is comparable to that for the triangular nanoparticles. This work has also explored the nucleation and growth mechanism of Al_2O_3 by ALD on Ag surfaces. Both XPS and QCM results suggest that initially, TMA decomposes completely on the Ag surface.

Chapter 4

Thermally Stable Nanosphere Lithography Fabricated Nanoparticles for Applications in Operando Surface-Enhanced Raman Spectroscopy

4.1 Introduction

Homogeneous catalysis plays a large role in the chemical industry since many products are fabricated by this process. The ability to monitor the surface chemistry during a catalytic reaction is imperative towards improving current and developing new catalytic processes. *In situ* spectroscopic techniques have provided important fundamental information in regards to surface species and catalyst structure.[70-72] Unfortunately, these experiments are often conducted under a controlled environment that does not mimic industrial conditions. As a result, the data that is collected may not be comparable to the catalytic process in question. Operando spectroscopy is a method where spectroscopic data can be collected *in situ* under temperatures and pressures employed in industrial catalytic reactions.[72,73] Therefore, the information found in operando spectroscopy experiments can provide valuable insight towards understanding industrial catalytic processes.

Nanosphere Lithography (NSL) fabricated nanoparticles have been successfully utilized as surface-enhanced Raman spectroscopy (SERS) substrates.[19,74,75] The signature optical property of these nanoparticles is the localized surface plasmon resonance (LSPR). The LSPR phenomenon occurs when light interacts with particles that are much smaller (~10 – 200 nm) than the incident wavelength.[1,6] The resulting effect is that the electric field **E** near the particle surface is enhanced where $| \mathbf{E} |^2$ can be 100 - 10,000 times larger than the incident field.[1] This enhancement of the electromagnetic field makes these materials excellent SERS substrates.[19,74,75] It is well known that the SERS effect significantly enhances the Raman scattering signal when the Raman-active molecule is spatially confined within the electromagnetic fields generated upon excitation of the LSPR of the nanostructured noble metal surface.[8] The SERS signals of ensemble-averaged molecules demonstrate enhancements up to 8 orders of magnitude over

normal Raman signals.[19,20] Because, NSL fabricated nanoparticles are excellent SERS substrates, they have the potential to be used to conduct *in situ* studies of model catalytic reactions. Because SERS is an extremely sensitive technique, operando SERS would allow for the study of catalytic surfaces that are normally difficult or impossible to characterize with normal Raman spectroscopy. Unfortunately, at elevated temperatures (300ºC),[9] these nanoparticles anneal and form hemispheres, which have been found to have significantly less extinction efficiency than tetrahedrons.[1] Therefore, any reaction that requires high temperatures, such as many catalytic processes, could not be studied with these nanoparticle substrates. Alternatively, if the nanoparticles could be designed to be thermally robust as well as maintain their optical properties they would have great potential to be used for operando SERS studies.

The work presented herein demonstrates the initial steps towards designing a thermally robust SERS sensor for conducting operando SERS experiments. Atomic layer deposition (ALD) has been utilized to fabricate thermally robust SERS substrates that also have the potential to be a support for model catalytic reactions such as the oxidative dehydrogenation of cyclohexane. ALD is a fabrication method that produces highly uniform and controlled thin films. Precursor gases are alternately pulsed through the reactor and purged away resulting in a self-limiting growth process that constructs a film one monolayer at a time.[56] Highly uniform monolayers of Al_2O_3 can be deposited with ~1 Å thickness resolution.[15] Furthermore, because Al_2O_3 is often used as a catalytic support, these substrates could be used to monitor a variety of catalytic reactions.

LSPR spectroscopy and scanning electron microscopy (SEM) were used to compare the stability of bare Ag nanoparticles and Ag nanoparticles coated with 0.2 nm, 0.4 nm, and 1.0 nm of ALD Al_2O_3 at various temperatures (50 ºC, 100 ºC, 200 ºC, 300 ºC, 400 ºC, and 500 ºC) and

over time (up to 6 hours) in N_2. It was necessary to use thin coatings (1.0 nm or less) so that the SERS enhancement, which decays exponentially from the nanoparticle surface, would be maintained.[74] The results of this work found that even after coating the Ag nanoparticles with 0.2 nm of ALD Al_2O_3, the Ag nanoparticle arrays exhibit a substantially increased thermal stability, in comparison with bare Ag nanoparticles, at temperatures of at least 500 °C for several hours. Because, these nanoparticles would ideally be used to conduct operando SERS experiments, they will be exposed to reactive compounds at elevated temperatures. Therefore, experiments were carried out with ALD Al_2O_3 coated Ag nanoparticles heated at various temperatures under propane to determine their stability under more realistic reaction conditions. At low temperatures (less than 200 ºC) the ALD Al_2O_3 coated nanoparticles' geometry is extremely stable. Alternatively, at higher temperatures (200 °C and above), the results showed that the nanoparticle structure is affected more so than the ALD Al_2O_3 coated nanoparticles that were heated under the less reactive gas, N_2. Therefore, it is believed that the atmospheric conditions have a significant effect on nanoparticle stability at elevated temperature. Overall, the ALD Al_2O_3 coated nanoparticles' geometry was significantly more thermally stable than bare Ag nanoparticles and therefore, they show great potential to be used for operando SERS experiments.

4.2 Experimental Methods

4.2.1 Materials

Ag (99.99%) was purchased from D. F. Goldsmith (Evanston, IL). Borosilicate glass substrates, No. 2 Fisherbrand 18-mm circular coverslips were acquired from Fisher Scientific (Pittsburg, PA) and P-doped Si (111) was obtained from Wacker Siltronic (Portland, OR). Hexanes, methanol, H_2SO_4, H_2O_2, and NH_4OH were purchased from Fischer Scientific

(Fairlawn, VA). Surfactant-free carboxyl-terminated polystyrene nanospheres with 390 nm (± 19.5 nm) diameters were received in a suspension of water from Duke Scientific (Palo Alto, Ca). Absolute ethanol was acquired from Pharmco (Brookfield, CT). Millipore cartridges (Marlbourough, MA) were used to purify water to resistively of 18 $M\Omega cm^{-1}$. Al_2O_3 films were fabricated by ALD utilizing trimethylaluminum (TMA) purchased from Sigma Aldrich (Milwaukee, WI) and deionized water.

4.2.2 Nanosphere Lithography

NSL was used to fabricate monodispersed, surface-confined Ag nanoparticles.[57] Glass and Si (111) substrates were cleaned in a piranha etch solution (3:1 H_2SO_4/H_2O_2 30%) for 30 min at 80 ºC. After rinsing with water, the substrates were sonicated for 60 min in 5:1:1 $H_2O/H_2O_2/NH_4OH$ in order to create a hydrophilic surface on the substrate to facilitate self-assembly of the nanosphere masks. Finally, the substrates were rinsed and stored in water for future use. 2D self-assembled monolayer masks of nanospheres were fabricated by drop-coating approximately 2.5 μL of undiluted nanosphere solution (10% solid) on the pretreated substrates. The nanospheres were allowed to dry in ambient conditions. 50 nm of Ag was deposited by electron beam (e-beam) deposition in a Kurt J. Lesker Axxis e-beam deposition system (Pittsburg, PA) with a base pressure of 10^{-6} Torr. The mass thickness and deposition rate (1 Å/sec) was monitored using a Sigma Instruments 6 MHz gold plated QCM (Fort Collins, Colorado). After the Ag deposition, the nanosphere masks were removed by sonication in absolute ethanol for 3 min.

4.2.3 Atomic Layer Deposition

Al_2O_3 films were fabricated on the Ag nanoparticles by ALD. The reactor utilized in these experiments is similar to previous publications.[58] TMA and deionized H_2O vapors were

alternately pulsed through the reaction chamber utilizing N_2 as the carrier gas at a mass flow rate of 360 sccm and a pressure of 1 Torr using a growth temperature of 50 ºC. Al_2O_3 ALD proceeds on a hydroxylated surface according to scheme 1.[16]

Scheme 1.

(C) $Al\text{-}OH^* + Al(CH_3)_3 \rightarrow Al\text{-}O\text{-}Al(CH_3)_2^* + CH_4$

(D) $Al\text{-}CH_3^* + H_2O \rightarrow Al\text{-}OH^* + CH_4$

The asterisks (*) signify the surface species. One complete AB cycle is 42 s: (1) TMA reactant exposure time = 1 s, (2) N_2 purge following TMA exposure time = 10 s, (3) H_2O reactant exposure time = 1 s, (4) N_2 purge following H_2O exposure time = 30 s. Long purge times are necessary at low temperatures to prevent chemical vapor deposition (CVD) of Al_2O_3.[16]

4.2.4 Thermal Annealing

Thermal studies were conducted inside the ALD reaction chamber under one Torr of N_2 or 10 Torr of propane.

4.2.3 UV-Vis Extinction Spectroscopy

LSPR extinction measurements of the Ag nanoparticle arrays were obtained using a variable angle spectroscopic ellipsometer (VASE) M-2000V from J. A. Wollam Co. in transmission mode.

4.2.4 Scanning Electron Microscopy (SEM)

SEM images of bare and ALD Al_2O_3 coated NSL nanoparticles on Si (111) were observed with a Hitatchi S-4700-II SEM. Images were collected with 10.0 kV.

4.3 Results and Discussion

4.3.1 Thermal Stability of ALD coated NSL Particles at Various Temperatures

The LSPR λ_{max} of metal nanoparticles is extremely sensitive to nanoparticle shape and size.[8,76] Therefore, geometry changes of the nanoparticle structure due to thermal annealing can be determined by monitoring their LSPR value. A blue shift of the LSPR will be observed if the Ag triangular nanoparticle changes shape as a result of annealing.[8,76] Previous work ha shown that bare Ag triangular nanoparticles that have been annealed for at 300 °C for 1 hour form hemispheres with an LSPR ~450 nm.[9] Figure 1 examines the shift of the LSPR of both bare Ag nanoparticles and Ag nanoparticles coated with 0.2 nm, 0.4 nm, and 1.0 nm of ALD Al_2O_3 before and after heating for one hour at several temperatures (100 ºC, 200 ºC, 300 ºC, 400 ºC, and 500 ºC). After heating the bare Ag nanoparticles for one hour at 100 °C a 62 nm blue shift in the LSPR occurs, indicating that a structure change due to temperature had already occurred (Fig 4.1A). Upon annealing the bare Ag nanoparticles at 200 °C for one hour an overall shift of 206 nm was observed, indicating that the nanoparticles have become hemispherical. Alternatively, only a 9 nm blue shift of the LSPR is observed after heating Ag triangular nanoparticles coated with 1.0 nm of ALD Al_2O_3 at 500 °C for 1 hour, indicating that the nanoparticles retained their original triangular shape. A plot of LSPR shift vs. temperature can be seen for bare Ag nanoparticles (Fig. 4.1C) as well as Ag nanoparticles coated with 0.2 nm (▲), 0.4 nm (■), and 1.0 nm (♦) of ALD Al_2O_3 (Fig. 4.1D). While the bare Ag nanoparticles already show a large negative LSPR shift (62 nm) after exposure to 100 °C, the LSPR of the nanoparticles coated with as little as 0.2 nm the ALD Al_2O_3 show significantly less negative shifting (21 nm) even after heating for 1 hour at 500 ºC. Ag nanoparticles with the thickest (1.0 nm) ALD Al_2O_3 coatings

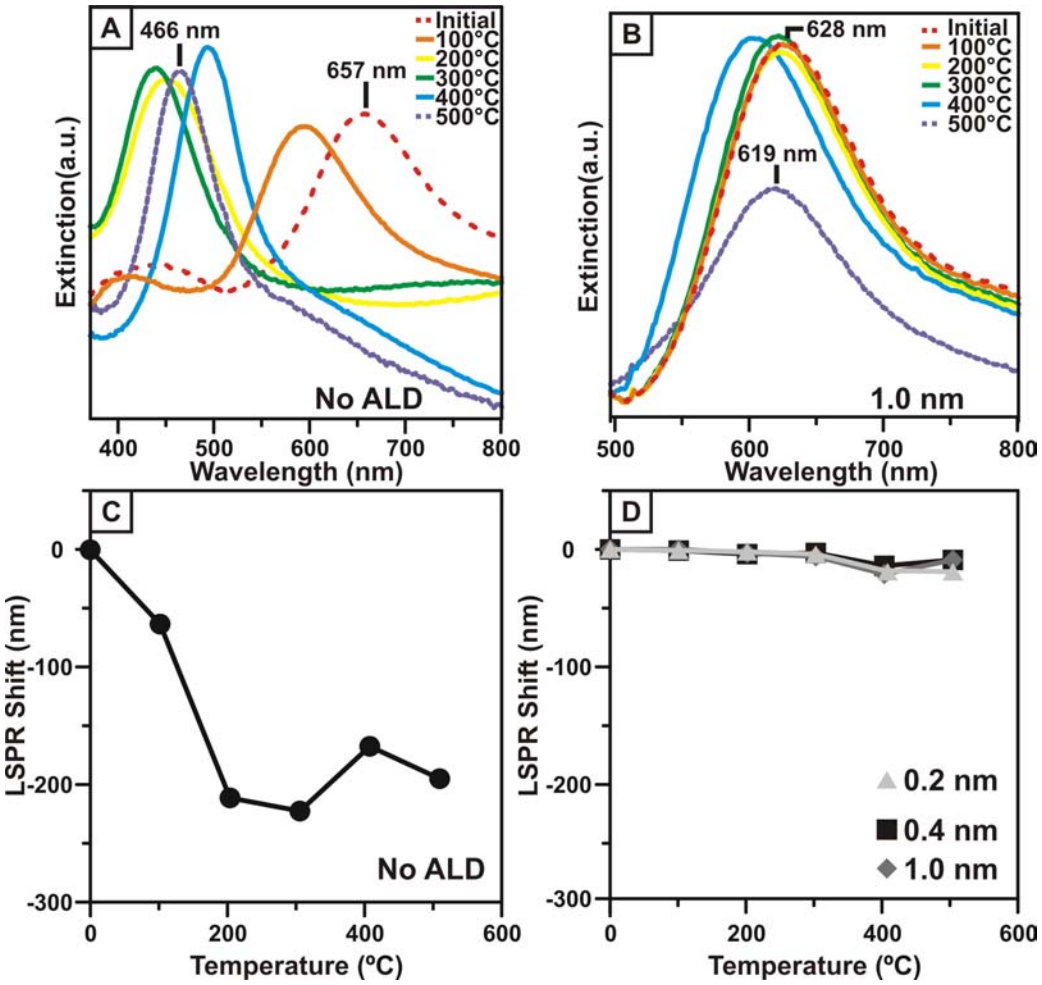

Figure 4.1 LSPR spectroscopy of bare Ag nanoparticles (A) and Ag nanoparticles coated with 1.0 nm of ALD Al_2O_3 (B) heated at various temperatures. (C) Plot of the LSPR shift vs. temperature of bare Ag nanoparticles heated at various temperatures. (D) Plot of the LSPR shift Ag nanoparticles coated with 0.2 nm (▲), 0.4 nm (■), and 1.0 nm (♦) ALD Al_2O_3 heated at various temperatures. All samples were heated at each temperature for 1 hour under 1 Torr of N_2.

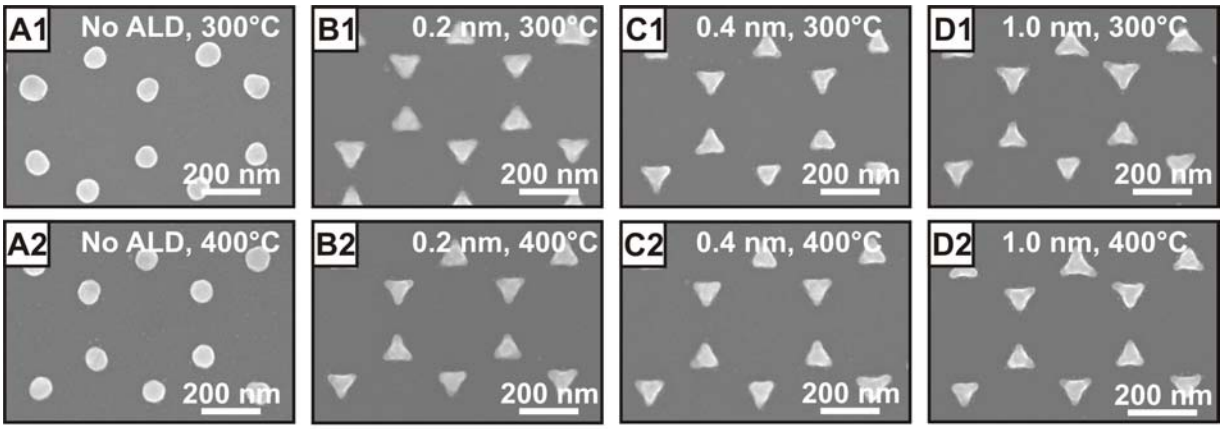

Figure 4.2 SEM images of bare Ag nanoparticles (A1,A2) and Ag nanoparticles coated with 0.2 nm (B1, B2), 0.4 nm(C1, C2), and 1.0 nm (D1, D2) of ALD Al_2O_3 heated at 300 °C (A1, B1, C1, and D1) and 400 °C (A2, B2, C2, and D2). All samples were heated at each temperature for 1 hour under 1 Torr of N_2.

have the smallest LSPR shifts after heating, indicating that thicker coatings protect the nanoparticle better. Using SEM, the shape of the bare and ALD Al_2O_3 coated Ag nanoparticles can be visually observed after thermal treatment. Figure 2 depicts SEM images of bare Ag nanoparticles (2A-1 and 2A-2) and Ag nanoparticles coated with 0.2 nm (4.2B-1 and 4.2B-2), 0.4 nm (4.2C-1 and 4.2C-2), and 1.0 nm (4.2D-1 and 4.2D-2) of ALD Al_2O_3 after heating for one hour at 300 °C and 400 °C. The bare Ag nanoparticles formed hemispheres after thermal annealing at 300 ºC and 400 ºC (Fig.4.2A-1 and 4.2A-2), which correlates well with the observed LSPR values measured after annealing at these temperatures. The SEM images show that while the ALD Al_2O_3 coated nanoparticles retain their triangular shape, the heating does slightly affect their shape. An average decrease of the perpendicular bisector of ~5 nm is seen after heating the ALD Al_2O_3 coated nanoparticles at 300ºC for 1 hr. An additional reduction of ~9 nm is seen after annealing at 400ºC for 1 hour. Overall, the geometry change is small and therefore these nanoparticles appear to be suitable to be used in elevated temperatures with little structural change. While the LSPR spectra indicated that thicker ALD Al_2O_3 coatings maintained the nanoparticle geometry the best, very little difference in nanoparticle geometry was observed in the SEM images.

4.3.2 Thermal stability of ALD coated NSL particles at 500°C over time

The thermal stability over time was examined for bare and ALD Al_2O_3 coated Ag nanoparticles. Figure 4.3 depicts LSPR spectra of bare Ag nanoparticles (Fig. 4.3A) and Ag nanoparticles coated with 1.0 nm ALD Al_2O_3 (Fig. 4.3B) taken at one hour intervals over 6 hours while heating at 500 °C under N_2. The LSPR shift vs. time for both the bare Ag nanoparticles (Fig. 4.3C) and Ag nanoparticles coated with 0.2 nm (▲), 0.4 nm (■), and 1.0 nm (♦) ALD Al_2O_3 (Fig. 4.3D) was plotted. As expected, the bare Ag nanoparticles experienced an LRPR

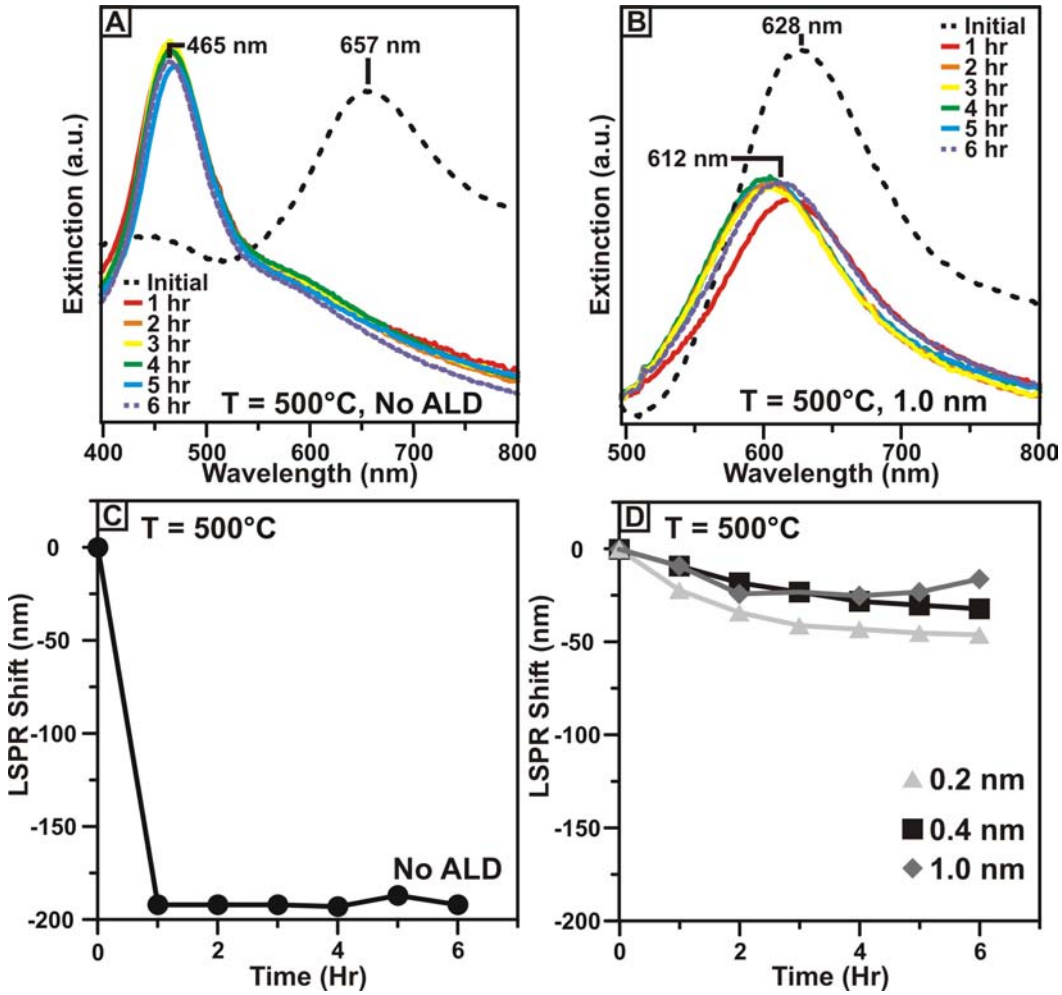

Figure 4.3 LSPR spectroscopy of bare Ag nanoparticles (A) and Ag nanoparticles coated with 1.0 nm of ALD Al_2O_3 (B) heated at 500 °C over time. (C) Plot of the LSPR shift of bare Ag nanoparticles heated at 500 °C over time. (D) Plot of the LSPR shift of Ag nanoparticles coated with 0.2 nm (▲), 0.4 nm (■), and 1.0 nm (♦) of ALD Al_2O_3 heated at 500 °C over time. All samples were heated under 1 Torr of N_2.

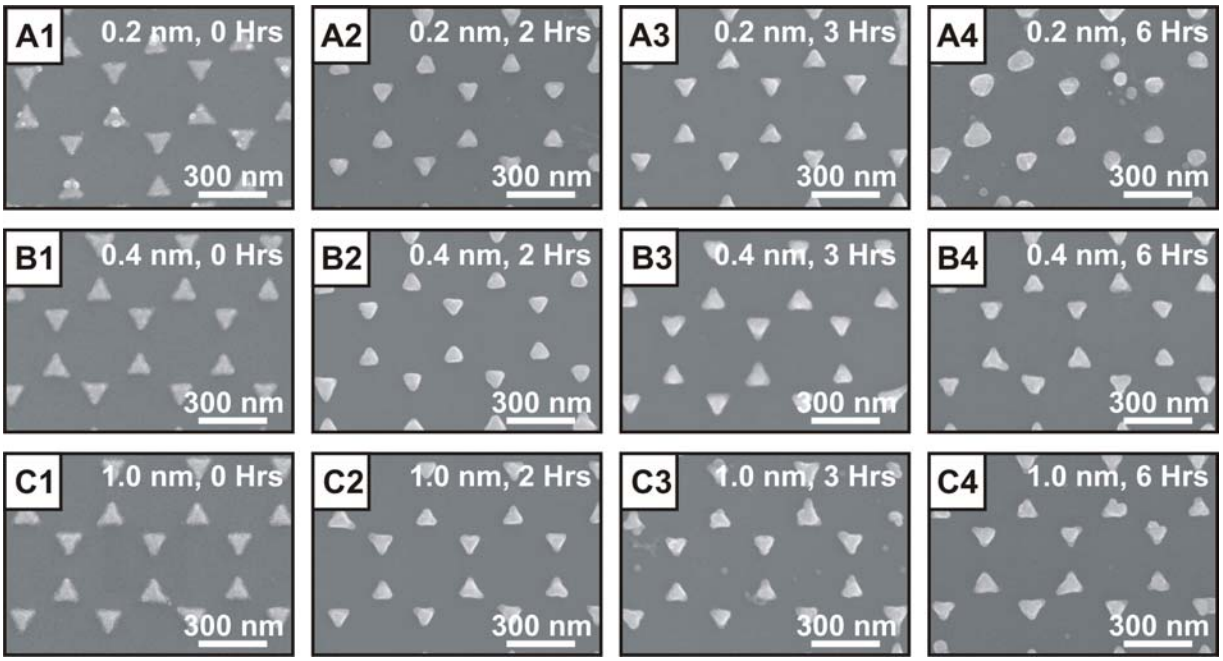

Figure4.4 SEM images of Ag nanoparticles coated with 0.2 nm (A1-A4), 0.4 nm (B1-B4), 1.0 nm (C1-C4) of ALD Al_2O_3 heated at 500 °C for 0, 2, 3, and 6 hours. All samples were heated under 1 Torr of N_2.

shift from 657 nm to 465 nm in just one hour indicating that the triangular nanoparticles had become hemispheres. The LSPR remained constant for the subsequent hours, which correlates with the idea that a hemisphere should be the most geometrically stable structure for these nanoparticles. Alternatively, the nanoparticles coated with 1.0 nm ALD Al_2O_3 changed shape very little as is verified by an overall LSPR blue shift of just 16 nm after six hours. While the nanoparticles coated with 0.2 nm (Fig. 4.3D) had a larger over all shift of 24 nm, this value still confirms that the triangular shape was well maintained even after heating at 500 °C for six hours. Overall, it was observed that the thickest ALD Al_2O_3 coating (1.0 nm) resulted in the most stable nanoparticle structure.

SEM images were taken of Ag nanoparticles coated with 0.2 nm, 0.4 nm, and 1.0 nm of ALD Al_2O_3 heated at 500 °C after 0, 2, 3, and 6 hours (Figure 4.4). After two hours, an average reduction of ~14 nm of the nanoparticles' perpendicular bisectors was seen. After six hours, a significant difference in nanoparticle shape and monodispersity was observed. The geometry of the Ag nanoparticles coated with 0.2 nm ALD Al_2O_3 had significantly changed (Fig 4.4-A4) but was still significantly more retained than the geometry of bare Ag nanoparticles after thermal annealing. A further average reduction of ~3 nm was found for the Ag nanoparticles coated with 0.4 nm and 1.0 nm ALD Al_2O_3.

4.3.3 Thermal Stability of ALD Coated NSL Particles Under Propane

The experiments described previously show that ALD Al_2O_3 coated Ag nanoparticles are thermally stable under minimally reactive compounds such as N_2 In order for these Ag nanoparticles to be successful as operando SERS substrates, they need to be stable under both the reactants and products that would be present in a catalytic reaction. Propane, which is much more reactive than N_2, is often used in catalytic reactions; therefore Ag nanoparticles coated with

1.0 nm ALD Al_2O_3 were heated at various temperatures for 30 minutes under 10 Torr of propane. Figure 4.5 shows LSPR spectra collected before and after heating at 50 ºC (A), 100 ºC (B), 200 ºC (C), 300 ºC (D), and 400 ºC (E). A 1 nm and 9 nm blue shift is seen for the nanoparticles heated at 50 ºC at 100 ºC, respectively, implying that very little structural change occurred. Surprisingly, a larger blue shift of 36 nm was observed for the nanoparticles heated at 200ºC, indicating a larger change in nanoparticle geometry in comparison to ALD Al_2O_3 coated nanoparticles that were heated under N_2. Finally a blue shift of 61 nm and 58 nm was observed for nanoparticles that were annealed under 300 ºC and 400 ºC respectively. These results signify that as the temperature is increased, larger structural changes occur. Furthermore, these experiments show that reactive compounds such as propane modify the nanoparticle structure at elevated temperatures more than less reactive compounds such as N_2.

SEM images of the ALD Al_2O_3 coated nanoparticles after heating under propane are shown in Figure 4.5F-J. Nanoparticle perpendicular bisector decreased an average of 0.6 nm for the nanoparticles heated at 50 ºC, showing that minimal structural change occurs when exposing the nanoparticles to propane at low temperatures. This result correlates well with the fact that only a 1 nm blue shift of the LSPR occurred after annealing. Additionally, little structural change (3.4 nm reduction of the perpendicular bisector) was seen for the nanoparticles heated at 100 ºC. Alternatively, an average reduction in the perpendicular bisector of 6.9 nm, 9.6 nm, and 9.6 nm was seen for the nanoparticles heated at 200 ºC, 300 ºC, and 400 ºC respectively. The SEM images support the results found in the LSPR spectra, which indicate that larger geometry changes occur at higher temperatures.

While there are large structural changes in nanoparticle geometry when heating at high temperatures under propane, the changes are still much less significant than those observed for

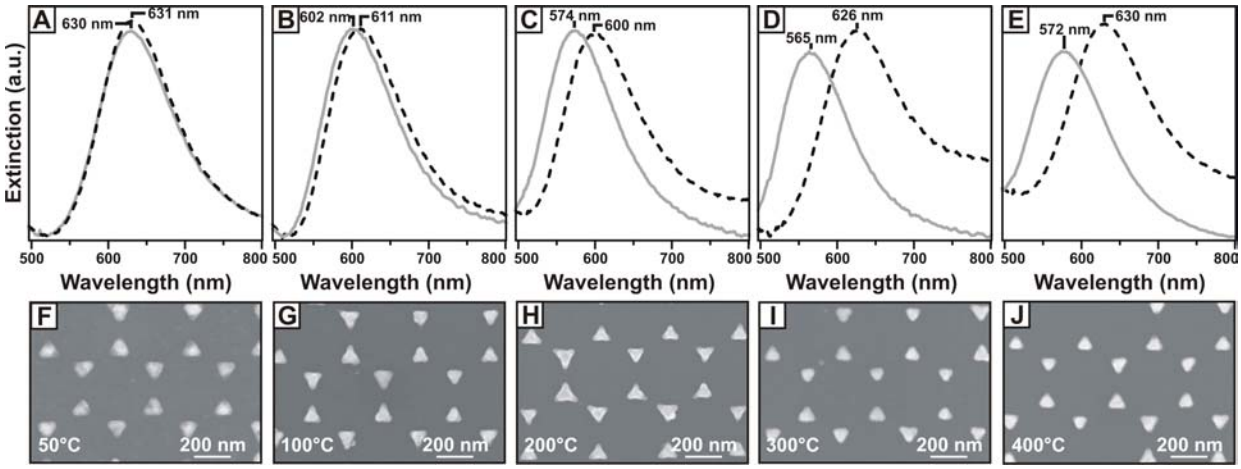

Figure 4.5 LSPR spectra of Ag nanoparticles coated with 1.0 nm of ALD Al_2O_3 heated for 30 minutes at 50 °C (A), 100 °C (B), 200 °C (C), 300 °C (D), and 400 ºC (E) under 10 Torr of propane. The initial LSPR λ_{max} is depicted by a black dashed line and the LSPR λ_{max} after thermal annealing under is depicted by a solid grey line. Each plot is paired with a corresponding SEM image taken after heating at 50 °C (F), 100 °C (G), 200 °C (H), 300 °C (I), and 400 ºC (J).

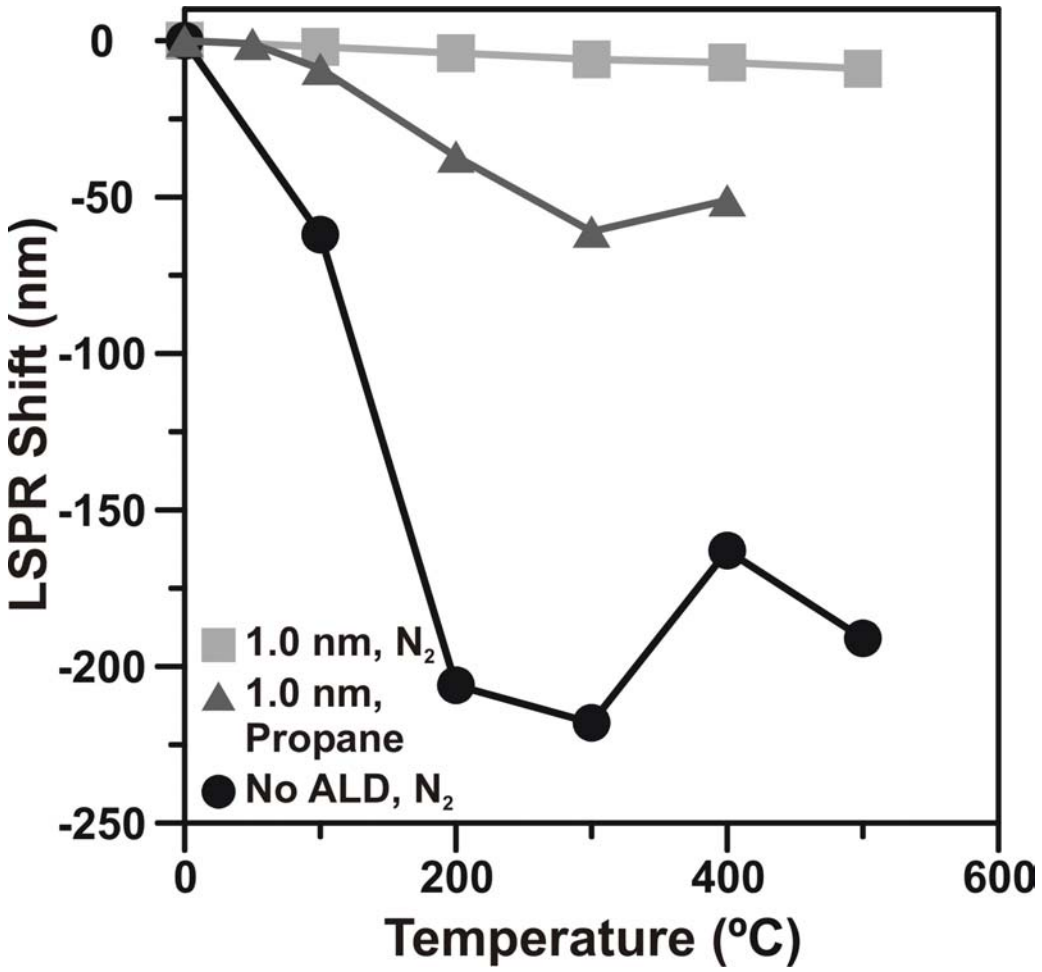

Figure 4.6 Plot of LSPR shift vs. temperature for Ag nanoparticles coated with 1.0 nm ALD Al_2O_3 heated under 1 Torr N_2 (■) or 10 Torr propane (▲), and bare nanoparticles heated under 1 Torr N_2 (●).

bare nanoparticles. Figure 4.6 depicts a plot of LSPR shift vs. temperature for Ag nanoparticles coated with 1.0 nm ALD Al_2O_3 heated under N_2 (■) and propane (▲) as well as bare Ag nanoparticles heated under N_2 (●). The plot shows that the ALD Al_2O_3 coated nanoparticles heated under N_2 maintained their shape the most. ALD Al_2O_3 coated nanoparticles maintained their geometry at low temperatures under propane. Although, the nanoparticles did not perform at temperatures as well as they did under N_2, they still maintained their structure well in comparison to bare Ag nanoparticles. These results indicate that the thermally stable ALD Al_2O_3 coated nanoparticles show potential to serve as effective operando SERS substrates.

4.4 Conclusions

This work has shown that ALD Al_2O_3 coated Ag NSL fabricated nanoparticles can maintain their shape at high temperatures over time and therefore have the potential to be used as operando SERS substrates. Experiments were carried out to determine both the stability of bare Ag nanoparticles and Ag nanoparticles coated with various thicknesses (0.2 nm, 0.4 nm, and 1.0 nm) of ALD Al_2O_3 at several temperatures (100 °C, 200 °C, 300 °C, 400 °C, and 500 °C) and over long periods of time (up to 6 hours). The results showed that ALD Al_2O_3 coated nanoparticles maintained their original geometry significantly better that the bare Ag nanoparticles. While experiments showed that thicker ALD Al_2O_3 coatings resulted in the most stable nanoparticle structure, ALD Al_2O_3 coatings as thin as 0.2 nm resulted in thermally robust nanostructures as well. LSPR spectra indicated that all the ALD Al_2O_3 coated nanoparticles maintained their shape well at temperatures of at least 500 ºC. Nanoparticles with the thickest ALD Al_2O_3 coating (1.0 nm) showed the least structural change. While, the nanoparticles coated with the most ALD Al_2O_3 (1.0 nm) maintained their geometry better at 500ºC for longer periods

of time, the nanoparticles with thinner coatings of ALD Al_2O_3 still preformed at a level where they could be used as successful SERS substrates at elevated temperatures over several hours. Finally, ALD Al_2O_3 coated Ag nanoparticles were heated at various temperatures under propane to mimic more realistic reaction conditions. These experiments showed that while the nanoparticle geometry was not as stable as under N_2, they were much more stable than uncoated nanoparticles. This work provides the first steps towards developing SERS substrates that can be used to perform Operando SERS studies.

Chapter 5

An Innovative Surface-Enhanced Raman Spectroscopy (SERS) Method for the Identification of Six Historical Red Lakes and Dyestuffs

5.1 Introduction

Since the 1980s, Raman microspectroscopy has grown to be a well-established technique for the characterization of artists' pigments[77-81]. However, many dyestuffs, such as traditional red lake pigments and organic dyes of natural origin, are extremely fluorescent, an effect that dominates the weak optical process of Raman scattering. Furthermore, because subnanogram levels of these dyes are needed to achieve intense coloration, normal Raman spectroscopy is often not sensitive enough to probe these materials. Red lakes were extremely prized for their transparent, yet intense colors and are often found in paintings and illuminated manuscripts as thin glaze layers, usually characterized by a high proportion of oil medium. Lake pigments are obtained by precipitation of deeply colored dyestuffs onto inert, finely divided particles of alumina trihydrate or, alternatively, calcium carbonate or gypsum. The dyestuffs themselves, have been used for dyeing textiles since the earliest times of human history, bound to the fibers through formation of a metal complex with metal salts (called mordants, most commonly alum – $Al_2(SO_4)\cdot K_2SO_4\cdot 24H_2O$; iron sulfate – $FeSO_4\cdot 7H_2O$ - and tin chloride -$SnCl_2$ -). Previously, normal Raman spectroscopy has been successfully employed to characterize the historical red lake madder, which contains both the anthraquinone alizarin and purpurin.[82] FT-Raman spectroscopy has also been a successful technique to study madder as well as brazilwood.[79,83,84] However, no other red dyestuff has been successfully characterized due to the combined effect of high fluorescence and relatively small Raman scattering cross section of these compounds.

The Raman cross section can be amplified by Surface-enhanced Raman scattering (SERS). Furthermore, the use of a noble metal SERS substrate can quench fluorescence. SERS is a process whereby the Raman scattering signal is increased when a Raman-active molecule is spatially confined within the electromagnetic fields generated upon excitation of the localized

surface plasmon resonance of the nanostructured noble metal surfaces. The SERS signals of ensemble-averaged molecules demonstrate enhancements up to 8 orders of magnitude over normal Raman signal.[19,20] A variety of SERS substrates have been successfully employed to detect and study analytes including: (1) Citrate reduced Ag colloids,[85-87] (2) porous Ag electrodes,[88] (3) Ag films over nanospheres (AgFON),[23,89] (4) nanosphere lithography (NSL) derived Ag nanoparticles,[19] and (5) Ag island films (AgIF).[90]

Guieneau and Guichard first explored SERS as a technique to study the fluorescing anthraquinone dyes in 1987.[88] The authors demonstrated significant S/N enhancement obtained by performing SERS measurements on a porous Ag electrode cooled with liquid nitrogen on synthetic alizarin and extracts from a XIII century textile sample died with madder.[88] However, nearly twenty years passed before a significant body of study was published on SERS analysis of dyes, with the majority of the studies presented to date still focused on alizarin and purpurin[85,86].

Citrate reduced Ag colloids have been successfully employed as SERS substrates to detect alizarin and purpurin[85-87]; however, significant spectral changes have been described for alizarin and purpurin as function of pH.[86] Because SERS is extremely distance dependent, where the molecule in question must be confined within the decay length of the electromagnetic fields (0 – 4 nm)[91] one must have molecules that can replace the citrate surfactant and bind to the Ag surface which can prove challenging. Furthermore, the Ag colloids must be aggregated, which is difficult to reproduce and can have significant affects on the SERS spectra. An alternate SERS substrate is the AgIF, which is highly reproducible, and can be applied directly on single grains of pigment as is typically found in works of art.

The work presented herein describes the use of electron beam (e-beam) deposited AgIFs on samples and successively analyzing the SERS active surface with a confocal, dispersive,

Raman microscope. The work conducted allowed us to optimize several parameters of the analysis, including thickness of the AgIF, attenuation of laser power at the sample to limit thermal and photochemical damage, dimension of the total volume sampled (via reduction of the diameter of the confocal hole), and optimal laser excitation line (initially λ_0= 532 nm; 632.8 nm and 785.7 nm were evaluated), thus achieving significant improvement in S/N and resolution of peaks over normal Raman spectra.

SERS spectra of complex molecules such as anthraquinoid or flavonoid dyes will show different band positions and selective enhancement of particular peaks compared to normal Raman or FT-Raman. The band position shift may be due to the chemisorption of the molecule with the SERS surface. Because these dyes absorb visible light there may be a resonant effect, which will provide further peak enhancement and will result in Surface Enhanced Resonance Raman Scattering (SERRS). However, experimental work carried out by the authors and described elsewhere has demonstrated that the maximum enhancement of the Raman signal from these samples of red dyestuffs used as artists' materials occurs when the excitation wavelength matches the absorption band of the localized surface plasmon of the AgIF rather than the absorption of the dyestuff investigated.[29] Finally, the orientation of the molecule (perpendicular or parallel) with the SERS surface will result in selective enhancement of certain peaks. This renders interpretation of the spectra quite complex. Therefore, due to a lack of published reference SERS spectra of traditional artists' dyes and colorants we focused on red lake pigments and collected extremely detailed, reproducible spectra for 6 dyestuffs and selected lakes. In some cases, in order to support the interpretation of the spectra, single molecule theoretical computation of vibrational normal modes were performed, confirming good correlation between calculated and actual band position.

5.2 Natural and Early Synthetic Organic Colorants

The materials presented herein were chosen because they are the most commonly encountered red lakes and dyes in artistic production from antiquity to the 19th century.[92] All of these red natural organic compounds are complex structures that share a composition of condensed aromatic rings with hydroxyl, carbonyl and carboxylic acid functions and various other substituents, including sugars (cochineal) and amino groups (lac) (Fig. 5.1).

Madder is one of the oldest and most utilized dyestuff, with ample geographical distribution, spanning the East and west cultures since antiquity. In Europe it was extracted from the roots of the *Rubia Tinctorium L.* herb. When precipitating the dye on aluminum tri-hydrate one obtains a pigment of orange-red hue. Purpurin ($C_{14}H_8O_5$, 1,2,4- Trihydroxyanthraquinone, C.I. 58205) and alizarin ($C_{14}H_8O_4$, 1,2-Dihydroxyanthraquinone, C.I. 58000) are the main coloring substances of the madder root. Synthetic alizarin was introduced into the market in 1871 and soon after, the use of the natural root extract ceased. Amongst the coccid dyestuffs kermes, cochineal and lac dye were examined. When used as lake pigments each produce different shades of blue-toned, intense scarlet crimson color. Kermes has been used since antiquity, and one of the earliest mentions of this material can be found in the Old Testament. Kermes and cochineal are obtained by water or alcohol extraction of dried wingless female scale insects of two different species: *Kermes vermilio* Planch (kermes) and *Dactylopius coccus* L. Costa (cochineal) either cultivated or wild. Host plants for kermes are various types of oaks from Europe and Asia, while cochineal was collected from the Nopal cactus, in Mexico, Central and South America.[93] Both were very expensive commodities due to the laborious process of harvesting the insects. Imported to Europe since the 1540s, cochineal quickly supplanted kermes.

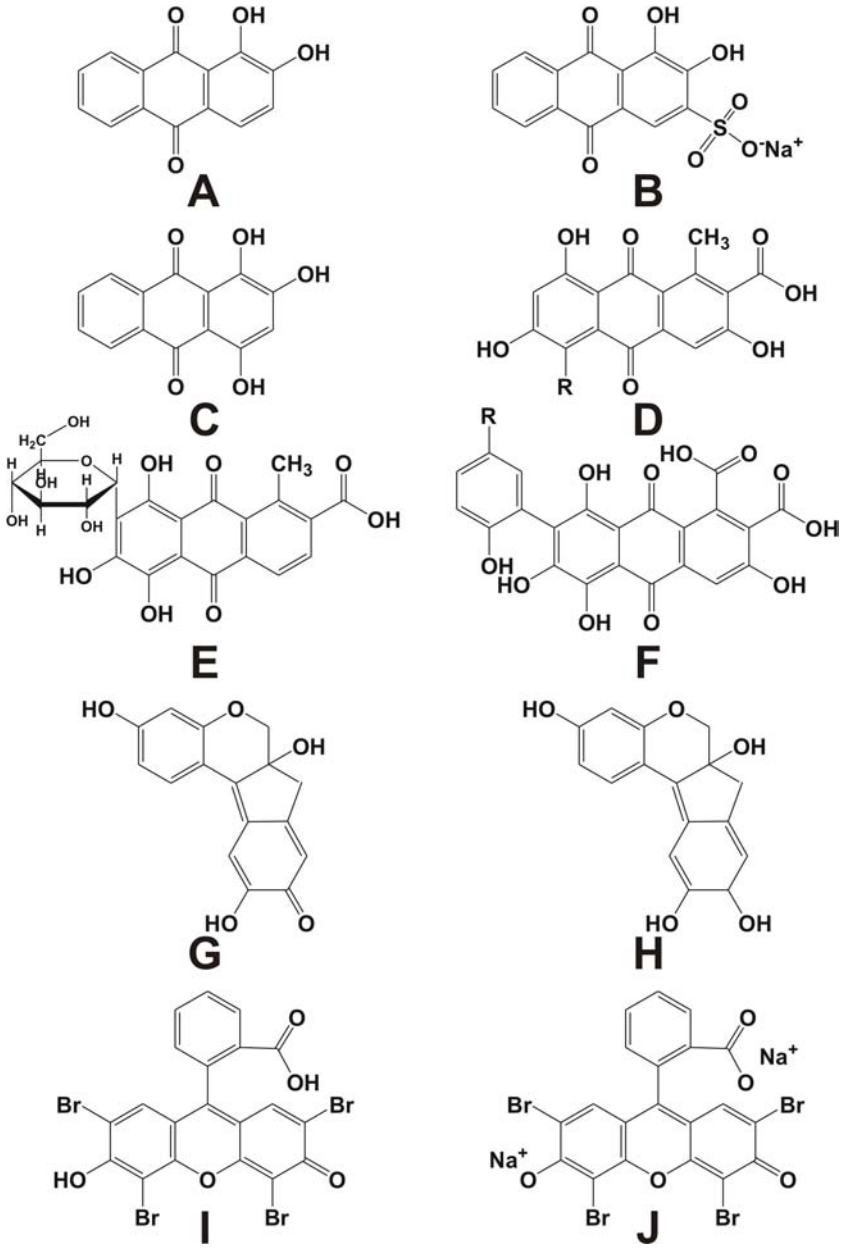

Figure 5.1 Natural and organic red organic compounds: (A) alizarin, (B) alizarin red S, (C) purpurin, (D) kermesic acid (R=OH); flavokermesic acid (R=H), (E) carminic acid**,** (F) 5 structures of laccaic acid are present in lac dye: laccaic acid A (R = $(CH_2)_2NHCOCH_3$), laccaic acid B (R = $(CH_2)_2OH$), laccaic acid C (R = $CH_2CH(NH_2)COOH$), laccaic acid D = flavokermesic acid, and laccaic acid E (R = CH_2NH_2). Laccaic acid A is the most prominent structure in lac dye, (G) brazilein, (H) brazilin, (I) eosin Y, (J) eosin Y free acid.

Cochineal is still commercially available today, however, due to its scarce light-fastness is no longer found in paintings, and is instead used in the cosmetic industry. The coloring matter of kermes and cochineal are kermesic acid ($C_{16}H_{10}O_8$, C.I. 75460) and carminic acid ($C_{22}H_{20}O_{13}$, C.I. 75470) respectively.

Laccifer lacca Kerr is another important scale insect, found on trees in India and Southeast Asia, from which lac dye is extracted. Used in India from ancient times to dye silk, it is not widely mentioned in European recipes for textile dyeing in the 15th and 16th century, but instead became more popular in the 19th century. The use of lac dye as an artists' pigment began in the 13th century and enjoyed widespread and extensive use in 15th Century Italy and onwards. Laccaic acids (C.I 75450) are the primary colorants in lac lake and are characterized by a hydroxyanthraquinone chemical structure associated to those of kermesic and carminic acid.

Brazilwood, a redwood from the tropical trees of the senna genus *Caesalpinia* native of Brazil, Nicaragua and Southeast Asia, was imported in Europe beginning in the 1500s. It was used to dye wool and silk and for manufacturing red inks. Although brazilwood was more economic than carmine it appears to have been applied less frequently in paintings probably because it has a less satisfactory hue and poor color permanence. The red color's principal component is brazilin ($C_{16}H_{14}O_5$, C.I. 75280), readily oxidized by light and air exposure to brazilein ($C_{16}H_{13}O_5$).

Eosin Y is an early synthetic dye that was utilized amongst 19th century artists. The potassium or sodium salt of 2,4,5,7 – tetrabromofluorescein was first made in 1871 and used for making inks. As a lake pigment, it makes a brilliant bluish red and was sold under the name of geranium lake. Van Gogh used the dye quite extensively but unfortunately, it has almost invariably faded in many of his paintings.

5.3 Experimental Methods

5.3.1 Raman Microspectroscopy

A Jobin Yvon Horiba Labram 300 confocal Raman microscope was used, equipped with Andor multichannel air-cooled open electrode charge-coupled device detector (CCD: 1024x256), BXFM open microscope frame (Olympus), holographic notch filter, and 1800 grooves/mm dispersive grating.

The excitation lines of an air cooled frequency doubled Nd:Yag solid state laser (λ_0= 532.15 nm), and He-Ne laser (λ_0=632.8 nm) were focused through a 100x objective on to the samples and Raman scattering was back collected through the same microscope objective. Power at the samples was kept at 10 μW by interposing a neutral density filter in order to avoid any thermal and photochemical damage; the diameter of the confocal hole was set at 400 μm and collection times varied in the range of 10 to 900 seconds. Some of the spectra required post-processing involving spike removal and multi-point baseline subtraction.

5.3.2 Silver Island Film Fabrication

Solid sample pigments were mounted on KBr crystals (International Crystal Laboratories) by simply pressing the powders on the halide blocks. Alternatively, the dyes were re-crystallized from methanolic solutions on glass slides or Aluminum coated slides (Thermo Electron Scientific). All mounted samples were then placed in a Kurt J. Lesker Axxis e-beam deposition system (Pittsburg, PA) with a base pressure of 10^{-6} Torr and AgIFs of approximately 6 – 8 nm thickness were fabricated on the sample surface. The mass thickness and deposition rate (1 Å/sec) was monitored using a Sigma Instruments 6 MHz gold plated QCM (Fort Collins, Colorado).

5.3.3 Suppliers and Sample Preparation

Eosin Y high purity (CAS# 17372-871); Eosin Y free acid 90-95% purity (CAS# 15086-94-9), Alizarin 97% (CAS # 72-48-0) and Purpurin (CAS# 81-54-9) were all purchased form ACROS organics and used as received, without further purification; Carminic acid was purchased from Aldrich (CAS # 1260-17-9), and re-crystallized from methanol. Samples of red extracts from brazilwood and lac dye, made from Laccifer Lacta secretion were purchased from Kremer pigments Inc (36020; indicated as extracted from Coccus Lacta on the supplier's original label), together with the pigment alizarin Crimson dark PR83 (2361). Historic samples of pink madder dark (Newman); Cochineal Carmine lake (F. Weber) and the distilled water extract of Kermes scale insects were obtained from the Forbes collection of pigments. Comprising over 1600 specimens assembled in the 1930s by E. W. Forbes , former director of the Fogg Art Museum at Harvard University, Boston, this collection is widely used as a source of reference Materials for Museum research.[94]

Colorants were also extracted from wool fibers dyed with alizarin and alizarin red S (9,10-Dihydro-3,4-dihydroxy-9,10-dioxo-2-anthracenesulfonic acid, sodium salt; $C_{14}H_7NaO_7S$ C.I. 58005; sodium alizarinsulphonate) and madder.

5.3.4 Extraction of Colorants from Dyed Fibers

A solution of hydrochloric acid (Aldrich, reagent grade 37%)/ distilled water/ methanol (Aldrich) was prepared, with volume ratios of 2:1:1. A small segment of the dyed fiber, measuring approximately 3 mm was then placed in a conical vial and covered with 0.1 ml of the solution. The vial was then positioned in a hot water bath and after approximately 10 minutes, the extract form the fiber was pipetted onto a glass or aluminum coated slide and let dry in air.[95]

5.3.5 Calculations

All geometry optimization and theoretical calculations of normal vibrational modes were conducted with Gaussian 2003 edition.[96] The B3LYP/6-311G^{++}(d,2p) basis set of the DFT method was used to calculate the normal vibrational modes for alizarin, purpurin, and brazilein. The B3LYP/6-311G(d) basis set of the DFT method was used to calculate the normal vibrational modes for brazilin and kermesic acid.

5.4 Results and Discussion

In this work, all the materials examined have been grouped according to common origin and are discussed separately. Tables are presented for each compound, reporting the wavenumbers of the observed bands in each SERS spectrum and normal Raman spectrum (when applicable). The tables also contain a comparison of the experimental values with values found in the literature and calculated bands (when available). Attribution for the vibrational modes are also proposed, derived from the literature. Bands observed that are considered most suitable, as markers for unambiguous identification of the individual colorants have also been indicated.

5.4.1 Madder Dyestuffs and Synthetic Derivatives (Alizarin, Purpurin, Pink Madder Dark, Alizarin Crimson, Alizarin Red S)

As previously mentioned, both the normal Raman spectra[82] and SERS spectra of solutions of red alizarin dye have been published[85-88]: our results are in good agreement with earlier published data. Slight variations in the intensity ratios of selected bands with the synthetic compound compared to actual pigment powders were observed. A SERS spectrum of synthetic alizarin was obtained with a 632.8 nm excitation (Figure 5.2 -A). While some residual fluorescence occurs, the peaks due to the dye are very intense and sharp. Vibrational bands were

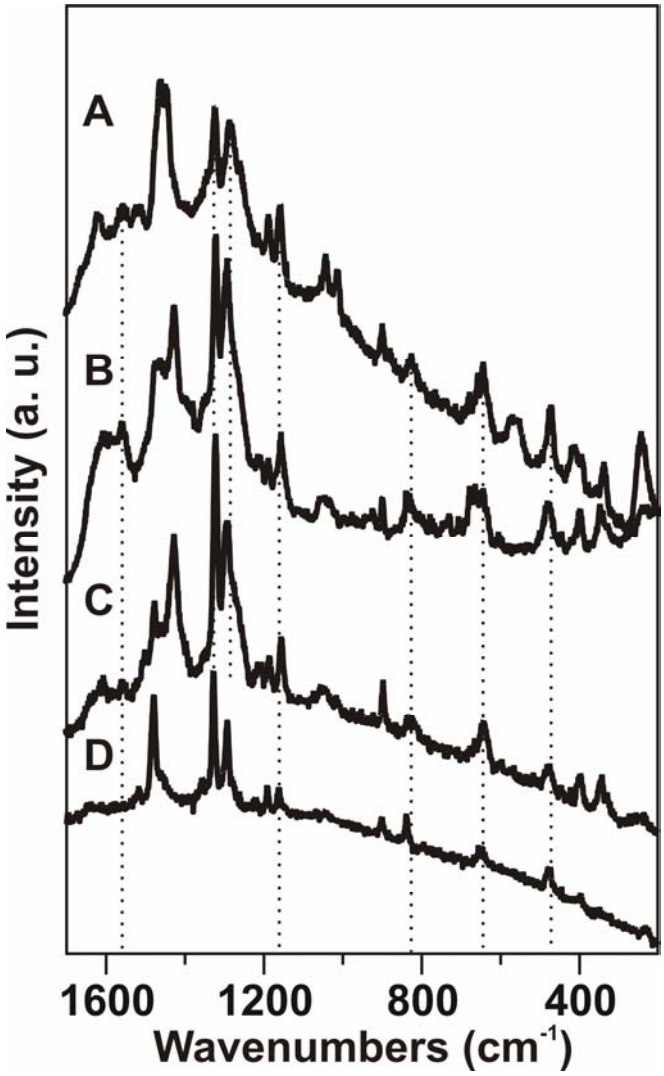

Figure 5.2 SERS spectrum of synthetic alizarin (A), excited with 632.8 nm laser, and spectra of specialty artists' pigments pink madder dark (B) and alizarin crimson dark (C). The normal Raman spectrum of pink madder dark is denoted by D.

SERS	Assignments[11]	Published bands[11]	Calculated
243m			243
339w	Skeletal Vibration	336vw (Normal Raman-alkaline)	340
396	Skeletal Vibration	398 m (SERS pH11.8)	382
414w	Skeletal Vibration	417vw (Normal Raman-alkaline)	414
*473m	Skeletal Vibration	473vw (Normal Raman-alkaline)	475
564w,br	Skeletal Vibration	577w (SERS pH 11.8)	563
645m,br			651
826w	γ(C-H)/ γ(C-O)	827vw (pH 5.5)	821
*900w	γ(C-H)	901vw (Normal Raman-alkaline)	890
1013m	υ(CC)/δ(CCC)	1011w (Normal Raman-solid)	1016
1042m	δ(CCC)	1044s (Normal Raman-alkaline)	1033
*1157s	υ(CC)/δ(CH)	1157w (SERS pH 11.8)	1151
1186s	υ(CC)/δ(CH)/δ(CCC)	1185m (SERS pH 11.8)	1177
1284s	Y(CO)/υ(CC)/δ(CCC)	1282s (Normal Raman-alkaline)	1278
1323s	Y(CC)	1323m (Normal Raman-alkaline)	1317
1448s,br	υ(CO)/δ(COH)/ δ(CH)	1451 (SERS pH 5.5)	1452
1461s,br	Y(CO)/υ(CC)/ δ(CH)	1461vs (Normal Raman-alkaline)	1461
1558w,br	υ(CC)		1560
1623wbr	υ(C=O)	1624s (Normal Raman-alkaline)	1626

Table 5.1 Principal experimental, calculated Raman vibrations, and previously published SERS spectra of synthetic Alizarin. Legend: vw: very weak; w: weak; m: medium; s: strong; vs: very strong; sh: shoulder; br: broad; υ: stretching; δ: in-plane bending; γ out-of-plane bending. Bands marked with an asterisk are suggested as markers for unambiguous identification of alizarin red dye in an unknown. Vibrational assignments were obtained from Canamares et al. where the authors utilized Ag colloids to collect SERS spectra of alizarin.

observed at 243, 339, 396, 414, 473, 564, 645, 826, 900, 1013, 1042, 1157, 1186, 1284, 1323, 1448, 1461, 1556, and 1623 cm^{-1} (table 5.1). The usefulness and ready applicability of the reference SERS spectrum of the pure dye is demonstrated by successful examination of the lake pigments from specialists pigment suppliers including pink madder dark (Figure 5.2B and 5.2D) and alizarin crimson dark (Figure 5.2Cand can be compared with the normal Raman spectrum of pink madder dark (Figure 5.2D). Significant enhancement is observed as well as more detailed spectra. In particular, the normal Raman spectrum of the powder acquired on the historic pigment pink madder dark, shows a more significant fluorescence background and fewer bands are observed at 239vw, 401vw, 479w, 659w, 860w, 901w, 1160w, 1190w, 1219vw, 1292m, 1326vs, 1355w, 1679s and 1517w cm^{-1}. The identification of the colorant of a wool fiber dyed with Alizarin red S was also obtained with SERS (Figure 5.3), which demonstrates that AgIFs have potential to be utilized on works of art in the future. Furthermore, all spectra recorded show good agreement with the reference spectrum of alizarin.

A highly reproducible SERS spectrum of purpurin is shown in Figure 5.4A. Substantial improvement of S/N with respect to the spectrum recorded with normal Raman spectroscopy was achieved (Figure 5.4B). The fluorescence background is virtually completely quenched using an excitation line of 632.8 nm. SERS spectra of purpurin in solution of aggregated citrate-reduced silver colloids have been reported recently, showing substantial pH dependence.[86] Our results compare well with data reported for purpurin at pH 6.2, i.e. when the dye is dissociated in the monoanionic form. This may be due to the fact that in the powder inter and intramolecular interactions of the carbonyl and phenol groups occur.

Calculated Raman bands and observed SERS bands are shown in Table 5.2. Based on the vibrational data collected we can distinguish between alizarin and purpurin on the basis of

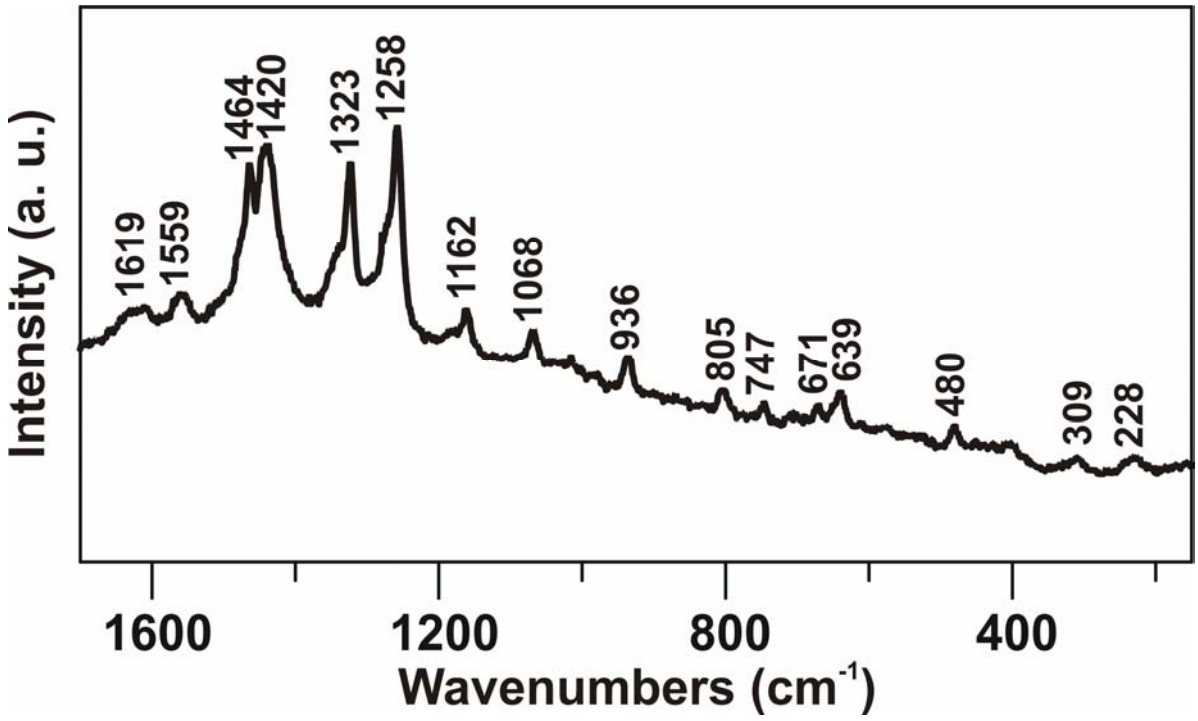

Figure. 5.3 SERS spectrum of the colorant extract from a sample wool fiber dyed with Alizarin Red S, and deposited on an Aluminum coated slide, excited with 632.8 nm laser (accumulation time: 180 seconds)

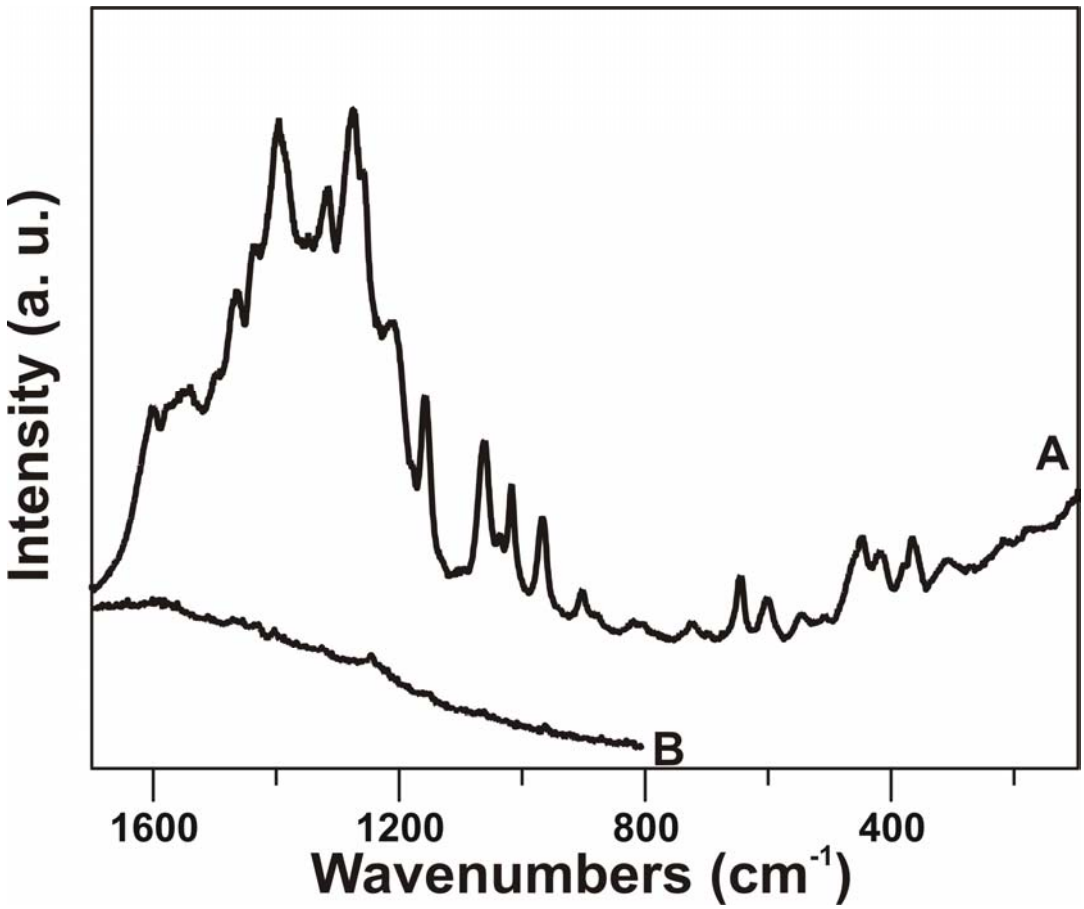

Figure 5.4. SERS spectrum (A) and the normal Raman spectrum (B) of synthetic purpurin, excited with 632.8 nm laser (accumulation time: 60 seconds, for two cycles).

SERS	Published (SERS, pH 6.2)[12]	Calculated
313vw	309	334
*366m	364	356
422m	425	421
451m	447	445
513vw	512	519
549w	551	579
606m	603	622
648m	647	644
728w	737	721
806w		810
824w		823
905w	900	890
*970s	968	975
*1020m	1015	1015
1040w		1047
1064s	1068	1079
1160s	1153	1162
1213m		1224
1277s		1271
1319s	1326	1318
*1401s,br	1407	1415
1439vw,sh	1435	1438
1468s	1471	1463
1545w,br		1561
1606m	1616	1597

Table 5.2 Principal experimental, calculated Raman vibrations, and previously published SERS spectra of synthetic Purpurin. Legend: Vw: very weak; w: weak; m: medium; s: strong; vs: very strong; sh: shoulder; br: broad; υ: stretching; δ: in-plane bending; γ. Bands marked with an asterisk are suggested as markers for unambiguous identification of purpurin in an unknown.

the presence of the marker bands centered at 243, 473 and 1186 cm^{-1} (alizarin) and 971, 1063, 1401 and 1606 cm^{-1} (purpurin). In order to differentiate these two dyes from all other red dyestuffs discussed in this paper, we propose to use bands at 473, 900 and 1157 cm^{-1} for alizarin and 366, 606, 970, 1020 (also observed for carminic acid at 1021), and 1401 cm^{-1} for purpurin.

5.4.2 Coccid Dyestuffs (Kermes, Cochineal, Lac Dye)

SERS spectra of kermes were taken for the distilled water extracts of the Kermes scale insects (Figure 5.5A). It is important to note the dramatic increase in S/N with respect to the normal Raman spectrum, both experimentally observed in this work (Figure5.5B) and previously published normal[97] and FT- Raman.[79] The spectra collected correlate well with calculated bands (Table 5.3).

The 632.8 nm excitation SERS spectrum for Carminic acid (Figure 5.6A) is compared with the normal Raman spectrum (Figure 5.6B). The SERS spectrum depicts vibrational bands at 122, 225, 454, 756, 847, 962, 1021, 1043, 1196, 1319, 1380, 1441, and 1570 cm^{-1} while the normal Raman spectrum provides little vibrational information. A normal Raman spectrum of carminic acid has been published[79], with excitation line of 780 nm and bands at 465 w, 474 w, 1108 w, 1257 m, 1314 s, 1440 m, 1489 m, 1592 m, and 1645 m cm^{-1}. Despite the excellent quality of the spectrum of carminic acid, attempts at recording a good spectrum of the historic pigment cochineal only resulted in a spectrum still dominated by high fluorescence and with poorly resolved bands (Figure 5.7). Nonetheless, the spectrum shows a drastic improvement compared to the normal Raman spectrum observed in our experiment and shows a characteristic profile that is believed to provide sufficient indications for the identification of unknowns.

Figure 5.8 depicts both a normal Raman spectrum (B) and SERS spectrum (A) of lac dye. While an adequate normal Raman spectrum of lac dye is obtainable, the SERS spectrum

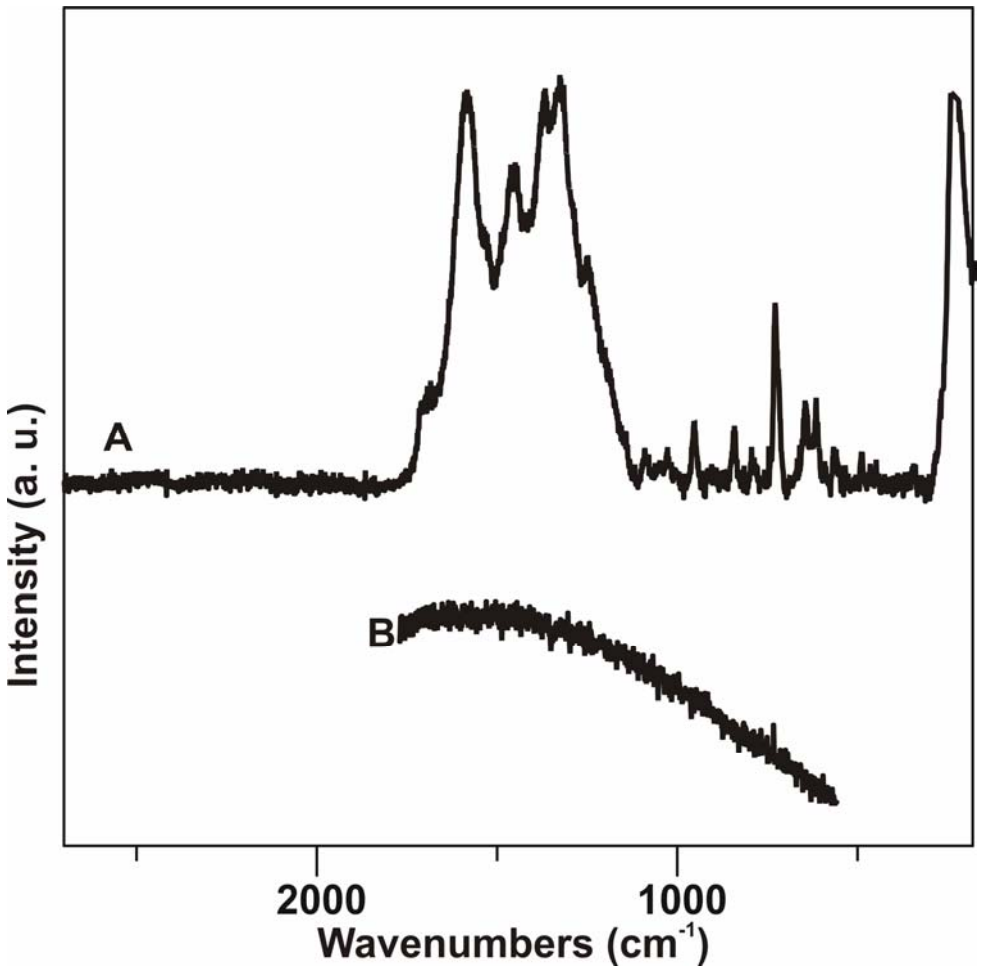

Figure 5.5 SERS spectrum (A) recorded on distilled water extract from Kermes scale insects, successively deposited on an Aluminum coated slide, excited with 632.8 nm laser (accumulation time: 60 seconds, after multi-point baseline correction) and the Normal Raman spectrum (B).

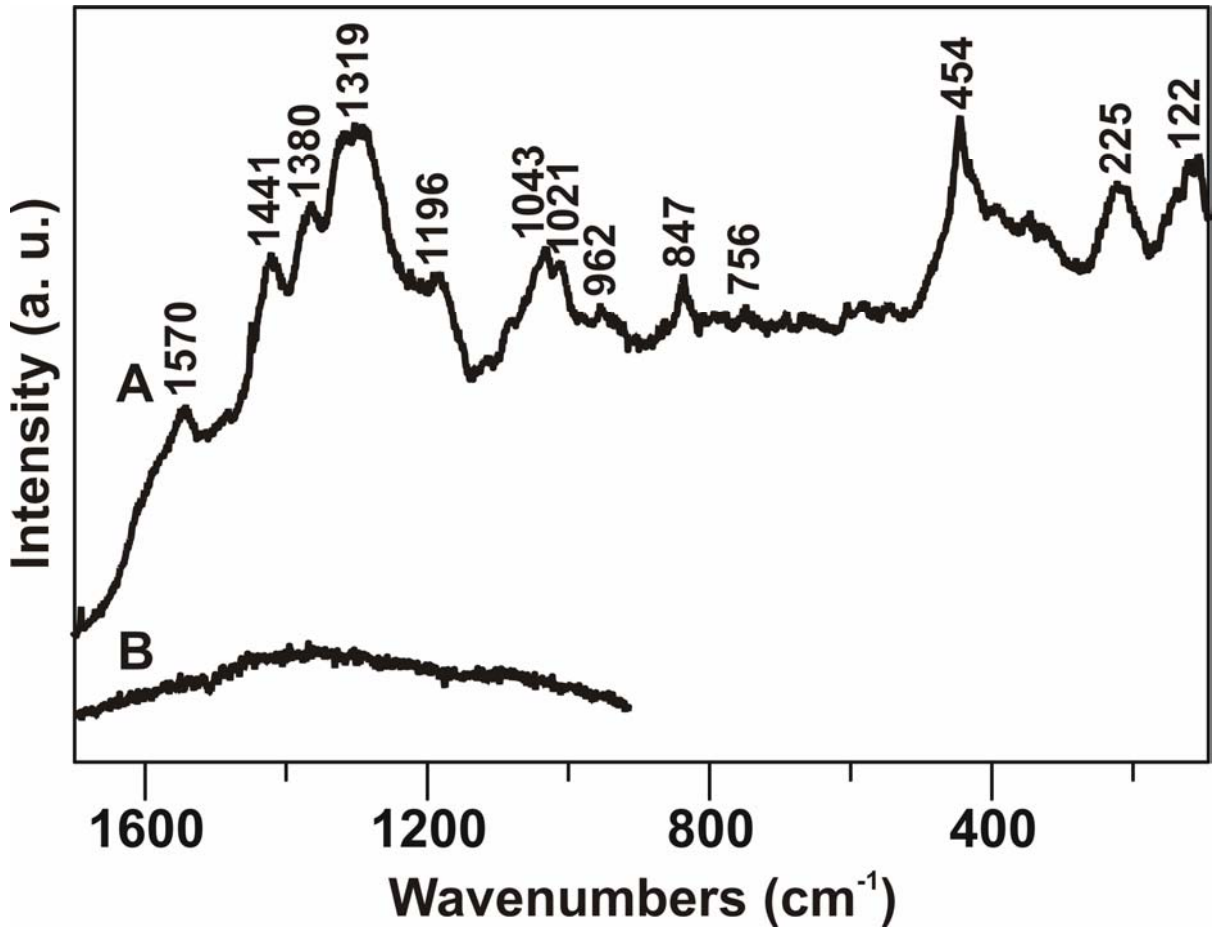

Figure 5.6 SERS spectrum (A) and the normal Raman spectrum (B) of synthetic carminic acid, excited with a 632.8 nm laser.

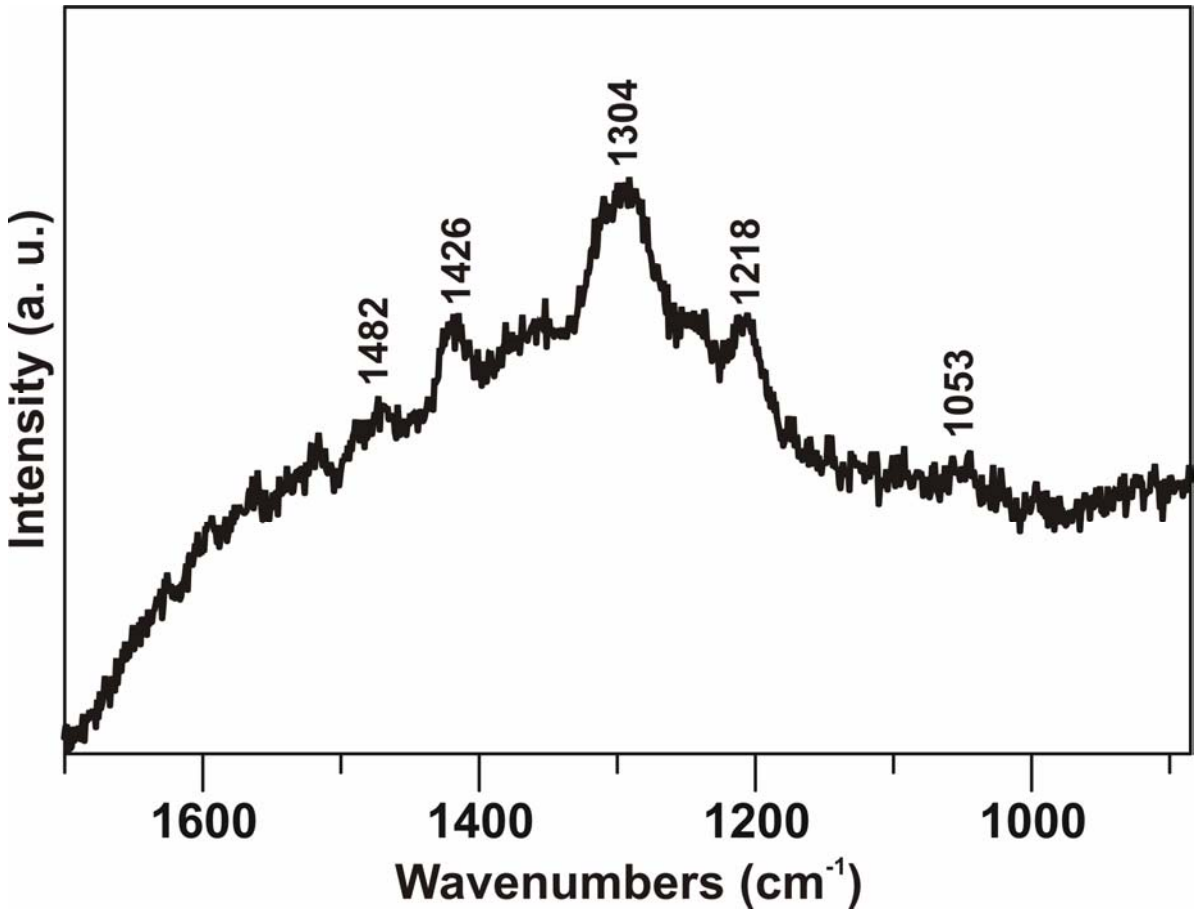

Figure 5.7 SERS spectrum of cochineal lake excited with 632.8 nm laser (accumulation time: 60 seconds for two cycles).

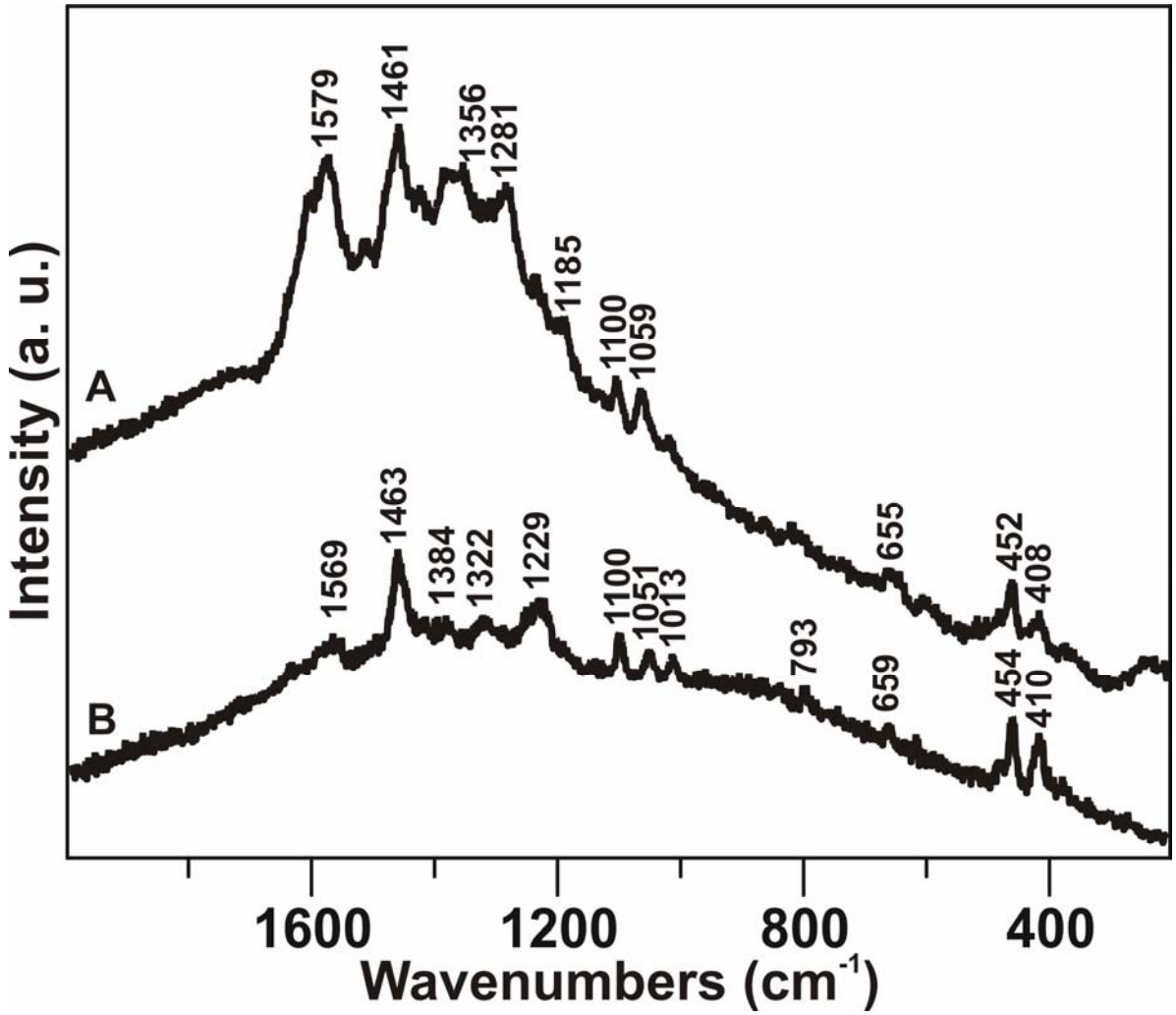

Figure 5.8 SERS spectrum of lac dye (A), excited with 632.8 nm laser, compared with normal Raman spectrum of the same material (B) (632.8 nm laser excitation, accumulation time: 120 seconds for 8 cycles).

Calculated	SERS
244	240vs
372	
410	
479	
499	
539	
556	564vw
576	
597	615m
627	
653	646m
710	
736	729s
760	
785	794vw
811	
863	842m
868	
922	
940	953m
1013	
1028	1029w
1085	1091w
1139	
1168	
1205	
1317	1330vs
1391	1371vs
1448	
1458	1457vs
1484	
1603	1590vs
1672	1703sh

Table 5.3 Principal experimental bands observed for kermes scale insects and their water extract, compared with calculated Raman vibrations of kermesic acid. Legend: vw: very weak; w: weak; m: medium; s: strong; vs: very strong; sh: shoulder; br: broad.

provides enhanced detail especially in the wavenumber range 1200-1600 cm^{-1}. Low fluorescence levels were observed and spectra was easily reproducible, with observed bands at 408w, 452m, 655w, 1059m, 1100m, 1185m, sh, 1232m, sh, 1281s, 1356m, 1386m, 1425m, 1461s, 1518m, and 1579s cm^{-1}. Based on our observation we propose that bands at 452 (keeping in mind that carminic acid has a band at 454 cm^{-1} and purpurin at 451 cm^{-1}), 1059, 1100, 1281 and 1579 cm^{-1} can be used for unambiguous identification of this colorant in unknown artifacts.

5.4.3 Redwoods (Brazilwood)

The red extract of brazilwood has been analyzed with both SERS and normal Raman (Figure 5.9) and compared with theoretical calculations of both brazilin and brazilein (Table 5.4). SERS spectra were recorded with 2 excitation wavelengths (532 [Figure 5.9A] and 632.8 nm [Figure 5.9B]) on the same dyestuff particle and important variations in the vibrational modes were observed. Similarly, it was possible to record a normal Raman spectrum (Figure 5.9C) of the dye, but this presented some differences with the SERS spectra, in particular with bands at 886m, 919m, 1233s, 1281s, and 1553w cm^{-1} that are not evident in the 633 nm excited SERS spectrum (Figure 5.9B) and variation in intensity of bands centered at 993w, 1135w, 1204m, br and 1398s cm^{-1}. It is important to note that observation of the dye powder under the stereomicroscope in visible light showed a mixture of bright ruby-red particles, transparent particles and dark grains, therefore it is possible that different colors (and different spectra) account for the mixture of redwood dyestuffs (different molecular formulas that constitute this colorant). In fact, some of the spectra presented a combination of the bands shown in Figure 5.9 for the normal and SERS spectrum, possibly supporting this hypothesis. Finally, both the experimental SERS and normal Raman spectra are in good agreement with the calculated vibrational bands (Table 5.4).

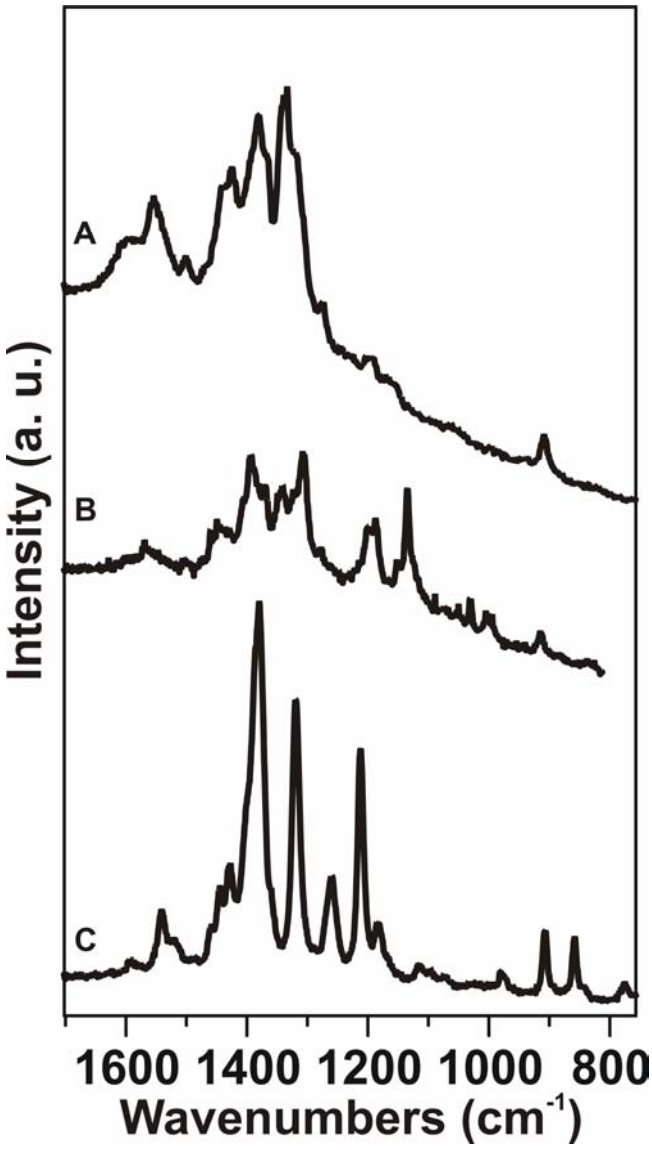

Figure 5.9 SERS spectra of brazilwood excited with 632.8 nm (accumulation time: 60 seconds for 3 cycles) (A) and 532 (accumulation time: 60 seconds for 3 cycles) (B) nm laser, compared with normal Raman spectrum of the same material (C) excited with 632 nm laser line (accumulation time: 120 seconds for 8 cycles).

Normal Raman	SERS 633	SERS 532	Assignments[7,8]	Published (FT-Raman)[7,8]	Brazilin Calculations	Brazilein Calculations
777w			γ(CO) + γ(CH)	767w	775	
866m					865	866
	913	910m			902	
919m						923
993w			υ(C-C) + υ(C-O)	990vw	981	
	1002m				1010	1009
	1030m		Ring stretching	1032		1045
1092vw			δ (C-H)i.p. wood cellulose	1092w		
1115vw			δ (C-H)i.p. wood cellulose	1115w		
1135vw	1134vs				1133	
	1189s				1191	
1204m	1200s	1198br	δ (C-C)	1203w	1200	
1233vs			υ(C-O) + υ(C-C)	1230sh	1235	1231
1281s	1280sh	1278sh			1279	1276
	1307vs				1311	1302
1339vs	1340m	1339s			1334	
	1370sh			1377	1372	1374
		1383s			1348	
1398vs	1393s,br				1411	
		1427s				1429
1445m	1449m	1441sh		1443w	1438	1436
1461m	1460w				1465	1455
1475sh,br						1478
	1505vw	1503w		1502[b]	1490	
1553m		1554		1550w		1548
	1567s		υ (C=C)	1564s	1562	
1600w	1598vs		υ(C-C)	1600s		1599

Table 5.4 Principal experimental (at two excitation wavelengths), calculated Raman vibrations, and previously published SERS spectra of brazilwood Legend: Vw: very weak; w: weak; m: medium; s: strong; vs: very strong; sh: shoulder; br: broad; υ: stretching; δ: in-plane bending; γ.

5.4.4 Early Synthetic Dyes (Eosin Y)

The disodium salt of this dye has a deep red color and showed an intense normal Raman spectrum (Figure 5.10A) on a slightly sloping fluorescence background. Fabrication of a AgIF on synthetic dye caused a total annihilation of this residual fluorescence (Figure 5.10B). An excitation wavelength of 632.8 nm was used to obtain a normal Raman spectrum and a SERS spectrum. The normal Raman spectrum had the following vibrational bands: 109w, 203w, 286,w, 343w, 407w, 448 vw, 477w, 645m, 710m, 772w, 963w, 1016w, 1090, 1174w, 1253w, sh, 1280 vs, 1314w, 1349br, m, 1474m, 1501vs 1570w, 1620m cm^{-1} (Figure 5.11A). The SERS spectrum correlated well with the normal Raman spectrum with bands located at 962w, 1016w, 1059w, 1091w, 1176w, 1251w, sh, 1279vs, 1312w, 1347m, 1473m, 1501vs, 1567w, and 1622m cm^{-1} (Figure 5.11B). Surprisingly, no normal Raman spectrum could be acquired on the yellow powder of the free acid of 2,4,5,7- tetrabromofluorescein, while an enormous enhancement was achieved with SERS. Bands were observed at 285m, 361w, 472s, 558m, 642m, 709m, 766m, 926vw, 958w, 1090w, 1177s, 1251sh, w, 1327vs, 1462 sh, m, 1495s, 1559 sh, m, 1621s cm^{-1} (Fig. 5.11), which correlate well with previously published SERS results (288s, 473s, 619w, 639w, 709w, 1177s, 1235w, 1281w, 1333vs, 1457w, 1501s, 1563w, 1617s cm^{-1})[19]. We therefore propose to use bands at 203, 645, 710, 1280, 1501 cm^{-1} to identify Eosin Y disodium salt, and 285, 472 (also present in the spectrum of alizarin) 642, 709, 1177, 1327 and 1495 cm^{-1} to identify the free acid.

5.5 Conclusions

In this paper, we have described an innovative SERS technique based on e-beam deposition of AgIFs for the analysis of organic red colorants. On the basis of the spectral

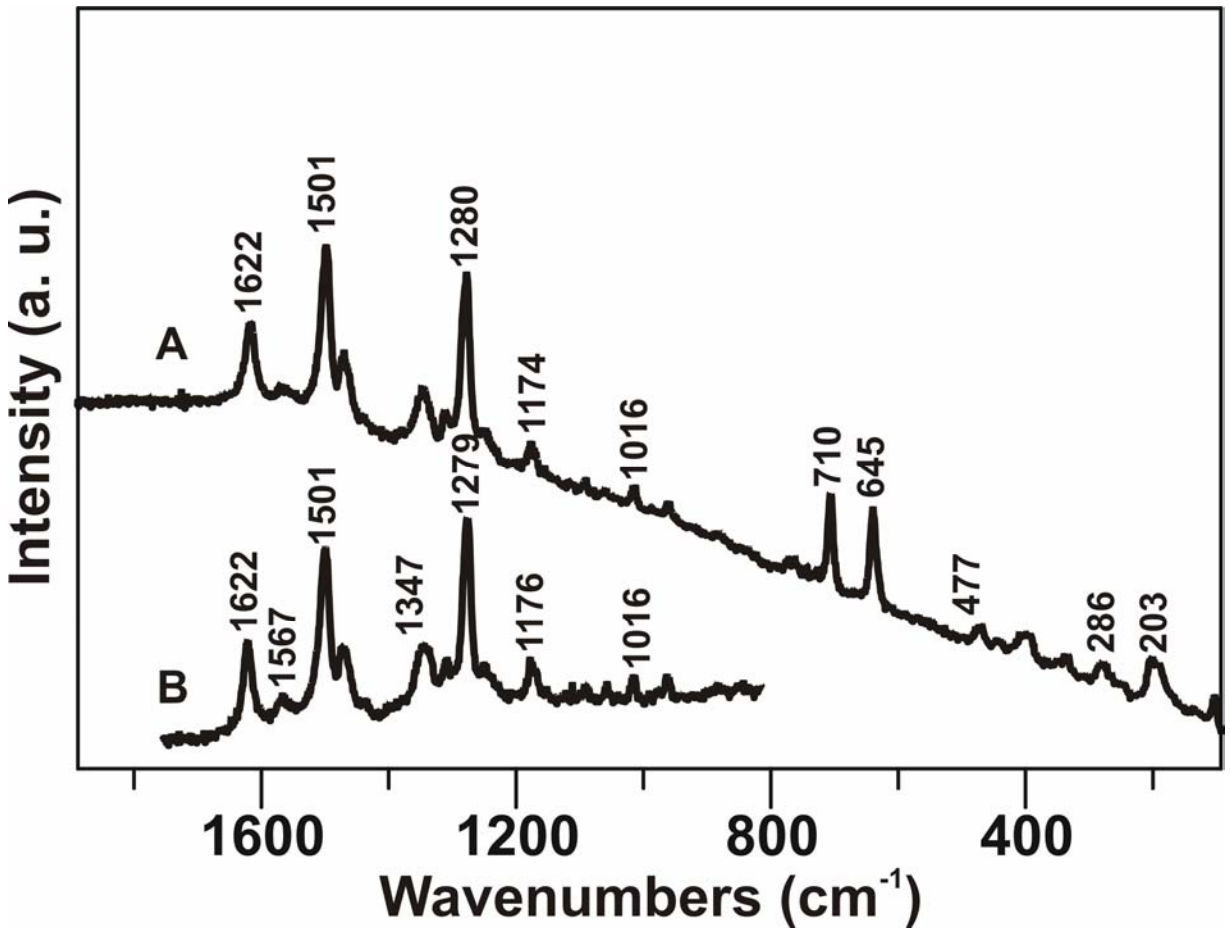

Figure 5.10 Normal Raman spectrum of synthetic Eosin Y high purity in its disodium salt form (A) (accumulation time: 80 seconds twice), compared with SERS spectrum (B), excited at 632.8 nm , of the same material (accumulation time: 300 seconds for three cycles)

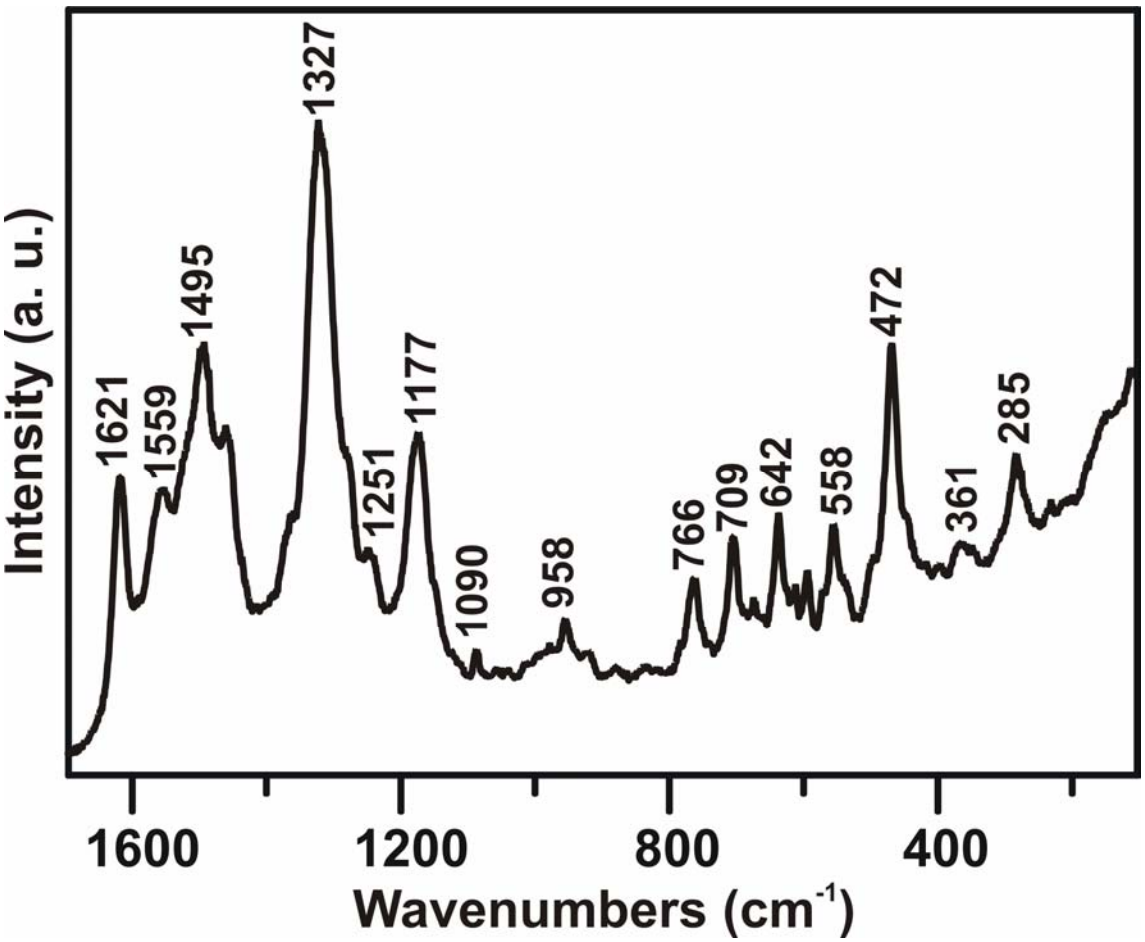

Fig. 11. SERS spectrum of synthetic Eosin Y free acid (632.8 nm laser excitation, accumulation time: 90 seconds for two cycles).

evidence presented here it seems possible to differentiate the most common historical artists' red lake pigments and dyestuffs, given the highly detailed SERS spectra obtained. The work presented here may constitute a first step in the direction of enabling researchers to identify unknown pigments on historical artifacts without further sample manipulation such as dye extraction. However, when analyzing actual paint layers, unknown aspects such as sample preparation, influence of other components (mineral pigments and fluorescent organic compounds such as varnishes and binding media) and possible use of mixtures of red lakes in a single brushstroke or adjacent layers are to be taken into account and may cause interference in the analysis. A certain success has been obtained by the authors in analyzing woolen fibers dyed with alizarin and alizarin red S, however, the experiments underscored the necessity of developing finely tuned, less aggressive extraction procedures than those currently in use for High Performance Liquid Chromatographic analysis of these materials (HPLC). In fact, SERS is a surface method and is therefore highly sensitive to impurities and matrix effects due to components of the degraded proteinaceous structure of the wool that are present in higher proportion than the colorant of interest.

Other areas of future work may involve the expansion of the range of examined dyestuffs to the natural yellow and green dyes, and the study of the effects on the SERS spectra recorded. of precipitation of the different dyestuffs on a variety of inorganic substrates.

Chapter 6

SiO_2 AgFONs: A Highly Sensitive SERS substrate for the Identification and Characterization of Artists' Red Dyes and Their Mixtures

6.1 Introduction

The identification of artists' materials in works of art is important in the field of art history, as well as for conservation and restoration efforts. Furthermore, the analysis of artists' materials can often be applied to date and authenticate artifacts. Identifying natural and early synthetic dyestuffs is of paramount importance, as these colorants are often not stable in light and, if exhibited without knowledge of their photo-sensitivity, can fade very rapidly. Raman spectroscopy is a noninvasive method that has been successfully applied to characterize many artists' pigments and dyes.[77-81] Because every molecule scatters light uniquely, Raman spectroscopy is an excellent analytical tool to "fingerprint" unknown compounds. However, because only subnanogram levels of these dyes are needed to impart intense color to fibers or paint, normal Raman spectroscopy often lacks the sensitivity to probe these materials at such low concentrations. Furthermore, many organic dyestuffs of natural origin are extremely fluorescent, an effect that dominates the weak optical process of Raman scattering.

Recently, a number of publications have reported the use of surface-enhanced Raman spectroscopy (SERS) to successfully characterize and identify highly fluorescent red dyes and lake pigments.[29,30,85,86,98-101] It is well known that the SERS effect significantly enhances the Raman scattering signal when the Raman-active molecule is spatially confined within the electromagnetic fields generated upon excitation of the localized surface plasmon resonance (LSPR) of the nanostructured noble metal surface.[8] The SERS signals of ensemble-averaged molecules demonstrate enhancements up to 8 orders of magnitude over normal Raman signals.[19,20] Furthermore, the use of a noble metal SERS substrate can quench fluorescence, therefore reducing or even removing harmful background. Additionally, resonance Raman will occur when the Raman excitation wavelength is of sufficient energy to promote an electronic

transition in the molecule of interest, from the ground to some electronically excited state resulting in further enhancement of the normal Raman signal (~10^2).[6,19] Because each of these dyes absorb in the visible region, resonance Raman and pre-resonance Raman enhancements should occur when using 532.17 nm and 632.8 nm excitation wavelengths, respectively. Furthermore, when the LSPR of the SERS substrate is also in the proper energy region, the conditions of surface-enhanced resonance Raman spectroscopy (SERRS) are met, which will result in enhancement factors that are approximately the product of the enhancement factors for non resonant SERS of the substrate and the resonant Raman spectrum of the adsorbate.[6] Throughout this work, the authors will use the term SERS to describe all data proceeded with either "pre-resonance", "resonance", or "non-resonance" to describe the experimental conditions. Finally, another benefit of this technique is that it can be used to identify extremely small amounts (7×10^{-15} g) of material,[102] which is often all that is available for analysis when a sample is removed from priceless museum objects.

Previously, we have successfully employed silver island films (AgIFs) as SERS substrates to identify and characterize several red lake dyes.[29,30] However, because AgIFs are non-uniform, it can be difficult and time consuming to collect consistent spectra.[103] This is particularly relevant when transferring the methodology from pure, commercially available reference compounds to artists' materials, which often contain impurities and are present in complex mixtures that further complicate spectral interpretation. Alternatively, this work uses silver film over nanospheres (AgFONs) as SERS substrates to overcome these issues resulting in the acquisition of consistent spectra. The Van Duyne group has successfully used AgFONs as SERS substrates for the detection of analytes such as glucose and anthrax.[23,89,91] Briefly, AgFON fabrication involves drop coating polystyrene or SiO_2 nanospheres onto a clean substrate

and then thermal or electron beam (e-beam) depositing ~200 nm of Ag over the nanosphere mask.[89,104] AgFONs are not only easily fabricated, economical, and stable for several weeks,[89] but are also composed of a uniform surface which provides highly consistent surface-enhanced Raman (SER) spectra. Furthermore, AgFONs have been successfully used to detect extremely small amounts of analyte which makes them ideally suited for analyzing the small samples often available in a museum setting.[27,28] The LSPR of a AgFON can be fine tuned simply by changing the size of the underlying nanospheres, ensuring that the substrate can be excited with numerous laser wavelengths.[89] As a result, AgFONs can be utilized with any Raman system, thus effectively allowing the custom-tailoring of the substrate/laser system for each specific application.

SERS has been successfully applied in the past to identify samples containing a single reference dye.[29,30,85,86,98-100] However, there has been little work focusing on the identification of individual components in dye mixtures. The ability to accurately characterize dye mixtures is necessary because a combination of dyes is often employed in real works of art. For example, in an extensive survey of 15th-16th century paintings from the National Gallery in London, a variety of dye combinations have been identified including: (1) lac with a possible addition of kermes; (2) madder and kermes; (3) brazilwood and kermes; (4) kermes and cochineal and, (5) cochineal and madder.[92] Furthermore, mixtures of brazilwood with cochineal and madder have been identified in works by Vincent Van Gough.[105] Therefore, in order for SERS to be a viable technique to analyze dye samples in artwork, the method must be capable of distinguishing individual dyes in mixtures. Murcia-Mascarós and co-workers were able to successfully identify alizarin in a mixture of alizarin and carminic acid using Raman spectroscopy.[101] The authors prepared a Zr-Ormosil polymer complex that not only selectively incorporated alizarin but

quenched fluorescence and induced intense Raman spectra.[101] While the Zr-Ormosil polymer can effectively be used to identify alizarin, it is materials specific. Alternatively, a materials general substrate such as an AgFON would allow for the identification of a variety of individual dyes within mixtures.

The work presented herein utilizes AgFONs as materials general SERS substrates to characterize several red dyes and organic molecules including: alizarin (Fig. 6.1A), purpurin (Fig. 6.1B), carminic acid (the chromophore in the dyestuffs cochineal) (Fig. 6.1C), and laccaic acid (contained in lac dye, a natural product comprising a mixture of acids) (Fig. 6.1D). The pre-resonance SER spectra collected in this work show higher resolution and improved constancy than what was observed in our previous work.[29,30] Furthermore, to the best of the authors' knowledge, the pre-resonance SER spectra taken on AgFONs of a sample of the artists' pigment cochineal are the highest resolution to date.[29,30] Because the red dyes absorb in the visible light region, resonance and pre-resonance Raman conditions can be met by using both 532.15 nm or 632.8 nm laser excitation wavelengths, respectively.[106,107] Additionally, when the LSPR of the SERS substrate falls within the absorption region of an adsorbed dye, the conditions of resonance SERS will be met. Experiments were therefore conducted with carminic acid and lac dye to optimize the combination of AgFON LSPR maxima and laser excitation wavelength for the analysis of these dyes. Because artists often use a mixture of dyes in their work, it is imperative that characterization techniques are able to distinguish between multiple materials in a single sample. Therefore, experiments were carried out to demonstrate that AgFONs can be used to effectively identify dyes in dye mixtures. AgFONs were successfully applied to characterize individual dyes in mixtures of (1) alizarin and lac dye, (2) alizarin and purpurin, and (3) lac dye and purpurin.

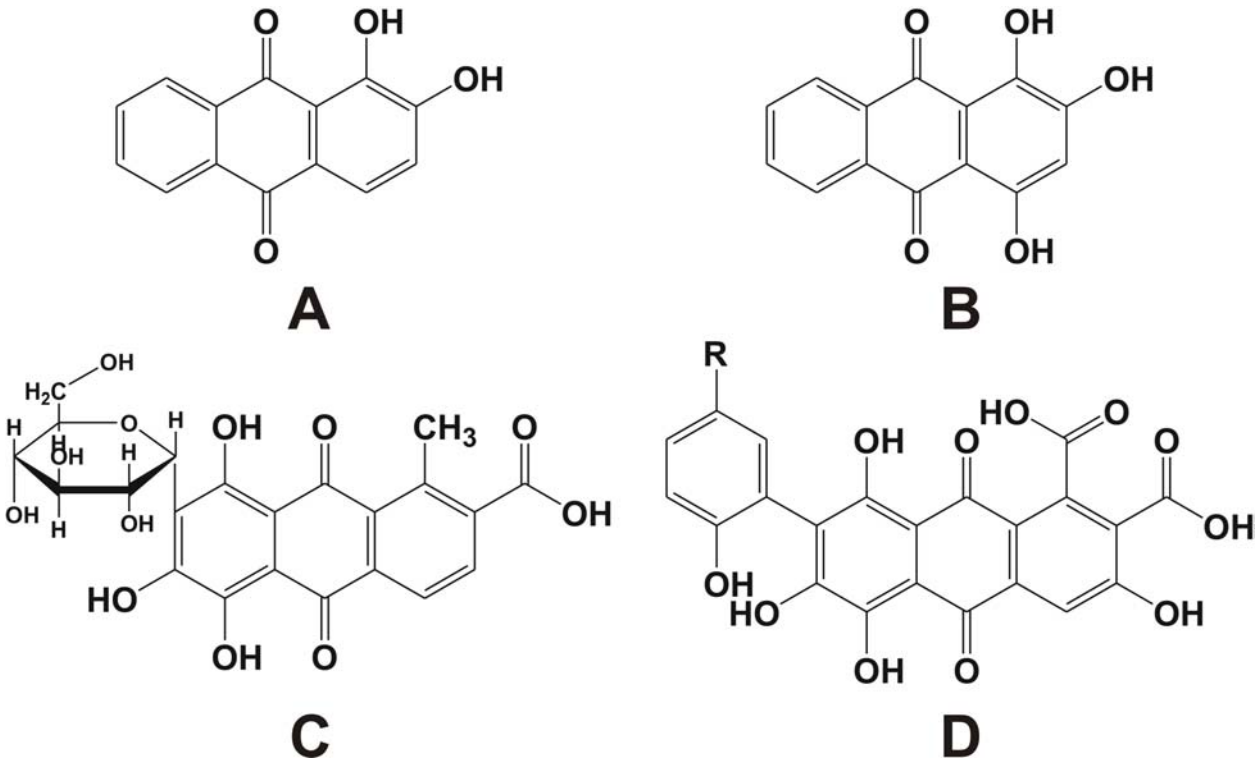

Figure 6.1 Natural and organic red compounds (A) alizarin, (B) purpurin, (C) carminic acid, and (D) 5 structures of laccaic acid are present in lac dye: laccaic acid A (R = $(CH_2)_2NHCOCH_3$), laccaic acid B (R = $(CH_2)_2OH$), laccaic acid C (R = $CH_2CH(NH_2)COOH$), laccaic acid D = flavokermesic acid, and laccaic acid E (R = CH_2NH_2). Laccaic acid A is the most prominent structure in lac dye.

6.2 Experimental Methods and Materials

6.2.1 Materials

Ag pellets (99.99%) were purchased from Kurt J. Lesker Co. (Clairton, PA). Borosilicate glass substrates, No. 2 Fisherbrand 18-mm circular coverslips were acquired from Fisher Scientific (Pittsburg, PA). Methanol, H_2SO_4, H_2O_2, and NH_4OH was obtained from Fisher Scientific (Fairlawn, VA). SiO_2 spheres with diameters of 300 nm, 390, and 550 nm were received in a suspension of water from Bangs Laboratories, Inc (Fishers, IN). Millipore cartridges (Marlborough, MA) were used to purify water to resistivity of 18 $M\Omega cm^{-1}$. Alizarin 97% (CAS # 72-48-0) and purpurin (CAS# 81-54-9) were purchased form ACROS organics and used as received, without further purification. Carminic acid was acquired from Aldrich (CAS # 1260-17-9). Lac dye, made from *laccifer lacca* secretion was obtained from Kremer Pigments Inc (36020; indicated as extracted from *coccus lacca* on the supplier's original label). The two cochineal carmine lake samples were obtained from Penick & Co. and F. Weber. The cochineal sample manufactured by F. Webber was taken from the Forbes reference collection of pigments containing over 1600 specimens of artists' materials accumulated in the 1930s by E. W. Forbes, former director of the Fogg Art Museum at Harvard University, Boston; this collection is widely used as a source of reference materials for museum research.[94]

6.2.2 AgFON Fabrication and Incubation Procedure

Glass substrates were cleaned in a piranha etch solution (3:1 H_2SO_4/30% H_2O_2) for 30 min at 80ºC. After rinsing with water, the substrates were sonicated for 60 min in 5:1:1 $H_2O/H_2O_2/NH_4OH$ in order to create a hydrophilic surface on the substrate to facilitate self-assembly of the nanosphere masks. Finally, the substrates were rinsed and stored in water for future use. Approximately 2.5 μL of SiO_2 sphere solution was drop-coated onto the pretreated

glass substrates and allowed to dry in ambient conditions. 200 nm of Ag was then deposited by electron beam (e-beam) deposition in a Kurt J. Lesker PVD 75 electron beam deposition system (Pittsburg, PA) with a base pressure of 10^{-6} Torr. The mass thickness and deposition rate (2 Å/sec) was monitored using a Sigma Instruments 6 MHz gold plated quartz-crystal microbalance (QCM) (Fort Collins, Colorado). AgFON substrates were stored in the dark at room temperature prior to use. In anticipation of SERS analysis, AgFONs were then incubated in dye solutions of $1x10^{-6}$ M or 15 ng/μL concentrations overnight. All dye solutions were made in methanol

6.2.3 Surface-Enhanced Raman Spectroscopy

A Jobin Yvon Horiba Labram 300 confocal Raman microscope was used, equipped with an Andor multichannel air-cooled open electrode charge-coupled device detector (CCD: 1024x256), BXFM open microscope frame (Olympus), holographic notch filter, and 1800 grooves/mm dispersive grating.

The excitation lines of an air cooled frequency doubled Nd:Yag solid state laser (λ_0= 532.15 nm), He-Ne laser (λ_0=632.8 nm) and a solid state diode laser (λ_0=785.7 nm) were focused through a 100x objective onto the samples and Raman scattering was back collected through the same microscope objective. Power at the samples was kept at 6 μW – 0.5 mW by using appropriate neutral density filters in order to avoid any thermal and photochemical damage. The diameter of the confocal hole was set at 500 μm and collection times varied in the range of 15 - 60 seconds. Some of the spectra required post-processing, involving spike removal due to cosmic rays.

6.2.4 UV-Vis Extinction and Reflectance Spectroscopy

UV-Vis absorption measurements were taken using an Ocean Optics (Dunedin, Fl) SD2000 fiber optically coupled spectrometer. All spectra of the methanolic solutions of the alizarin (1 x 10^{-4} M), carminic acid (1 x 10^{-4} M), cochineal (1500 ng/μL), lac dye (1500 ng/μL) and purpurin (1 X 10^{-4} M) were collected using a standard transmission geometry with unpolarized white light excitation. AgFON spectra were conducted in a reflectance geometry using a reflectance probe (Ocean Optics, Dunedin, FL) coupled to the spectrometer. AgFON spectra were acquired using a mirror-like Ag film on a glass substrate as a reference.

6.3 Results and Discussion

6.3.1 Identification and Characterization of Red Dyes on AgFON Substrates

Pre-resonance SER spectra were collected using 632.8 nm laser excitation for the red dyes alizarin (1x10^{-6} M) (Fig. 6.2A), lac dye (15 ng/μL) (Fig. 6.2B), and purpurin (1x10^{-6} M) (Fig. 6.2C). All samples were prepared on AgFONs fabricated with 390 nm diameter SiO_2 spheres. The low concentration of dyes in the sample solution was intended to mimic real museum sample sizes. The spectra were collected from each sample from five separate sample areas with extremely consistent results every time. Furthermore, all spectra obtained had higher resolution, improved consistency, and required shorter acquisition times than previously published work.[29,30] Diagnostic peaks were selected for each red dye and are labeled in Figure 6.2. Figure 6.3 compares pre-resonance SER spectra of cochineal from two different manufacturers (Fig. 6.3A and 6.3B) with a resonance SER spectrum of high purity carminic acid (the molecule that contributes the red color in cochineal) (Fig. 6.3C). The similarity of the

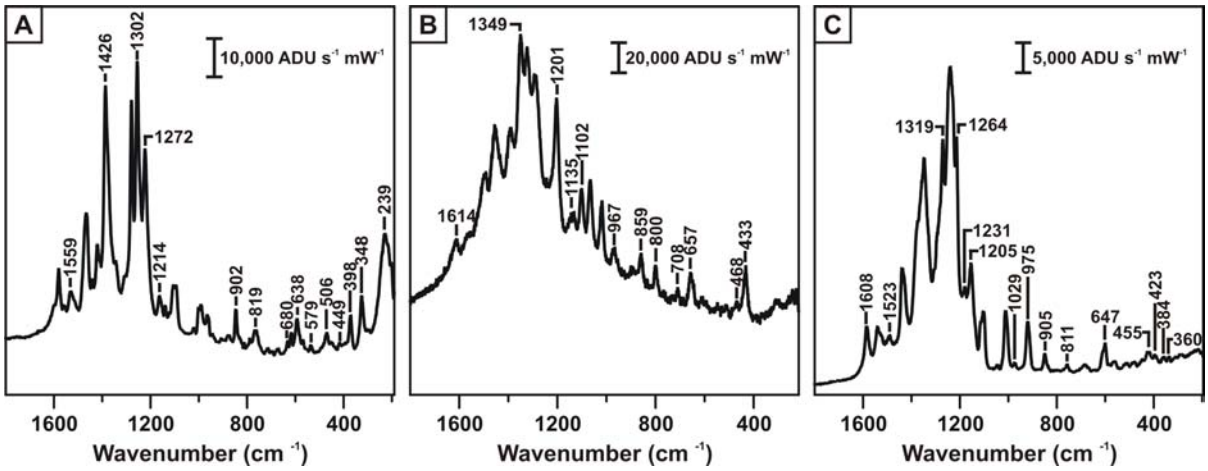

Figure 6.2 Pre-resonance SER spectra of (A) $1x10^{-6}$ M alizarin (60 sec acquisition), (B) $1x10^{-6}$ M purpurin (15 sec acquisition), and (C) 15 ng/μL lac dye (15 sec acquisition). All samples were prepared on AgFONs fabricated with 390 nm diameter SiO_2 spheres and spectra was collected with $\lambda_{excitation}$ = 632.8 nm.

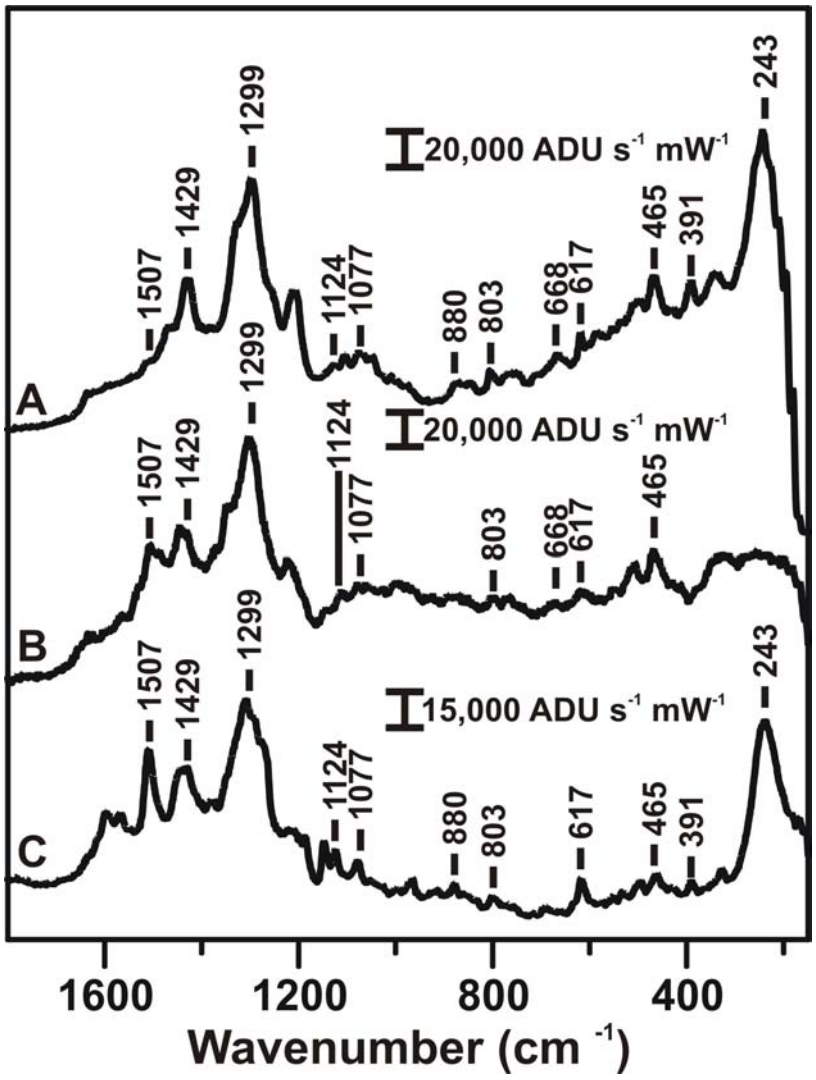

Figure 6.3 Pre-resonance SERS spectra of (A) 15 ng/μL cochineal (Penick & Co.-1981) (30 sec acquisition), (B) 15 ng/μL cochineal (Cochineal Carmine lake (F. Weber)) (30 sec acquisition), and (C) $1x10^{-6}$ M carminic acid (45 sec acquisition). All samples were prepared on AgFONs fabricated with 390 nm diameter SiO_2 spheres and spectra was collected with $\lambda_{excitation}$ = 632.8 nm.

spectra is evident, confirming the effectiveness of the methodology to correctly identify the chromaphore, in this case carminic acid, in the artists' pigment cochineal. Diagnostic peaks were selected and are labeled in the spectra in Figure 6.3. Again, spectra from each sample were collected in five separate areas with consistent results each time. Additionally, to the best of the authors knowledge, the pre-resonance SER spectra of cochineal presented in this work are the highest resolution to date.[30,78]

6.3.2 SERS Substrate Optimization

The sample size available in museums is often extremely small and therefore it is important to optimize the experimental parameters in order to find the most sensitive detection system. The work discussed here takes advantage of two Raman enhancing effects: (1) resonance Raman and (2) SERS. Experiments were conducted with two of the investigated red dyes (carminic acid and lac dye) to evaluate the contributions of both resonance Raman and SERS. Figure 6.4 depicts UV-Vis absorption spectra of alizarin (Fig 6.4A), carminic acid (Fig 6.4B-1) and cochineal (Fig 6.4B-2), lac dye (Fig 6.4C), and Purpurin (Fig 6.4D). Because each of these dyes absorb in the visible region, resonance Raman and pre-resonance Raman enhancements should occur when using 532.17 nm and 632.8 nm excitation wavelengths, respectively. The maximum SERS intensity is obtained from a AgFON surface when the laser excitation wavelength is slightly blue with respect to the LSPR maxiumum.[75] Therefore, by matching AgFON LSPR maxima with similar laser excitation wavelengths optimum SERS enhancement conditions will be met. Figure 5 depicts UV-Vis reflectance spectra of AgFONs fabricated with 300 nm (Fig. 6.5A), 390 nm (Fig. 6.5B), and 550 nm (Fig. 6.5C) diameter SiO_2 spheres with LSPR maxima located at 561 nm, 644 nm, and 747 nm respectively. Collecting spectra of the two dyes using 532.17 nm and 632.8 nm lasers on AgFONs with correlating LSPR

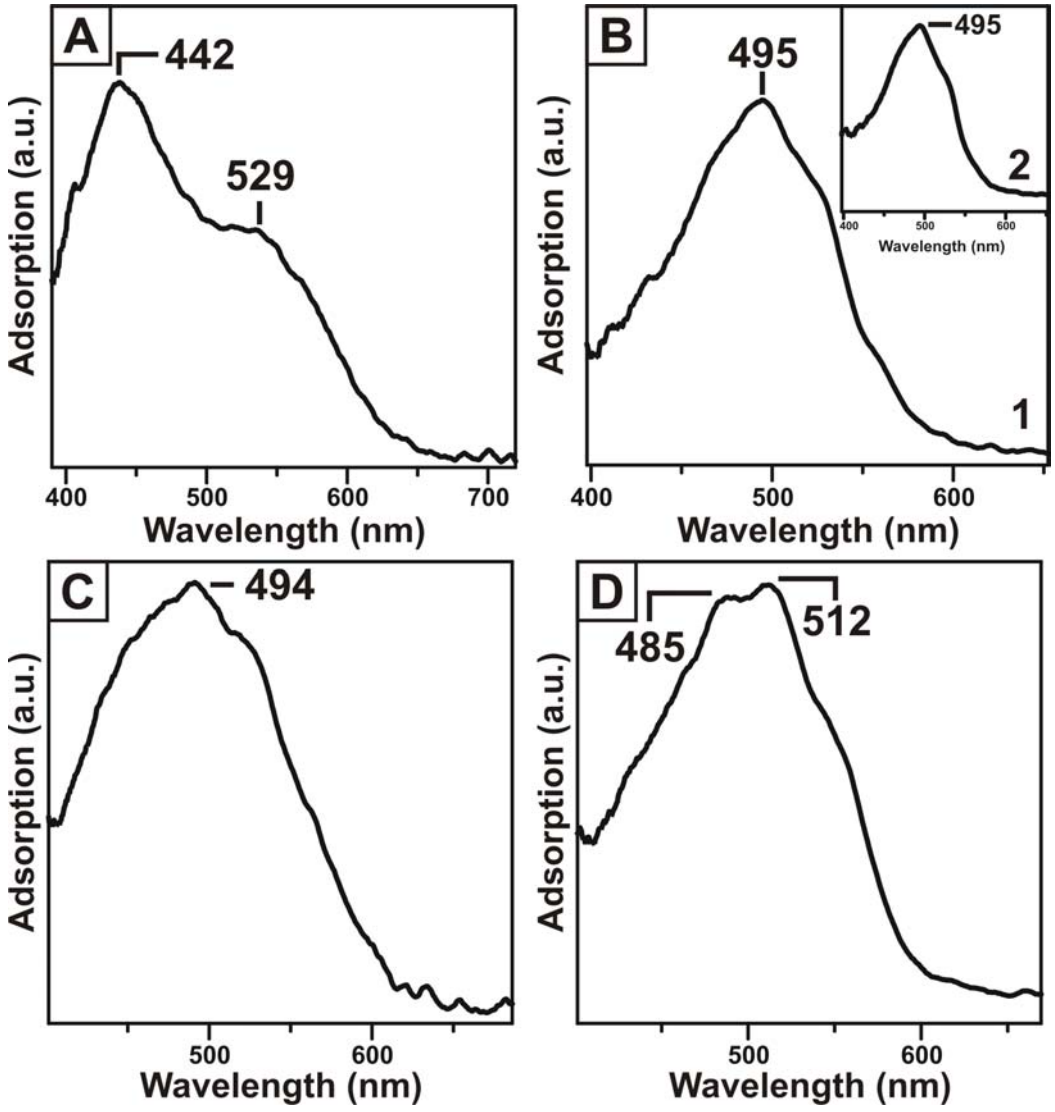

Figure 6. 4 UV-Vis spectra of (A)1 x 10^{-5} M alizarin, (B) (1) 150 ng/μL cochineal and (2) 1 x 10^{-5} M carminic acid, (C) 150 ng/μL lac dye, and (D) 1 x 10^{-5} M purpurin.

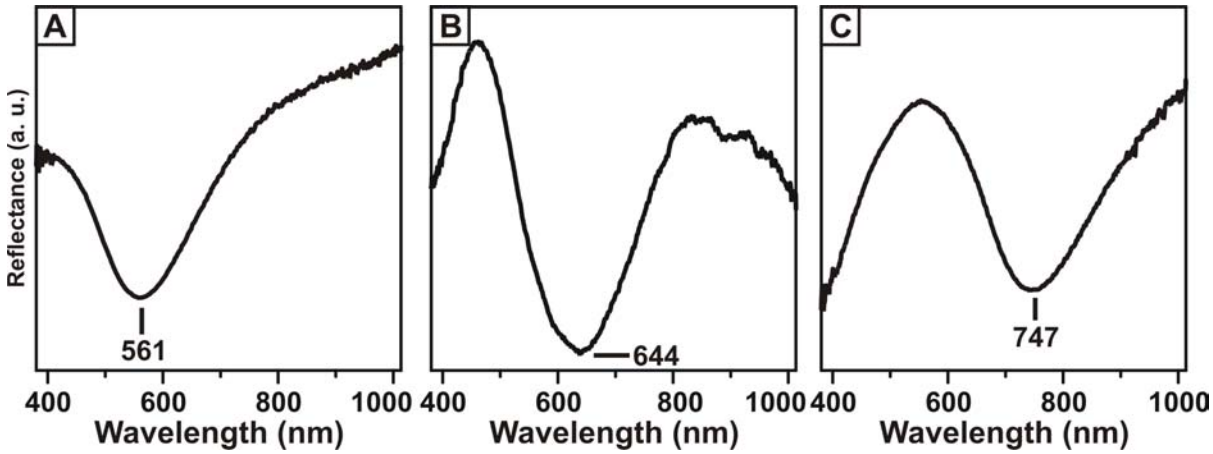

Figure 6.5 UV-Vis Reflectance spectra of AgFONs made with (A) 300 nm, (B) 390 nm, and (C) 550 nm diameter SiO_2 spheres.

maxima will result in both resonance and SER enhancements simultaneously. Alternatively, using a 785.7 nm laser with a AgFON with a similar LSPR maxima will only result in SERS. By comparing the resonance SERS spectra collected with the 532.17 nm and 632.8 nm lasers to the non-resonant SERS spectra collected with the 785.8 nm laser, the individual contributions due to resonance Raman and SERS can be determined.

Figure 6.6 depicts non-resonant SER (6.6A-1 and 6.6B-1), pre-resonant SER (6.6A-2 and 6.6B-2), and resonant SERS (6.6A-3 and 6.6B-3) spectra of carminic acid (Fig. 6.6A) and lac dye (Fig. 6.6B). All the spectra collected with the three laser excitation wavelengths (532.17, 632.8, and 785.7 nm) of carminic acid contained the diagnostic peaks that were previously shown (Fig. 6.3C). Similar results were observed for the spectra collected of lac dye. In the case of both carminic acid and lac dye, spectra collected with the 785.7 nm laser were ~ 30-125 orders of magnitude less intense than the spectra collected with the 532.15 nm and 632.8 nm lasers. These results can be attributed to the fact that resonance conditions were not met. One result of working on resonance is the amplification of specific vibrational bands. Examples of this can be seen in the 1429 cm^{-1} peak in the carminic acid spectra and the 1201 cm^{-1} peak in the lac dye spectra. Both the 1429 cm^{-1} (carminic acid) and the 1201 cm^{-1} (lac dye) peaks are weak in the spectra collected with the 785.7 nm laser while they are significantly enhanced in the spectra collected with both the 632.8 nm and 532.15 nm lasers. These experiments show that by working in the resonance and pre-resonance regions of these red dyes, significant enhancement of SERS spectra will be achieved.

6.3.3 Identification of Individual Dyes in Mixtures

Artists often mix several types of pigments or dyes together; therefore, samples that are collected from most artwork contain a mixture of compounds. Consequently, it is important to

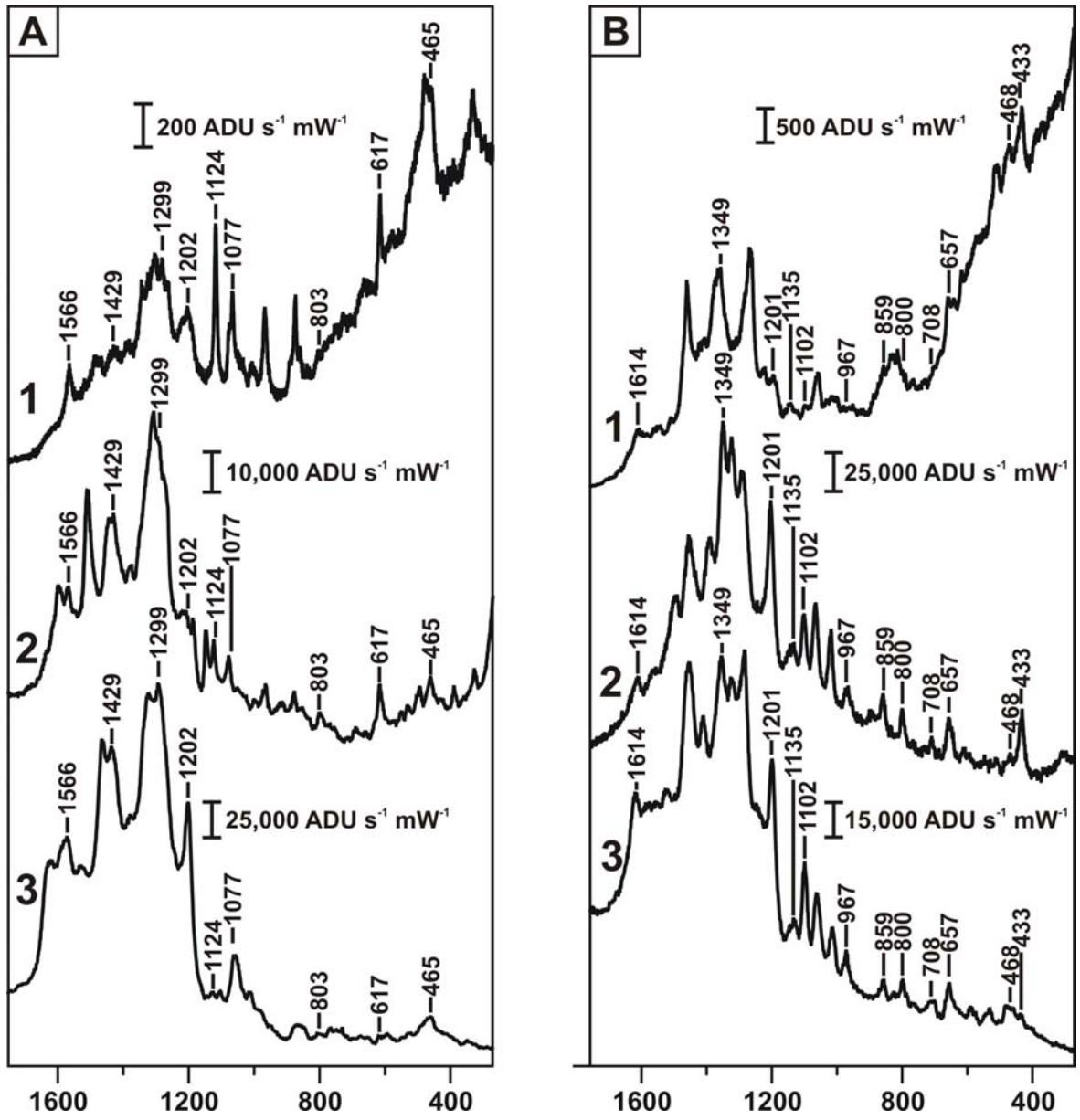

Figure 6.6 Pre-resonance, resonance, and non-resonance SER spectra of (A) carminic acid and (B) lac dye with collected various excitation wavelengths paired with SiO_2 AgFONs with similar LSPR values. (A1 and B1) $\lambda_{excitation}$ = 785.7 nm, AgFONs fabricated with 550 nm diameter SiO_2 spheres, 15 sec acquisition. (A2 and B2) $\lambda_{excitation}$ = 632.8 nm, AgFONs fabricated with 390 nm diameter SiO_2 spheres, 15 sec acquisition. (A3 and B3) $\lambda_{excitation}$ = 532.15 nm paired, AgFONs fabricated with 300 nm diameter SiO_2 spheres, 15 sec acquisition.

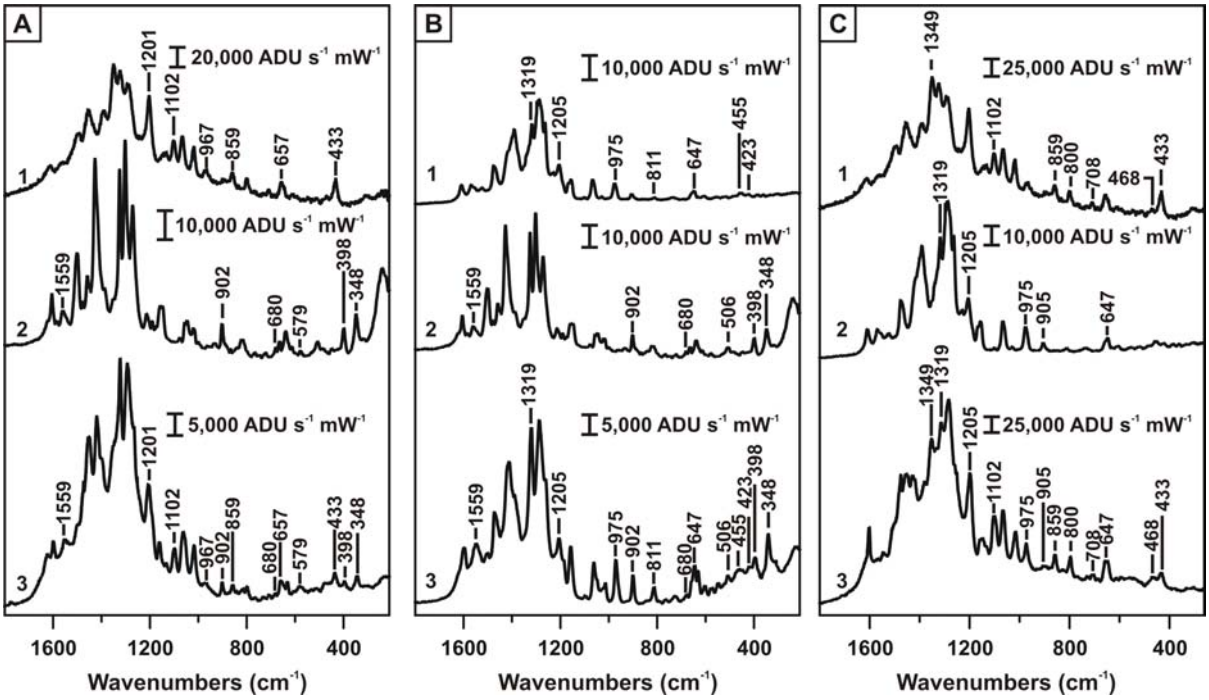

Figure 6.7 Pre-resonance SER spectra of (A) (1) 15 ng/μL lac dye (15 sec acquisition), (2) $1x10^{-6}$ M alizarin (60 sec acquisition), and (3) a mixture of 15 ng/μL lac dye and $1x10^{-6}$ M alizarin (60 sec acquisition), (B) (1) $1x10^{-6}$ M purpurin (15 sec acquisition), (2) $1x10^{-6}$ M alizarin (60 sec acquisition), and (3) a mixture of $1x10^{-6}$ M purpurin and $1x10^{-6}$ M alizarin (20 sec acquisition), and (C) (1) 15 ng/μL lac dye (15 sec acquisition), (2) $1x10^{-6}$ M purpurin (15 sec acquisition), and (3) a mixture of 15 ng/μL lac dye and $1x10^{-6}$ M purpurin (20 sec acquisition). (632.8 nm excitation, 390 nm diameter SiO_2 AgFONs).

be able to identify multiple dyes simultaneously in a single sample. Solutions were prepared containing low concentrations (1 x 10^{-6} M or 15 ng/μL) of two dyes, as would be found after extraction from historic textiles or artists' paint layers. Pre-resonance SER spectra were then collected with the 632.8 nm laser from SiO_2 AgFONs fabricated with 390 nm diameter spheres that had been incubated in these dye mixtures overnight. Figure 6.7 depicts pre-resonance SER spectra of dye mixtures containing alizarin and lac dye (6.7A-3), alizarin and purpurin (6.7B-3), and lac dye and purpurin (6.7C-3). For the purpose of comparison, spectra of the mixtures are paired with reference spectra of the individual dyes: alizarin (6.7A-2 and 6.7B-2), lac dye (6.7A-1 and 6.7C-1), and purpurin (6.7B-1 and 6.7C-2). The spectra collected from all of the dye mixtures contain diagnostic peaks from both of the individual red lake dyes and can therefore be identified as a mixture of the two dyes. The mixture containing alizarin and lac dye (Fig. 6.7A-3) contains peaks located at 433, 657, 859, 967,1102, and 1201 cm^{-1} which can be attributed to lac dye (Fig. 6.7A-1) and peaks located at 348, 398, 579, 680, 902 and 1559 cm^{-1} which can be attributed to alizarin (Fig.6.7A-2). The mixture made from purpurin and alizarin (Fig. 6.7B-3) contains peaks from both the individual purpurin (423, 455, 647, 811, 975, 1205, and 1319 cm^{-1}) and alizarin (348, 398, 506, 680, 902 and 1559 cm^{-1}). Finally, the mixture composed of lac dye and purpurin (Fig. 6.7C-3) contains peaks due to both lac dye (433, 468, 708, 800, 859, 1102, and 1349 cm^{-1}) and purpurin (647, 905, 975, 1205 and 1319 cm^{-1}). These experiments show that AgFONs exhibit great potential to be employed as SERS substrates to identify and characterize artwork samples containing mixtures of pigments and dyes.

6.4 Conclusions

This work demonstrates that AgFONs are an effective SERS substrate for the identification and characterization of red dyes and their mixtures. AgFONs are easily fabricated and are capable of collecting high resolution and consistent spectra. Because museum sample sizes are often extremely small, all SERS experiments were conducted with sample sizes similar to those found in museums (1×10^{-6} M or 15 ng/μL). Detailed and reproducible pre-resonance SER spectra were collected for the dyestuffs alizarin, purpurin, lac dye, carminic acid, and cochineal. Furthermore, to the best of the authors' knowledge, the pre-resonance SER spectra collected for cochineal are the highest resolution to date. Experiments were conducted with various laser excitation wavelengths (532.15 nm, 632.8 nm, and 785.7 nm) matched with correlating AgFON LSPR maxima (561 nm, 644 nm, and 747 nm) in order to determine the most sensitive detection system to study the red dyes. Because these red dyes adsorb visible light, resonance and pre-resonance Raman conditions could be met using the 532.15 nm and 632.8 nm lasers, respectively, resulting in further enhancement. Alternatively, using a 785.7 nm laser will only result in SERS. By comparing the spectra, it was determined that resonance effects will enhance SERS spectra of approximately 30-125 orders of magnitude. Finally, samples collected from artwork often contain dye mixtures. Therefore, experiments were successfully preformed to simultaneously identify individual dyes contained in mixtures of (1) alizarin and lac dye, (2) alizarin and purpurin, and (3) purpurin and lac dye. These initial experiments show promise towards utilizing AgFONs as SERS substrates to correctly identify individual dyes in mixed samples in real artwork.

References

1. Haes, A. J.; Haynes, C. L.; McFarland, A. D.; Schatz, G. C.; Van Duyne, R. P.; Zou, S., *MRS Bulletin* **2005,** 30, (5), 368.

2. Haes Amanda, J.; Van Duyne Richard, P., *Journal of the American Chemical Society* **2002,** 124, (35), 10596.

3. Riboh, J. C.; Haes, A. J.; McFarland, A. D.; Yonzon, C. R.; Van Duyne, R. P., *Journal of Physical Chemistry B* **2003,** 107, (8), 1772.

4. Haes, A. J.; Chang, L.; Klein, W. L.; Van Duyne, R. P., *Journal of the American Chemical Society* **2005,** 127, (7), 2264.

5. Yonzon, C. R.; Jeoung, E.; Zou, S.; Schatz, G. C.; Mrksich, M.; Van Duyne, R. P., *Journal of the American Chemical Society* **2004,** 126, (39), 12669.

6. Willets, K. A.; Van Duyne Richard, P., *Ann. Rev. Phys. Chem.* **2007,** 58, 267.

7. Haes, A. J.; Van Duyne, R. P., *Materials Research Society Symposium Proceedings* **2004,** 789, (Quantum Dots, Nanoparticles and Nanowires), 409.

8. Haynes, C. L.; Van Duyne, R. P., *J. Phys. Chem. B* **2001,** 105, (24), 5599.

9. Whitney, A. V.; Elam, J. W.; Zou, S.; Zinovev, A. V.; Stair, P. C.; Schatz, G. C.; Van Duyne, R. P., *J. Phys. Chem. B* **2005,** 109, (43), 20522.

10. Haes, A. J.; Zou, S.; Zhao, J.; Schatz, G. C.; Van Duyne, R. P., *J. Am. Chem. Soc.* **2006,** 128, (33), 10905.

11. Sherry, L. J.; Chang, S.-H.; Schatz, G. C.; Van Duyne, R. P.; Wiley, B. J.; Xia, Y., *Nano Letters* **2005,** 5, (10), 2034.

12. Sherry, L. J.; Jin, R.; Mirkin, C. A.; Schatz, G. C.; Van Duyne, R. P., *Nano Letters* **2006,** 6, (9), 2060.

13. Zhao, J.; Zhang, X.; Haes, A. J.; Zou, S.; Schatz, G. C.; Van Duyne, R. P., *Proceedings of SPIE-The International Society for Optical Engineering* **2006,** 6323, (Plasmonics: Metallic Nanostructures and Their Optical Properties IV), 63231B/1.

14. Haes, A. J.; Zou, S.; Schatz, G. C.; Van Duyne, R. P., *Journal of Physical Chemistry B* **2004,** 108, (1), 109.

15. Ott, A. W.; Klaus, J. W.; Johnson, J. M.; George, S. M., *Thin Solid Films* **1997,** 292, (1-2), 135.

16. Groner, M. D.; Fabreguette, F. H.; Elam, J. W.; George, S. M., *Chem. Mater* **2004,** 16, (4), 639.

17. Raman, C. V.; Krishnan, K. S., *Nature (London, United Kingdom)* **1928,** 121, 501.

18. Jeanmaire, D. L.; Van Duyne, R. P., *Journal of Electroanalytical Chemistry and Interfacial Electrochemistry* **1977,** 84, (1), 1.

19. Haynes, C. L.; Van Duyne, R. P., *Journal of Physical Chemistry B* **2003,** 107, (30), 7426.

20. Haynes, C. L.; Yonzon, C. R.; Zhang, X.; Van Duyne, R. P., *J. Raman Spectrosc.* **2005,** 36, (6/7), 471.

21. Lyandres, O.; Shah, N. C.; Yonzon, C. R.; Walsh, J. T., Jr.; Glucksberg, M. R.; Van Duyne, R. P., *Anal. Chem.* **2005,** 77, (19), 6134.

22. Shafer-Peltier Karen, E.; Haynes Christy, L.; Glucksberg Matthew, R.; Van Duyne Richard, P., *J. Am. Chem. Soc.* **2003,** 125, (2), 588

23. Stuart, D. A.; Yonzon, C. R.; Zhang, X.; Lyandres, O.; Shah, N. C.; Glucksberg, M. R.; Walsh, J. T.; Van Duyne, R. P., *Anal. Chem.* **2005,** 77, (13), 4013.

24. Yonzon, C. R.; Haynes, C. L.; Zhang, X.; Walsh, J. T., Jr.; Van Duyne, R. P., *Anal. Chem.* **2004,** 76, (1), 78.

25. Zhang, X.; Shah, N. C.; Van Duyne, R. P., *Vib. Spectrosc.* **2006,** 42, (1), 2.

26. Stuart Douglas, A.; Biggs Kevin, B.; Van Duyne Richard, P., *Analyst FIELD Full Journal Title:The Analyst* **2006,** 131, (4), 568.

27. Zhang, X.; Young, M. A.; Lyandres, O.; Van Duyne, R. P., *J. Am. Chem. Soc.* **2005,** 127, (12), 4484.

28. Zhang, X.; Zhao, J.; Whitney, A. V.; Elam, J. W.; Van Duyne, R. P., *J. Am. Chem. Soc.* **2006,** 128, (31), 10304.

29. Whitney, A. V.; Van Duyne, R. P.; Casadio, F., *Proceedings of SPIE-The International Society for Optical Engineering* **2005,** 5993, (Advanced Environmental, Chemical, and Biological Sensing Technologies III), 59930K/1.

30. Whitney, A. V.; Van Duyne, R. P.; Casadio, F., *J. Raman Spectrosc.* **2006,** 37, (10), 993.

31. Stuart, D. A.; Yuen, J. M.; Shah, N.; Lyandres, O.; Yonzon, C. R.; Glucksberg, M. R.; Walsh, J. T.; Van Duyne, R. P., *Anal. Chem.* **2006,** 78, (20), 7211.

32. Grunes, J.; Zhu, J.; Anderson, E. A.; Somorjai, G. A., *Journal of Physical Chemistry B* **2002,** 106, (44), 11463.

33. Bronstein, L. M., *Topics in Current Chemistry* **2003,** 226, (Colloid Chemistry I), 55.

34. Pantano, P.; Walt, D. R., *Chemical Materials* **1996,** 8, 2832.

35. Tong, H. D.; Jansen, H. V.; Gadgil, V. J.; Bostan, C. G.; Berenschot, E.; van Rijn, C. J. M.; Elwenspoek, M., *Nano Letters* **2004,** 4, (2), 283.

36. Han, J.; Craighead, H. G., *Science (Washington, D. C.)* **2000,** 288, (5468), 1026.

37. Siwy, Z.; Fulinski, A., *Physical Review Letters* **2002,** 89, (19), 198103/1.

38. Lee, S. B.; Martin, C. R., *Analytical Chemistry* **2001,** 73, (4), 768.

39. Gasparac, R.; Mitchell, D. T.; Martin, C. R., *Electrochimica Acta* **2004,** 49, (6), 847.

40. Howorka, S.; Cheley, S.; Bayley, H., *Nature Biotechnology* **2001,** 19, (7), 636.

41. Landskron, K.; Hatton, B. D.; Perovic, D. D.; Ozin, G. A., *Science* **2003,** 302, 266.

42. Haynes, C. L.; McFarland, A. D.; Zhao, L. L.; Van Duyne, R. P.; Schatz, G. C.; Gunnarsson, L.; Prikulis, J.; Kasemo, B.; Kall, M., *Journal of Physical Chemistry B* **2003,** 107, (30), 7337.

43. Martin, O. J. F., *Microelectronic Engineering* **2003,** 67-68, 24.

44. Smith, B. W.; Bourov, A.; Kang, H.; Cropanese, F.; Fan, Y.; Lafferty, N.; Zavyalova, L., *Journal of Microlithography, Microfabrication, and Microsystems* **2004,** 3, (1), 44.

45. Hulteen, J. C.; Martin, C. R., *Journal of Materials Chemistry* **1997,** 7, (7), 1075.

46. Hulteen, J. C.; Duyne, R. P. V., *Journal of Vacuum Science Technology A* **1995,** 13, (3), 1553.

47. Haynes, C. L.; Duyne, R. P. V., *Journal of Physical Chemistry B* **2001,** 105, 5599.

48. Haynes, C. L.; McFarland, A. D.; Smith, M. T.; Hulteen, J. C.; Duyne, R. P. V., *Journal of Physical Chemistry B* **2002,** 106, 1898.

49. Haynes, C. L.; Van Duyne, R. P., *Nano Letters* **2003,** 3, (7), 939.

50. Jenson, T. R.; Duval, M. L.; Kelly, K. L.; Lazarides, A. A.; Schatz, G. C.; Duyne, R. P. V., *Journal of Physical Chemistry B* **1999,** 103, 9846.

51. Madou, M. J., *Fundamentals of Microfabrication The Science of Miniaturization*. 2 ed.; CRC Press: 2002; p 723.

52. Hulteen, J. C.; Treichel, D. A.; Smith, M. T.; Duval, M. L.; Jenson, T. R.; Duyne, R. P. V., *Journal of Physical Chemistry B* **1999,** 103, 3854.

53. Jung, L. S.; Campbell, C. T.; Chinowsky, T. M.; Mar, M. N.; Yee, S. S., *Langmuir* **1998,** 14, 5636.

54. Malinsky, M. D.; Kelly, K. L.; Schatz, G. C.; Van Duyne, R. P., *Journal of the American Chemical Society* **2001,** 123, (7), 1471.

55. Haes, A. J.; Zou, S.; Schatz, G. C.; Van Duyne, R. P., *Journal of Physical Chemistry B* **2004,** 108, (22), 6961.

56. Ritala, M.; Leskela, M., *Handbook of Thin Film Materials* **2002,** 1, 103.

57. Jensen, T. R.; Duval, M. L.; Kelly, K. L.; Lazarides, A. A.; Schatz, G. C.; Van Duyne, R. P., *J. Phys. Chem. B* **1999,** 103, (45), 9846.

58. Elam, J. W.; Groner, M. D.; George, S. M., *Rev. Sci. Instrum.* **2002,** 73, (8), 2981.

59. Rocklein, M. N.; George, S. M., *Analytical Chemistry* **2003,** 75, (19), 4975.

60. Matero, R.; Rahtu, A.; Ritala, M.; Leskela, M.; Sajavaara, T., *Thin Solid Films* **2000,** 368, (1), 1.

61. Moulder, J. F.; Stickle, W. F.; Sobol, P. E.; Boman, K. D., *Handbook of X-ray Photoelectron Spectroscopy* **1992**.

62. Groner, M. D.; Elam, J. W.; Fabreguette, F. H.; George, S. M., *Thin Solid Films* **2002,** 413, (1-2), 186.

63. Zhou, X. L.; White, J. M., *Surface Science* **1992,** 273, (3), 322.

64. Rahtu, A.; Alaranta, T.; Ritala, M., *Langmuir* **2001,** 17, (21), 6506.

65. Draine, B. T.; Flatau, P. J., *J. Opt. Soc. Am. A* **1994,** 11, 1491.

66. Draine, B. T.; Flatau, P. J., *User Guid for the Discrete Dipole Approximation Code DDSCAT. 6.0* **2003**, http://arxiv.org/abs/astro.

67. Kelly, K. L.; Coronado, E.; Zhao, L. L.; Schatz, G. C., *Journal of Physical Chemistry B* **2003,** 107, (3), 668.

68. Zou, S.; Zhao, L.; Schatz, G. C., *Proceedings of SPIE-The International Society for Optical Engineering* **2003,** 5221, (Plasmonics: Metallic Nanostructures and Their Optical Properties), 174.

69. Lynch, D. W.; Hunter, W. R.; Palik, E. D., *Handbook of Optical Constants of Solids*. Academic Press: New York, 1985.

70. Somorjai, G. A.; Rupprechter, G., *J. Phys. Chem. B* **1999,** 103, (10), 1623.

71. Stair, P. C., *Current Opinion in Solid State & Materials Science* **2001,** 5, (5), 365.

72. Banares, M. A., *Catalysis Today* **2005,** 100, (1-2), 71.

73. Guerrero-Perez, M. O.; Banares, M. A., *Catalysis Today* **2006,** 113, (1-2), 48.

74. Dieringer, J. A.; McFarland, A. D.; Shah, N. C.; Stuart, D. A.; Whitney, A. V.; Yonzon, C. R.; Young, M. A.; Zhang, X.; Van Duyne, R. P., *Faraday Discussions* **2006,** 132, (Surface Enhanced Raman Spectroscopy), 9.

75. McFarland, A. D.; Young, M. A.; Dieringer, J. A.; Van Duyne, R. P., *J. Phys. Chem. B* **2005,** 109, (22), 11279.

76. Jensen, T. R.; Malinsky, M. D.; Haynes, C. L.; Van Duyne, R. P., *J. Phys. Chem. B* **2000,** 104, (45), 10549.

77. Guineau, B., *Stud. Conserv.* **1984,** 29, (1), 35.

78. Bell, I. M.; Clark, R. J. H.; Gibbs, P. J., *Spectrochim. Acta, Part A.* **1997,** 53A, (12), 2159.

79. Burgio, L.; Clark, R. J. H., *Spectrochim. Acta, Part A.* **2001,** 57A, (7), 1491.

80. Smith, G. D.; Clark, R. J. H., *Rev. Conserv.* **2002,** 2, 92.

81. Vandenabeele, P.; Moens, L.; Edwards, H. G. M.; Dams, R., *J. Raman Spectrosc.* **2000,** 31, (6), 509.

82. Bussotti, L.; Castellucci, E.; Matteini, M., *Science Tech. Cult. Heritage* **1996,** 5, 13.

83. de Oliveira, L. F. C.; Edwards, H. G. M.; Velozo, E. S.; Nesbitt, M., *Vib. Spectrosc.* **2002,** 28, (2), 243.

84. Edwards, H. G. M.; de Oliveira, L. F. C.; Nesbitt, M., *Analyst (Cambridge, United Kingdom)* **2003,** 128, (1), 82.

85. Canamares, M. V.; Garcia-Ramos, J. V.; Domingo, C.; Sanchez-Cortes, S., *J. Raman Spectrosc.* **2004,** 35, (11), 921.

86. Shadi, I. T.; Chowdhry, B. Z.; Snowden, M. J.; Withnall, R., *J. Raman Spectrosc.* **2004,** 35, (8/9), 800.

87. Leona, M., *Proceedings of the 6th Infrared and Raman Users Group Conference*. Florence, Italy, 2006; p 105.

88. Guineau, B.; Guichard, V., *ICOM committe for conservation: 8th triennial meeting, Sydney, Australia, 6-11 September, 1987. Preprints.* The Getty Conservation Institute: Marina del Rey, 1987; Vol. 2, p 659.

89. Zhang, X.; Young Matthew, A.; Lyandres, O.; Van Duyne Richard, P., *J. Am. Chem. Soc.* **2005,** 127, (12), 4484.

90. Van Duyne, R. P.; Hulteen, J. C.; Treichel, D. A., *J. Chem. Phys.* **1993,** 99, (3), 2101.

91. Shafer-Peltier, K. E.; Haynes, C. L.; Glucksberg, M. R.; Van Duyne, R. P., *J. Am. Chem. Soc.* **2003,** 125, (2), 588.

92. Kirby, J.; White, R., *National Gallery Technical Bulletin* **1996,** 17, 56.

93. Schweppe, H.; Roosen-Runge, H., *Artists' Pigments. A handbook of their history and characteristics*. Oxford University Press: New York, 1996; Vol. 1, p 255.

94. Gary, C. W.; Omecinsky, D., *JAIC* **1983,** 22, 68.

95. Hofenk de Graaff, J. H., *The Colorful Past; Origins, Chemistry and Identification of natural dyestuffs*. Abegg-Stiftung and Archetype Publications Ltd.: Riggisberg, Switzerland and London, UK, 2004; p 40.

96. M. J. Frisch, G. W. T., H. B. Schlegel, G. E. Scuseria, M. A. Robb, J. R. Cheeseman, J. A. Montgomery, Jr., T. Vreven, K. N. Kudin, J. C. Burant, J. M. Millam, S. S. Iyengar, J. Tomasi, V. Barone, B. Mennucci, M. Cossi, G. Scalmani, N. Rega, G. A. Petersson, H. Nakatsuji, M. Hada, M. Ehara, K. Toyota, R. Fukuda, J. Hasegawa, M. Ishida, T. Nakajima, Y. Honda, O. Kitao, H. Nakai, M. Klene, X. Li, J. E. Knox, H. P. Hratchian, J. B. Cross, V. Bakken, C. Adamo, J. Jaramillo, R. Gomperts, R. E. Stratmann, O. Yazyev, A. J. Austin, R. Cammi, C. Pomelli, J. W. Ochterski, P. Y. Ayala, K. Morokuma, G. A. Voth, P. Salvador, J. J. Dannenberg, V. G. Zakrzewski, S. Dapprich, A. D. Daniels, M. C. Strain, O. Farkas, D. K. Malick, A. D. Rabuck, K. Raghavachari, J. B. Foresman, J. V. Ortiz, Q. Cui, A. G. Baboul, S. Clifford, J. Cioslowski, B. B. Stefanov, G. Liu, A. Liashenko, P. Piskorz, I. Komaromi, R. L. Martin, D. J. Fox, T. Keith, M. A. Al-Laham, C. Y. Peng, A. Nanayakkara, M. Challacombe, P. M. W. Gill, B. Johnson, W. Chen, M.

W. Wong, C. Gonzalez, and J. A. Pople, *Gaussian 03, Revision C.02*, Gaussian, Inc.: Wallingford CT, 2004.

97. Clark, R. J.; Huxley, *Science Tech. Cult. Heritage* **1996**, 98.

98. Canamares, M. V.; Garcia-Ramos, J. V.; Domingo, C.; Sanchez-Cortes, S., *Vib. Spectrosc.* **2006,** 40, (2), 161.

99. Chen, K.; Leona, M.; Vo-Dinh, K.-C.; Yan, F.; Wabuyele, M. B.; Vo-Dinh, T., *J. Raman Spectrosc.* **2006,** 37, (4), 520.

100. Leona, M.; Stenger, J.; Ferloni, E., *J. Raman Spectrosc.* **2006,** 37, (10), 981.

101. Murcia-Mascaros, S.; Domingo, C.; Sanchez-Cortes, S.; Canamares, M. V.; Garcia-Ramos, J. V., *J. Raman Spectrosc.* **2005,** 36, (5), 420.

102. Chen, K.; Leona, M.; Vo-Dinh, K. C.; Yan, F.; Wabuyele, M.; Vo-Dinh, T., *Proceedings of SPIE-The International Society for Optical Engineering* **2005,** 5993, (Advanced Environmental, Chemical, and Biological Sensing Technologies III), 59930M/1.

103. Jensen, T. R.; Van Duyne, R. P.; Johnson, S. A.; Maroni, V. A., *Applied Spectroscopy* **2000,** 54, (3), 371.

104. Litorja, M.; Haynes, C. L.; Haes, A. J.; Jensen, T. R.; Van Duyne, R. P., *J. Phys. Chem. B* **2001,** 105, (29), 6907.

105. Kirby, J. In *Reconstruction of French 19th Century red lake pigments used at the time of Vincent van Gogh*, Approaching the Art of the Past: Sources and Reconstructions, Amsterdam, 2005; Clark, M.; Townsend, J. H.; Stijnman, A., Eds. Archetype Publications: Amsterdam, 2005; pp 69.

106. Asher, S. A., *Annual Review of Physical Chemistry* **1988,** 39, 537.

107. Hudson, B.; Kelly, P. B.; Ziegler, L. D.; Desiderio, R. A.; Gerrity, D. P.; Hess, W.; Bates, R., *Advances in Laser Spectroscopy* **1986,** 3, 1.

108. Groner, M. D.; Fabreguette, F. H.; Elam, J. W.; George, S. M., *Chem. Mater.* **2004,** 16, 639.

109. Schatz, G. C.; Van Duyne, R. P., Electromagnetic Mechanism of Surface-Enhanced Spectroscopy. In *Handbook of Vibrational Spectroscopy*, Chalmers, J. M.; Griffiths, P. R., Eds. Wiley: New York, 2002; Vol. 1, pp 759

110. Dick, L. A.; Haes, A. J.; Van Duyne, R. P., *Journal of Physical Chemistry B* **2000,** 104, 11752

111. Kennedy, B. J.; Spaeth, S.; Dickey, M.; Carron, K. T., *Journal of Physical Chemistry B* **1999,** 103, 3640.

Appendix 1

Surface-Enhanced Raman Spectroscopy (SERS) Distance Dependence

A1.1 Experimental

A1.1.1 Atomic Layer Deposition (ALD)

Al_2O_3 films were fabricated on nanosphere lithography (NSL) Ag nanoparticles by atomic layer deposition (ALD). The reactor utilized in these experiments is similar to that described in previous publications.[58] TMA and deionized H_2O vapors were alternately pulsed through the reaction chamber utilizing N_2 as the carrier gas at a mass flow rate of 360 sccm and a pressure of 1 Torr using a growth temperature of 50 ºC. Al_2O_3 ALD proceeds on a hydroxylated surface according to the pair of self-limiting reactions shown in scheme 1.[108]

Scheme 1.

$$Al\text{-}OH^* + Al(CH_3)_3 \rightarrow Al\text{-}O\text{-}Al(CH_3)_2^* + CH_4$$

$$Al\text{-}CH_3^* + H_2O \rightarrow Al\text{-}OH^* + CH_4$$

The asterisks (*) signify the surface species. One complete AB cycle is 42 s: (1) TMA reactant exposure time = 1 s, (2) N_2 purge following TMA exposure time = 10 s, (3) H_2O reactant exposure time = 1 s, (4) N_2 purge following H_2O exposure time = 30 s. Long purge times are necessary at low temperatures to prevent chemical vapor deposition (CVD) of Al_2O_3.[108]

A1.1.2 Surface-Enhanced Raman Spectroscopy (SERS)

Experiments were performed to map the distance decay function of surface-enhanced Raman spectroscopy (SERS). Silver film over nanosphere (AgFON) samples were prepared by depositing 200 nm of silver over 390 nm polystyrene spheres from an electron beam evaporation source (Kurt J. Lesker AXXIS System). Alumina was then deposited by a custom fabricated ALD system at Argonne National Laboratory in thicknesses of 0.0 nm, 1.6 nm, 3.2 nm and 4.8 nm. The SERS spectrum of 50 mM pyridine in 100 mM NaCl/water was measured over the AgFON and ALD Al_2O_3 coated AgFON samples (λ_{ex} = 532 nm, P = 1.0 mW, acquisition time =

300 s). The excitation was performed in an epi configuration through a 20X objective (Nikon, NA = 0.5) on an inverted microscope (Nikon TE300). The SERS signal was collected through the same objective in 180 degree backscattering geometry.

A1.2 SERS Distance Dependence by ALD

The distance dependence of SERS is both a critical mechanistic and practical issue. The electromagnetic mechanism predicts that SERS is a long range effect that does not require the adsorbate to be in direct contact with the surface; but, does require it to be within a few nanometers of the surface.[109] In contrast, the chemical mechanism predicts that SERS is a short range effect that requires the adsorbate to be chemisorbed directly on the surface. From a practical perspective, there are certain experiments, such as those involving surface immobilized biological molecules,[110] where direct contact between the adsorbate of interest and the surface must be prevented for the experiment to succeed. In all of the SERS distance dependence studies published so far, randomly roughened surfaces (viz., island films, cold-deposited films in UHV, etc.) were used and the Raman active adsorbate is spaced from the surface using a polymer film, cold-condensed molecular layer, or self-assembled monolayer. Each of these spacer methods has its limitations. The ideal distance dependence experiment would be one in which the thickness of the spacer layer could be easily varied in thickness from a few angstroms to a hundred nanometers. Furthermore, the spacers would be conformal to handle roughened and nanostructured surfaces, pinhole free, and chemically uniform. ALD is just such a spacer fabrication method that produces highly uniform and controlled thin films.[9] Precursor gases are alternately pulsed through a reactor and purged away resulting in a self-limiting growth process

that constructs a film one monolayer at a time. Highly uniform monolayers of Al_2O_3 can be deposited with ~3.2 Å thickness resolution by ALD.

In this work we have deposited ALD Al_2O_3 multilayers onto AgFON surfaces to probe the distance dependence of SERS. In previous work, the distance dependence of SERS has been theoretically approximated as:

$$I = \left(1 + \frac{r}{a}\right)^{-10} \quad (1)$$

where I is the intensity of the Raman mode, a is the average size of the field enhancing features on the surface and r is the distance from the surface to the adsorbate.[111] Fig. A1.1 (B) shows the SER spectra for pyridine adsorbed on AgFON surfaces coated with three different thicknesses of ALD Al_2O_3. A plot of the relative intensity of the 1594 cm^{-1} band as a function of Al_2O_3 thickness is shown in Fig A1.1 (A). Fitting the experimental data to equation (1) leads to the average size of the enhancing particle (a) to be equal 12.0 nm. The term d_{10} defines the surface to molecule distance required to decrease the SERS intensity by a factor of ten. The data presented in this work clearly show that SERS is a long range effect with a d_{10} value for this particular surface nanostructure of 2.8 nm.

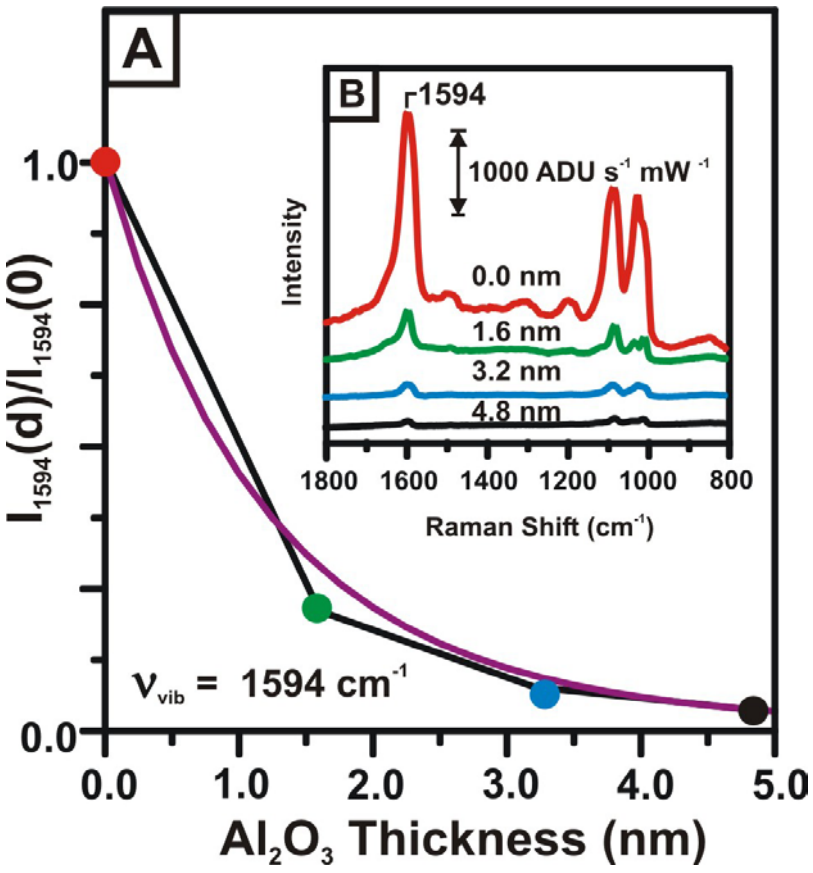

Figure A1.1 (A) Plot of SERS intensity as a function of Al_2O_3 thickness for the 1594 cm^{-1} band of pyridine. (B) SERS spectra from which the normalized SERS intensity is calculated.

APPENDIX 2

Thermal Stability of ALD Al_2O_3 Coated Ag Nanoparticles Under Various Gases

A2.1 Experimental

A2.1.1 Nanosphere Lithography

Nanosphere lithography (NSL) was used to fabricate monodispersed, surface-confined Ag nanoparticles.[57] Glass and Si (111) substrates were cleaned in a piranha etch solution (30% 3:1 H_2SO_4/H_2O_2) for 30 min at 80 ºC. After rinsing with water, the substrates were sonicated for 60 min in 5:1:1 $H_2O/H_2O_2/NH_4OH$ in order to create a hydrophilic surface on the substrate to facilitate self-assembly of the nanosphere masks. Finally, the substrates were rinsed and stored in water for future use. 2D self-assembled monolayer masks of nanospheres were fabricated by drop-coating approximately 2.5 μL of undiluted nanosphere solution (10% solid) on the pretreated substrates. The nanospheres were allowed to dry in ambient conditions. 50 nm of Ag was deposited by electron beam (e-beam) deposition in a Kurt J. Lesker Axxis e-beam deposition system (Pittsburg, PA) with a base pressure of 10^{-6} Torr. The mass thickness and deposition rate (1 Å/sec) was monitored using a Sigma Instruments 6 MHz gold plated QCM (Fort Collins, Colorado). After the Ag deposition, the nanosphere masks were removed by sonication in absolute ethanol for 3 min.

A2.1.2 Atomic Layer Deposition (ALD)

Al_2O_3 films were fabricated on NSL Ag nanoparticles by atomic layer deposition (ALD). The reactor utilized in these experiments is similar to that described in previous publications.[58] TMA and deionized H_2O vapors were alternately pulsed through the reaction chamber utilizing N_2 as the carrier gas at a mass flow rate of 360 sccm and a pressure of 1 Torr using a growth temperature of 50 ºC. Al_2O_3 ALD proceeds on a hydroxylated surface according to the pair of self-limiting reactions shown in scheme 1.[108]

Scheme 1.

$$Al\text{-}OH^* + Al(CH_3)_3 \rightarrow Al\text{-}O\text{-}Al(CH_3)_2^* + CH_4$$

$$Al\text{-}CH_3^* + H_2O \rightarrow Al\text{-}OH^* + CH_4$$

The asterisks (*) signify the surface species. One complete AB cycle is 42 s: (1) TMA reactant exposure time = 1 s, (2) N_2 purge following TMA exposure time = 10 s, (3) H_2O reactant exposure time = 1 s, (4) N_2 purge following H_2O exposure time = 30 s. Long purge times are necessary at low temperatures to prevent chemical vapor deposition (CVD) of Al_2O_3.[108]

A2.1.3 Thermal Annealing

Thermal studies were conducted inside the ALD reaction Chamber under 30 Torr of CO, O_2 or propane. All samples were heated at 400ºC for 30 minutes.

A2.1.4 UV-Vis Extinction Spectroscopy

LSPR extinction measurements of the Ag nanoparticle arrays were obtained using the M-2000V in transmission mode.

A2.1.5 Scanning Electron Microscopy (SEM)

Various Al_2O_3 film thicknesses on triangular Ag nanoparticles on Si (111) were observed with a Hitatchi S-4700-II SEM. Images were collected with 10.0 kV.

A2.2 Results and Discussion

A2.2.1 Thermal Annealing of ALD Al_2O_3 Coated Nanoparticles Under Various Gases

Thermally stable ALD Al_2O_3 coated NSL nanoparticles have the potential to be used to perform *in situ* SERS studies of reactions conducted at elevated temperatures; such as catalytic processes. Because the ALD Al_2O_3 coated nanoparticles would be exposed to reactive compounds, in such a reaction, it is important to determine their stability at high temperatures

under reactive materials. Figure A2.1 depicts UV-Vis spectra of ALD Al_2O_3 coated nanoparticles taken prior to and after heating at 400ºC for 30 minutes under 30 Torr (A) CO, (B) propane and, (C) O_2. Correlating SEM images (Figure A2.1E-G) were taken of the ALD Al_2O_3 coated nanoparticle substrates after heating. The ALD Al_2O_3 coated nanoparticles maintained their geometry better than uncoated particles (Chapter 4). Unfortunately, the ALD Al_2O_3 coated nanoparticles did not retain their shape as well as those that were heated under a less reactive gas such as N_2 (Chapter 4). The UV-Vis spectra collected after the nanoparticles were annealed under O_2 showed a significant decrease in intensity which may be attributed to oxidation of the Ag. Currently it is assumed that the reactive gases (CO, O_2, and propane) are either interacting with the Al_2O_3 coating or the Al_2O_3 Ag bonds. Either reaction would result in the breaking of Al_2O_3 Ag bonds, making the nanoparticles more susceptible to the high temperatures. As a result, more geometry changes would be observed than when heating the nanoparticles under a less reactive gas such as N_2.

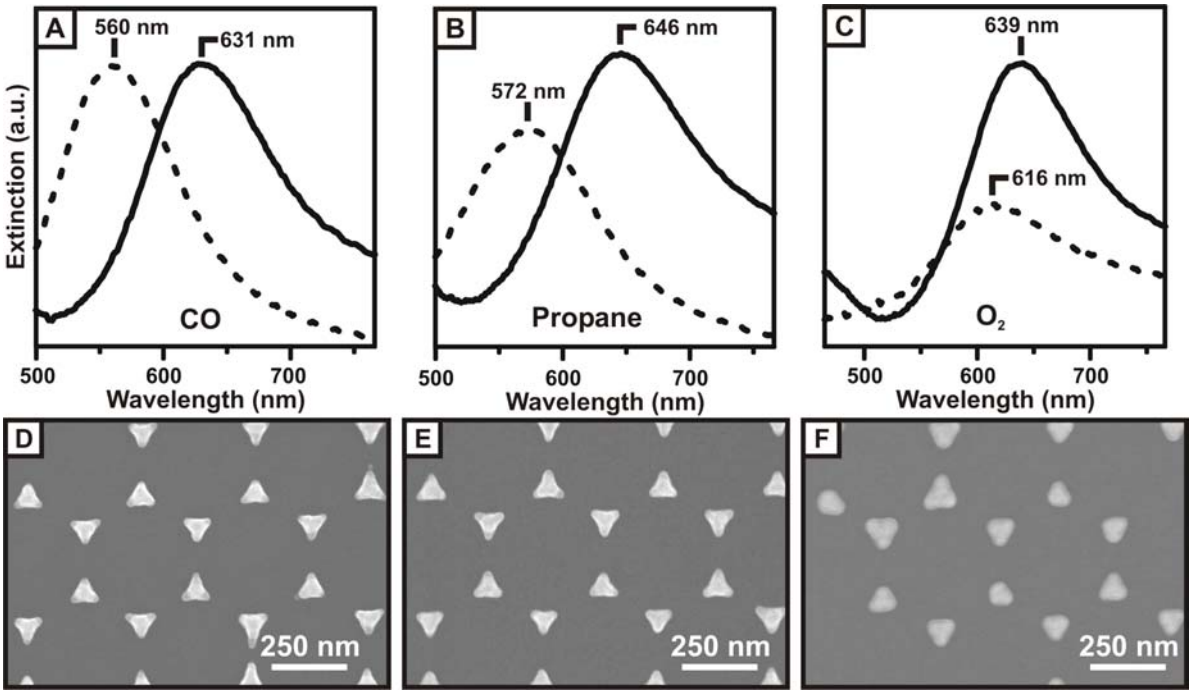

FIGURE A2.1 LSPR spectra of ALD Al_2O_3 coated nanoparticles heated at 400ºC under 30 Torr (A) CO, (B) propane, and (C) O_2. SEM images of ALD Al_2O_3 coated nanoparticles after heating under (E) CO, (F) propane, and (G) O_2. All samples were heated for 30 minutes. Solid lines indicate spectra taken prior to heating. Dashed lines indicate spectra taken after heating.

ALYSON V. WHITNEY

1406 Elmwood Ave. • Evanston, IL, 60201 • Phone (847) 287-0293 • a-whitney@northwestern.edu

SKILLS

- Microscopy: atomic force microscopy, scanning electron microscopy, transmission electron microscopy
- Spectroscopy: ultraviolet-visible, infrared, Raman, Mass Spec
- Chemical synthesis and optical and structural characterization of nanostructures
- Nanostructure fabrication techniques: focused ion beam, nanosphere lithography, atomic layer deposition
- Computer Skills: Proficient in Microsoft Office, WordPerfect, Grapher, CorelDRAW
- Extremely organized, highly adaptable, fast learner, and excellent verbal and communication skills

EDUCATION

Ph.D., Chemistry, Northwestern University
expected June 2007

B.A., Chemistry, Anthropology Minor, University of California, Santa Barbara
December 2001

EXPERIENCE: RESEARCH AND COLLABORATIONS

Northwestern University, Department of Chemistry, Evanston, IL
Graduate Student
2002-present
Thesis: Plasmonic Sensors for Applications in Catalysis and Art Conservation
Advisor: Professor Richard P. Van Duyne

- Devised and acquired novel results for 2 new scientific collaborative research projects at the Art Institute of Chicago and Argonne National Laboratory
- Presented work at 11 national and international conferences, obtained 2 invention disclosures, and wrote and published 10 peer reviewed journal articles including the Journal of the American Chemical Society

Art Institute of Chicago, Department of Conservation, Chicago, IL
Research Coordinator
2004-present

- Initiated a collaboration between Northwestern University and the Art Institute of Chicago
- Designed and implemented new, noninvasive, techniques to characterize artists' materials for the purpose of conserving, preserving, and authenticating works of art
- Utilized SERS to characterize historical red pigments and dyes, which had previously been difficult and often impossible to achieve with normal Raman spectroscopy

Argonne National Laboratory, Argonne, IL
Visiting Researcher
2004-present

- Incorporated new techniques from Argonne to advance current research at Northwestern University resulting in a $150,000 research grant
- Developed a SERS technique to conduct *in-situ* monitoring of important industrial catalytic processes in order to improve product yield and reduce chemical waste

University of Melbourne, Department of Chemistry, Melbourne, Australia
Visiting Researcher
2002

- Worked in Australia as a result of independently acquiring a visiting researcher position with Professor Paul Mulvaney
- Conducted fundamental experiments to study the optical properties of CdSe quantum dots

LEADERSHIP AND ACTIVITIES

- Phi Lambda Upsilon (graduate chemistry honors society)

President
2005-2006

- Led biweekly board meetings composed of 8 executive board members resulting in the creation of a new scientific outreach program to elementary schools, increased profits from laboratory supplies to undergraduates, and raised the monetary value of our travel grants
- Organized several events including the 3rd Annual Career Forum for Northwestern chemistry graduate students attracting the highest attendance to date

Executive Board Member
2004-2006

- South Region High School Science/Math Fair Science Fair Judge
  2004-2006
- Co-organizer of 2nd annual "Nanoscience Day" for local Boy Scouts
  2004
- Teaching Assistant for General Chemistry and Advanced Physical Chemistry Laboratories
  2002-2004
  - Created weekly lesson plans and presented weekly lectures to prepare students for the laboratories

AWARDS AND HONORS

- **L'Oreal Art & Science of Color Silver Prize** for work linking art and science **2006**
- **Andrew W. Mellon Foundation Grant** for research conducted with the Art Institute of Chicago **2006**
- **Young Investigator Prize** for research presented at the Third International Conference on the Application of Raman Spectroscopy in Art and Archaeology, Paris, France **2006**
- **Received 5 independent travel grants 2005**
- **Research in Science and Engineering (RISE) Fellowship** from University of California, Santa Barbara **2001**

SELECTED PUBLICATIONS

1. "Ultrastable Substrates for Surface-Enhanced Raman Spectroscopy: Al_2O_3 Overlayers Fabricated by Atomic Layer Deposition Yield Improved Anthrax Biomarker Detection," X. Zhang, J. Sung, **A. V. Whitney**, J. W. Elam, *J. Am. Chem. Soc.* 128, 10304-10309 (2006).
2. "An innovative surface-enhanced Raman spectroscopy (SERS) method for the identification of six traditional red lakes and dyestuffs," **A. V. Whitney**, F. Casadio, and R. P. Van Duyne, *J. Raman Spectrosc.,* 37, 993-1002 (2006).
3. "Advances in Contemporary Nanosphere Lithographic Techniques," X. Zhang, **A. V. Whitney**, J. Zhao, E. M. Hicks, and R. P. Van Duyne, *Journal of Nanoscience and Nanotechnology*, 6, 1920-1934, (2006).
4. "Surface-enhanced Raman spectroscopy: New materials, concepts, characterization tools, and applications," J. A. Dieringer, O. Lyandres, A. D. McFarland, N. C. Shah, D. A. Stuart, **A. V. Whitney**, C. R. Yonzon, M. A. Young, J. Yuen, X. Zhang, and R. P. Van Duyne, Faraday Discussion 132, 9-26 (2006).
5. "Silver Island Films as Substrates for Surface-Enhanced Raman Spectroscopy (SERS): A Methodological Study on their Application to Artists' Red Dyestuffs", **A. V. Whitney**, F. Casadio, and R. P. Van Duyne, *Proceedings of SPIE-The International Society for Optical Engineering*, 5993, 117-126, (2005).
6. "The Localized Surface Plasmon Resonance Nanosensor: A High Resolution Distance Dependence Study Using Atomic Layer Deposition", **A. V. Whitney**, J. W. Elam, S. Zou, A. V. Zinovev, P. C. Stair, G. C. Schatz, R. P. Van Duyne, *J. Phys. Chem. B.,* 109, 20522-20528 (2005).

7. "Sub-100 nm Triangular Nanopores Fabricated with the Reactive Ion Etching Variant of Nanosphere Lithography and Angle-Resolved Nanosphere Lithography", **A. V. Whitney**, B. D. Myers, and R. P. Van Duyne, *Nano Lett.*, 4, 1507-1511 (2004).

SELECTED PRESENTATIONS

1. "Operando Surface-Enhanced Raman Spectroscopy," Oral Presentation, American Chemical Society 232nd National Meeting, San Francisco, CA, September 2006
2. "Silver Island Films as Substrate for Surface-Enhanced Raman Spectroscopy (SERS): A Methodological Study on Their Application to Artists' Red Dyestuffs," Oral Presentation, International Society for Optical Engineering, Optics East, Boston, MA, October 2005
3. "An Innovative Surface-Enhanced Raman Spectroscopy Method for the Identification of Red Lakes and Dyestuffs," Oral Presentation, 3rd International Conference on the Application of Raman Spectroscopy in Art and Archaeology, Paris, France (**Young Investigator Prize**), September 2005
4. "Monitoring Atomic layer Deposition with the Localized Surface Plasmon Resonance Nanosensor," Oral Presentation, NU Center for Catalysis and Surface Science Seminar Series, May 2005
5. "Monitoring the Thickness of Al_2O_3 Thin Films fabricated by Atomic Layer Deposition" NU Semi-Annual Scientific Meeting of the Institute for Environmental Catalysis Poster Session, March 2005
6. "Sub-100 nm Nanowells Fabricated with the Reactive Ion Etching Variant of Nanosphere Lithography and Angle-Resolved nanosphere Lithography," Pittsburg Conference Poster Session, Chicago, IL, March 2004
7. "Nanoporous Membranes fabricated by Nanosphere Lithography and Reactive Ion Etching," NU Center for Catalysis and Surface Science Annual Scientific Meeting Poster Session, March 2004